GEORG-AUGUST-UNIVERSITÄT
GÖTTINGEN

Fakultät für
Physik

Master's Thesis

Suche nach dem Higgs-Boson im Vektorbosonfusionskanal in $\tau^+\tau^-$-Endzuständen mit dem ATLAS Experiment

Search for the Higgs boson in vector-boson fusion in $\tau^+\tau^-$ final states with the ATLAS experiment

prepared by

Eric Drechsler

from Greiz

at the II. Physikalischen Institut

Thesis number:	II.Physik-UniGö-MSc-2013/04
Thesis period:	1st October 2012 until 31st March 2013
First referee:	Prof. Dr. Arnulf Quadt
Second referee:	Priv. Doz. Dr. Kevin Kröninger

Synopsis

In this thesis, an optimisation study of cut-based Standard Model Higgs boson searches in $\tau^+\tau^-$ final states produced in vector boson fusion (VBF) is presented. The VBF production mode gives rise to a distinctive event topology, which is used to suppress background events. For VBF processes, a marginal jet activity in the central region of the detector is expected. Thus, the application of a central jet veto (CJV) improves the signal-to-background ratio. Different definitions of the CJV are compared in terms of significance for signal selection in this thesis. The study was conducted with data corresponding to an integrated luminosity of 13 fb^{-1} collected by the ATLAS detector in proton-proton collisions at a centre-of-mass energy of $\sqrt{s} = 8$ TeV in 2012.

Die vorliegende Arbeit beschreibt eine Optimierungsstudie zur schnittbasierten Suche nach dem durch Vektorbosonfusion (VBF) produzierten Standard Modell Higgsboson in $\tau^+\tau^-$ Endzuständen. Durch die charakteristische Topologie eines VBF-Ereignisses können Untergrundereignisse unterdrückt werden. Da für ein VBF Ereignis nur marginale Jet-Aktivität im Zentralbereich des Detektors erwartet wird, kann ein zentrales Jet Veto genutzt werden, um zwischen Signal und Untergrundereignissen zu unterscheiden. In dieser Arbeit wurden verschiedene Definitionen eines solchen zentralen Jet Vetos untersucht, um die Signifikanz der Signalselektion zu optimieren. Die Studie wurde mit den in 2012 mit dem ATLAS Detektor gesammelten Daten in Proton-Proton Kollisionen durchgeführt. Der ausgewertete Datensatz entspricht einer integrierten Luminosität von 13 fb^{-1} bei einer Schwerpunktsenergie von $\sqrt{s} = 8$ TeV.

Contents

1. Introduction

Since the dawn of time, mankind is seeking for the answers to the great questions of existence. Where do we come from? What are we made of? Why does our world and the universe evolve as we observe it?

Modern particle physics approaches these topics, by investigating the physics of the fundamental constituents of matter. Formulated in the 1970s, the *Standard Model of particle physics* (SM) contains our current knowledge about the elementary particles which matter is made of. These particles are grouped into *quarks* and *leptons*, which interact via three fundamental forces, mediated by *gauge bosons*. The masses of these fundamental particles is explained by the *Higgs mechanism*, which gives rise to another, substantial particle - the *Higgs boson* H.
Within the last decades, many of the predictions of the SM have been tested with high precision. Several experimental facilities, like LEP, TEVATRON and HERA, succeeded in confirming and measuring properties of the elementary particles. Despite the success of the SM, several shortcomings arise from unanswered questions, like the origin of dark matter and the asymmetry between matter and antimatter in the universe. In order to approach these questions, new particle accelerators are built to increase the explored energy regime.

The *Large Hadron Collider* (LHC) at CERN is currently the world's most powerful particle accelerator, colliding bunches of protons at a design centre-of-mass energy of $\sqrt{s} = 14$ TeV. The main experiments ATLAS, CMS, ALICE and LHCb are located at four separated interaction points.

In Summer 2012, the ATLAS and the CMS collaborations announced the discovery of a new boson in the context of searches for the SM Higgs boson. This is a tremendous success for the LHC's research programme and marks the beginning of a new era in modern particle physics. In order to study the nature of this new boson and eventually confirm that it is exactly the predicted SM Higgs boson, precise measurements of its properties need to be performed. An important step towards this confirmation is a proof of the boson's coupling to fermions, which should be

proportional to their masses. For that reasons, dedicated searches in $\tau^+\tau^-$ final states are performed, aiming at a discovery of the $H \to \tau^+\tau^-$ process.

In this thesis, an optimisation study of cut-based SM Higgs boson searches in $\tau^+\tau^-$ final states produced in vector boson fusion (VBF) is presented. The VBF production mode gives rise to a distinctive event topology, which is used to suppress background events. The study was conducted with 13 fb^{-1} data collected by the ATLAS detector at $\sqrt{s} = 8$ TeV proton-proton collisions in 2012.

After this introduction, a summary of the Standard Model is given in Chapter (2). In particular, Higgs physics and phenomenology, as well as the recent discovery are discussed. Furthermore, characteristics of physics at hadron colliders are presented. In Chapter (3), an overview of the experimental setup, namely the LHC and the ATLAS detector is given. Afterwards, in Chapter (4), the object definitions are presented. The datasets and the physics process modelling methods used for the study are discussed in Chapter (5). Thereafter, the analysis strategy, the control study and the final optimisation study is presented in Chapter (6). The thesis is concluded by a summary and outlook in Chapter (7).

2. The Standard Model and Higgs Physics

In this chapter, an introduction to the Standard Model of Particle Physics is given, presenting some of its remarkable successes as well as stating shortcomings and contradictions. As a crucial ingredient, the Higgs mechanism is briefly discussed and theoretical as well as experimental implications are presented. Finally, an overview of recent experimental results concerning the discovery of a Higgs-like boson is given.

2.1. The Standard Model of Particle Physics

The Standard Model of Particle Physics (SM) is currently the most successful and comprehensive theoretical model for the description of elementary particles and their interactions. The SM in its current formulation was developed in the 1970s. Since then experimental measurements confirmed the predictions of the SM, the most recent being the discovery of a Higgs-like boson [1–3].

The SM is a renormalisable and locally Lorentz-gauge invariant quantum field theory. Internal symmetries of the unitary gauge group

$$\mathrm{SU}(3)_C \times \mathrm{SU}(2)_L \times \mathrm{U}(1)_Y \tag{2.1}$$

give rise to the fundamental interactions and properties of the SM particle fields. C stands for colour, L for left-handedness and Y for the weak hypercharge, altogether depicting characteristics of the symmetry transformations related to each group.
The SM can be formulated using the Lagrange formalism [1, 4]. By requiring local gauge invariance under transformations described by the group in Equ. 2.1, the force-mediating fields are introduced. Following *Noether's Theorem*, the internal symmetries yield conserved quantities for the system [5]. The SM in its current form describes the electromagnetic, the weak and the strong interaction. Gravity

is not included in the theory, but can be neglected at energy scales accessible with current collider experiments. Hence the SM is understood as an *effective* quantum field theory, since it is expected to fail to describe physics at energies where gravity effects become significant [6].

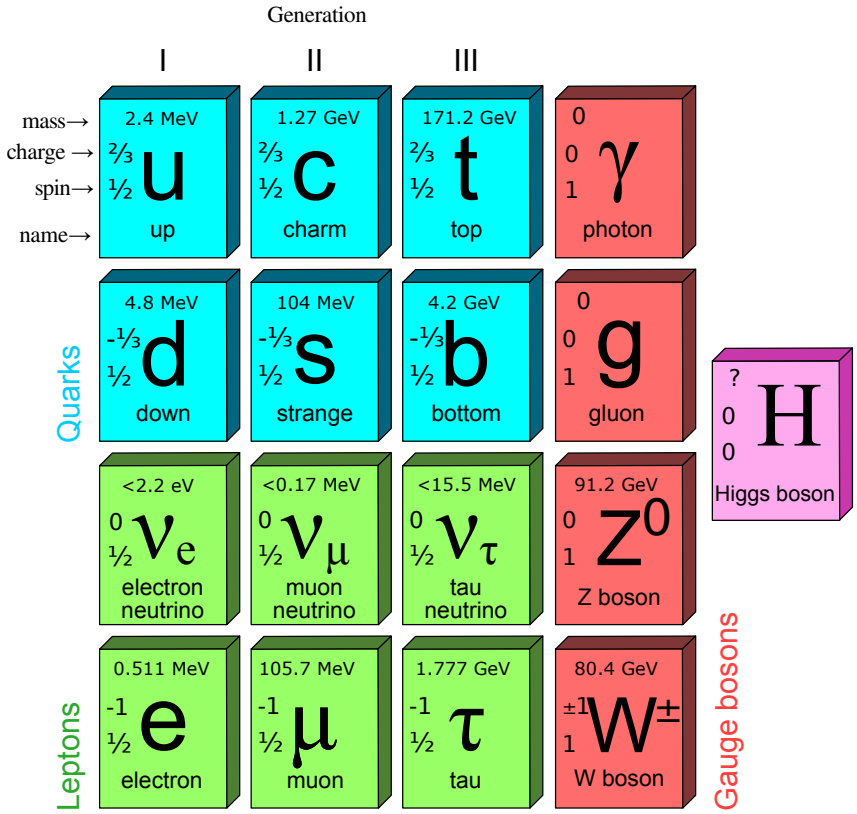

Figure 2.1.: A representation of the particles described by the SM [7]. All particles have been experimentally verified and their properties measured to high precision [8]. The nature of the recently discovered Higgs-like boson is not yet completely verified.

A representation of the particles incorporated in the SM together with some of their properties is shown in Fig. 2.1. A set of quantum numbers for each particle determines their characteristics and behaviour.
The leptons and quarks are grouped together as fermions and arranged in three generations with increasing masses from left to right. Each fermion carries spin-1/2. With an integer spin of 1, vector-bosons are the force mediators in the SM and behave fundamentally different from fermions. The electromagnetic force is mediated by the massless photon γ, the weak force by the massive Z^0, $W^{\pm}$ bosons

and the strong force by eight massless gluons g. The only scalar boson with spin-0 incorporated in the SM is the Higgs boson H.

The electrically charged leptons $\ell = e,\ \mu,\ \tau$ form, together with their corresponding neutral neutrinos $\nu_\ell = \nu_e,\ \nu_\mu,\ \nu_\tau$ left-handed doublets $(\nu_\ell,\ \ell)$ with weak isospin components $I_3 = \pm 1/2$. In the quark sector such a doublet consists of an up-type quark $q_u = u,\ c,\ t$ with electric charge $2/3e$ and a down-type-quark $q_d = d,\ s,\ b$ with charge $-1/3e$. Furthermore right-handed particles form singlets with a weak-isospin component $I_3 = 0$. For each fermion there also exists an antiparticle with the same properties but opposite additive quantum numbers, like electrical and colour charge.

2.1.1. Quantum Chromodynamics

The theoretical formulation of the strong force is called Quantum Chromodynamics (QCD) and described by the non-Abelian local gauge symmetry group $\mathrm{SU}(3)_C$. The generators of this group can be represented by the eight Gell-Mann matrices λ_i. The quantum numbers of $\mathrm{SU}(3)_C$ are three colours, referred to as red, green and blue. Only quarks and gluons participate in the strong interaction, the latter being the mediators of the interactions. The gluons carry a colour charge and an anti-colour charge, while the (anti-)quarks only carry one (anti-)colour charge. Gluons are therefore able to interact among each other, causing the non-Abelian nature of QCD.
The QCD-Lagrangian can be written as

$$\mathcal{L}_{\mathrm{QCD}} = \sum_q \psi_q^\dagger \left(i\gamma^\mu (\partial_\mu + 2\pi i\, \alpha_s \lambda_c \mathcal{A}_\mu^c) - m_q \right) \psi_q - \frac{1}{4} G_{\mu\nu}^a G_a^{\mu\nu} \tag{2.2}$$

where $G_{\mu\nu}^a$ denote the field strength tensors, $\lambda_c \mathcal{A}_\mu^c$ the gluon fields contracted with the Gell-Mann matrices and α_s the strong coupling constant.

The running coupling constant α_s describes the strength of the energy-dependent coupling between quarks and gluons. The coupling constant can be expressed as a function of an arbitrary energy scale, which in the context of the SM is commonly $\Lambda_{\mathrm{QCD}} \approx 200\mathrm{MeV}$. An evaluation of the coupling constant at an energy Q is possible by

$$\alpha_s(Q^2; Q > \Lambda_{\mathrm{QCD}}) = \frac{12\pi}{(33 - 2n_f) \ln\left(\frac{Q^2}{\Lambda_{\mathrm{QCD}}}\right)} \tag{2.3}$$

where n_f denotes the number of quark flavours available at the energy scale Q with $n_f = 6$ for $Q > m_{\text{top}}$.

Inspecting Equ. 2.3 it can be seen that for large energies, or short distances, the strength of the coupling decreases. This behaviour incorporates two characteristic effects of the strong interaction:

- for short distances quarks act like free particles since the strong coupling constant is small. This effect is called *asymptotic freedom*.
- for large distances, or low energy, quarks experience a confining potential. When separating two quarks it becomes energetically more favourable at some point to create a new quark-antiquark pair than separating the quarks further. The created quarks then form bound states with the original ones. This is called *confinement* and explains why quarks appear only in bound, i.e. hadronic (qqq) or mesonic ($q\bar{q}$) states. Perturbative description of this long-distance part of the strong force is not possible since the coupling constant becomes too large for the perturbative expansion to work.

2.1.2. Theory of Electroweak Interaction

The electroweak theory represents the unification of the electromagnetic and the weak interaction [9–12]. It is described by the combination of symmetry groups $\mathrm{SU}(2)_L \times \mathrm{U}(1)_Y$.

The non-Abelian unitary group $\mathrm{SU}(2)_L$ is generated by the three Pauli matrices σ_i and implies the conservation of the third weak isospin component I_3. Its three gauge fields are W^i_μ with $i = 1, 2, 3$. Right-handed fermions with the trivial isospin $I_3 = 0$ are invariant under $\mathrm{SU}(2)_L$ transformations and form singlets which therefore do not interact weakly. This causes the parity-violation of the weak interaction [13]. Left-handed fermions transform under $\mathrm{SU}(2)_L$ and appear as doublets with $I_3 = \pm 1/2$. The generator of the Abelian symmetry group $\mathrm{U}(1)_Y$ is the weak hypercharge Y The corresponding gauge field is B^μ.

The electroweak part of the SM Lagrangian can be written as

$$\begin{aligned}\mathcal{L}_{\mathrm{EW}} = &\psi_L^\dagger \gamma^\mu \left(i\,\partial_\mu - \tfrac{g}{2}\sigma_j W_\mu^j - \tfrac{g'}{2} Y B_\mu \right) \psi_L \\ &+ \psi_R^\dagger \gamma^\mu \left(i\,\partial_\mu - \tfrac{g'}{2} Y B_\mu \right) \psi_R \\ &- \frac{1}{4}\left(W_{\mu\nu}^j W_j^{\mu\nu} + B_{\mu\nu} B^{\mu\nu} \right)\end{aligned} \tag{2.4}$$

where g and g' are coupling constants. The three terms describe the interaction of left-handed particles, the interaction of right-handed particles, and the self interaction or field strength of the gauge fields.

The physical mass eigenstates of the electroweak interaction are the gauge bosons

$$\begin{aligned} A_\mu &= W_\mu^3 \sin\theta_W + B_\mu \cos\theta_W && \text{(photon } \gamma\text{)} \\ Z_\mu &= W_\mu^3 \sin\theta_W - B_\mu \cos\theta_W && (Z\text{−Boson } Z^0) \\ W_\mu^\pm &= \tfrac{1}{\sqrt{2}}\left(W_\mu^1 \mp i\, W_\mu^2 \right) && (W\text{−Bosons } W^\pm) \end{aligned} \tag{2.5}$$

with θ_W denoting the weak mixing angle, called *Weinberg-angle*. This angle relates to the electroweak coupling constants via

$$\sin\theta_W = \frac{g'}{\sqrt{g^2 + g'^2}} \qquad . \tag{2.6}$$

This value is not predicted by the SM and has to be determined experimentally. It is measured to be $\sin^2\theta_W = 0.21316 \pm 0.00016$ [8]. The gauge bosons in Equ. 2.5 are massless. However, the Z^0 and the $W^\pm$ bosons discovered in the 1980's at the UA1 and UA2 experiments at CERN are massive with $m_W = (80.399 \pm 0.023)$ GeV and $m_Z = (91.1876 \pm 0.0021)$ GeV [8, 14–16]. In the SM, these masses can be accounted for by the Higgs mechanism which is presented in Sec. (2.1.3).

Another important aspect of electroweak theory is the weak interaction in the quark sector. Mass and weak eigenstates of quarks q and q' are not identical, but related by the unitary Cabibbo-Kobayashi-Maskawa (CKM) matrix

$$\begin{pmatrix} d' \\ s' \\ b' \end{pmatrix} = \begin{pmatrix} V_{ud} & V_{us} & V_{ub} \\ V_{cd} & V_{cs} & V_{cb} \\ V_{td} & V_{ts} & V_{tb} \end{pmatrix} \begin{pmatrix} d \\ s \\ b \end{pmatrix} \tag{2.7}$$

with non-vanishing off-diagonal elements [8, 13, 17]. The latter imply flavour-

changing charged currents mediated by $W^{\pm}$ bosons. So far, no flavour-changing neutral currents (FCNC) have been observed [18]. The off-diagonal terms of the CKM matrix are complex numbers. This gives an explanation for $\mathcal{CP}$-violation in the SM [13].

2.1.3. The Higgs Mechanism

A mass term for a gauge boson X in the SM Lagrangian would naively require a term like $m^2 X_\mu X^\mu$ which would spoil local gauge symmetry. The Higgs mechanism, developed in the 1960s, offers an elegant solution incorporating *spontaneous symmetry breaking*. It introduces masses for gauge bosons without violating the gauge symmetry [6, 19].
The Higgs mechanism introduces a complex scalar field doublet Φ, together with its potential $V(|\Phi|)$

$$\Phi = \begin{pmatrix} \Phi^+ \\ \Phi^0 \end{pmatrix} \tag{2.8}$$

$$V(|\Phi|) = \mu^2 \left(\Phi^\dagger \Phi\right) + \lambda \left(\Phi^\dagger \Phi\right)^2 \quad . \tag{2.9}$$

Thus, a new term is added to the SM Lagrangian

$$\begin{aligned} \mathcal{L}_{\text{Higgs}} = &\left(\partial_\mu \Phi + i\tfrac{g}{2}\sigma_j W_\mu^j \Phi + i\tfrac{g'}{2} Y B_\mu \Phi\right)^\dagger \left(\partial^\mu \Phi + i\tfrac{g}{2}\sigma^j W_j^\mu \Phi + i\tfrac{g'}{2} Y B^\mu \Phi\right) \\ &- V(|\Phi|) \quad . \end{aligned} \tag{2.10}$$

The potential in Equ. 2.9 has two parameters μ^2 and λ. The latter has to be positive definit to ensure a lower boundary for the potential.

A positive μ^2 merely leads to a spin-0 particle with mass μ [20]. For a negative $\mu^2 < 0$ the potential is sketched in Fig. 2.2 with a non-zero global minimum for the neutral component of Φ at

$$\langle \Phi \rangle_0 = \begin{pmatrix} 0 \\ \frac{1}{\sqrt{2}} v \end{pmatrix} \qquad \text{with} \qquad v = \sqrt{-\frac{\mu^2}{\lambda}} \quad .$$

The non-vanishing vacuum expectation value (VEV) v introduces the spontaneous symmetry breaking: the ground state at 0 is only meta-stable, a system may now spontaneously exit this state towards the global minimum at v. This global minimum

for Equ. 2.9 is degenerate and experimentally measured from muon decays and its relation to the Fermi-coupling constant to be $v \approx 246$ GeV [1, 8].

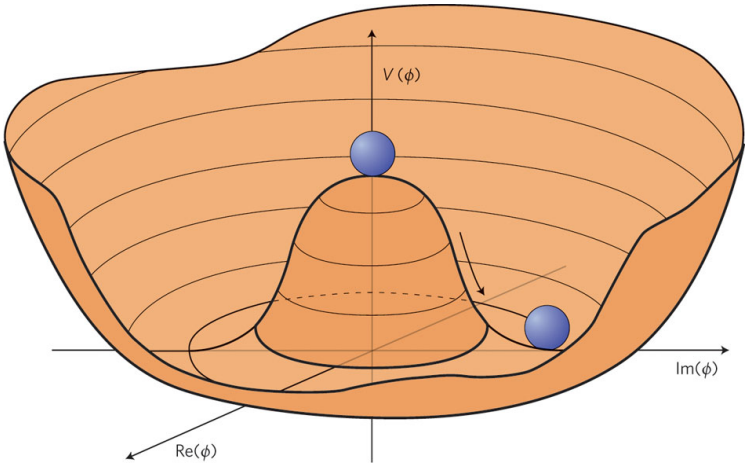

Figure 2.2.: Potential $V(\Phi)$ of the Higgs field. The movement of the ball represents spontaneous symmetry breaking of the system [21].

Using first order perturbation theory and the *unitary gauge*, the scalar field in Equ. 2.8 can be written as

$$\Phi = \frac{1}{\sqrt{2}} \begin{pmatrix} 0 \\ v + H(x) \end{pmatrix} \tag{2.11}$$

where $H(x)$ denotes the physical Higgs field or Higgs boson. By plugging Equ. 2.11 into the Lagrangian in Equ. 2.10 and rewriting the expression in terms of the physical gauge bosons in Equ. 2.5 it follows

$$\begin{aligned} \mathcal{L}_{\text{Higgs}} = & \underbrace{\frac{1}{4} g^2 v^2 W_\mu^+ W^{-,\mu} + \frac{1}{8}(g^2 + g'^2) v^2 Z_\mu Z^\mu \, (+0 \cdot A_\mu A^\mu)}_{\text{gauge boson mass terms}} \\ & \underbrace{+\mathcal{L}^H_{\text{kin}} + \mathcal{L}^H_{\text{mass}} + \mathcal{L}^H_{\text{Couplings}}}_{\text{Higgs physics terms}} \quad . \end{aligned} \tag{2.12}$$

The last three terms in Equ. 2.12, describing the kinetic energy, mass and couplings of the Higgs boson, are explained in Sec. (2.2.1). The gauge boson mass terms yield

the relations

$$\begin{aligned} m_A &= 0 = m_\gamma \\ m_Z &= \frac{1}{2} v \sqrt{g^2 + g'^2} \\ m_W &= \frac{1}{2} v g = m_Z \cos\theta_W \end{aligned}$$

and hence the photon is massless, while the bosons Z^0 and $W^\pm$ are massive. The masses of the latter are dependent on the VEV and the weak coupling constants g, g'. The Higgs mechanism therefore introduces particle masses without spoiling the symmetry but introducing a new field with a non-trivial ground state.

With the Higgs mechanism, fermion masses can also be implemented in the SM. For this a *Yukawa coupling* between fermions and the Higgs field is introduced by adding

$$\mathcal{L}_{\text{Yuk}} = -\, i \sum_f \lambda_f \psi_f^\dagger \Phi \psi_f \tag{2.13}$$

to the SM Lagrangian. The parameter λ_f describes the coupling strengths of the fermions f to the Higgs field, resulting in fermion mass terms

$$m_f = \frac{\lambda_f v}{\sqrt{2}} \qquad . \tag{2.14}$$

2.1.4. Open Questions

The SM is a very successful theoretical framework and explains many experimental observations at hadron colliders at high precision. Though, there are several shortcomings and open questions which indicate the need for modifications or extensions of the SM.

There are experimental results which differ from SM predictions. For example, recent experimental results indicate, that only ~ 5 % of the energy content observed in the universe is described by the particles of the SM, the remaining 95 % is composed of 27 % *dark matter* and 68 % *dark energy* [22]. The SM does not provide an explanation for the nature of these constituents. Supersymmetric extensions of the SM, like the MSSM, can provide a dark matter candidate. Another example is the measurement of the anomalous magnetic moment of muons which reveales a

discrepancy to the SM expectation by 3.4 standard deviations [8].

Furthermore, there are some fundamental open questions which cannot be answered within the SM. There is no explanation why quarks carry a third of the electrons's charge or why there are exactly three generations of fermions following a mass hierarchy. The complicated group structure in Equ. 2.1 is expected to be unified at very high energies which does not happen within the SM [23]. It is also unclear how the asymmetry between the amount of matter and antimatter arose in the early universe. The $\mathcal{CP}$-violation predicted by the SM is too small to explain this imbalance [24].

Another unsatisfactory problem is the fine-tuning or hierarchy problem. The Higgs boson mass receives corrections from fermionic tree level loop diagrams which are proportional to the fermions masses and a cut-off scale Λ_{UV} at which quantum gravity effects become important in absence of new physics. This scale is expected to be close to the Planck mass $m_P \sim 10^{19}$ GeV, which is several magnitudes larger than the allowed Higgs mass between $100 - 1000$ GeV [23]. To obtain the low value for the Higgs mass the parameter μ^2 can be adjusted to cancel the contribution from the mass correction. This adjustment would require the very precise cancellation of two very large numbers. This fine tuning seems unnatural and unlikely [23].

2.2. Higgs-Physics and Phenomenology

This section deals with the properties and phenomenology of the SM Higgs boson. Furthermore recent results concerning the discovery of a Higgs-like boson are presented. Only if all of its properties are experimentally confirmed, a discovery of the SM Higgs boson can be claimed with certainty.

2.2.1. Properties of the Higgs-Boson

Since the Higgs field in Equ. 2.8 is scalar the Higgs boson is a spin-0 particle. The full part of the Lagrangian in Equ. 2.12 containing the physical Higgs field H is

$$\mathcal{L}_{\text{Higgs}} = \underbrace{\tfrac{1}{2}\partial_\mu H \partial^\mu H}_{\text{kinetic term}} - \underbrace{\lambda v^2 H^2}_{\text{mass term}} - \underbrace{(\,\lambda v H^3 + \tfrac{1}{4} H^4\,)}_{\text{self coupling}} \tag{2.15}$$

$$+ \underbrace{\tfrac{1}{2}\, g^2 v H\, W_\mu^+ W^{-,\mu} + \tfrac{1}{4}\,(g^2 + g'^2) v H\, Z_\mu Z^{-,\mu}}_{\text{triple gauge boson couplings}} \tag{2.16}$$

$$+ \underbrace{\tfrac{1}{4}\, g^2 H^2 W_\mu^+ W^{-,\mu} + \tfrac{1}{8}\,(g^2 + g'^2) H^2 Z_\mu Z^\mu}_{\text{quartic gauge boson couplings}} \quad , \tag{2.17}$$

encoding its properties and couplings. The mass of the Higgs boson is

$$m_H = \sqrt{2\lambda}\, v = \sqrt{-2\mu^2} \tag{2.18}$$

with the unknown parameters λ and μ.

From theoretical constraints, boundaries for the Higgs mass can be set, dependent on the cut-off scale Λ_{UV}. Upper constraints can be derived by requiring unitarity for tree-level contributions of scattering processes involving gauge bosons and the Higgs boson. Furthermore, a breakdown of perturbation theory as well as occuring coupling divergences - called *triviality bound* - constrain the upper value of the Higgs mass.
Lower limits are achieved by the *stability bound*. In order to have a stable vacuum, the potential in Equ. 2.9 must be bounded from below and hence $\lambda > 0$. This imposes a constraint on the Higgs mass from below.

Taking these arguments into account, limits for the Higgs mass are given as

$$50 \text{ GeV} \lesssim m_H \lesssim 800 \text{ GeV} \qquad \text{for } \Lambda_{\text{UV}} \sim 10^4 \text{ GeV or} \tag{2.19}$$

$$130 \text{ GeV} \lesssim m_H \lesssim 180 \text{ GeV} \qquad \text{for } \Lambda_{\text{UV}} \sim 10^{16} \text{ GeV} , \tag{2.20}$$

depending on the cut-off scale up to which the SM is expect to be valid [20].

The coupling terms in Equ. 2.17 are the Higgs bosons self interaction and the coupling to the gauge bosons. They are sketched together with the Yukawa coupling to fermions from Equ. 2.13 and their coupling strengths in Fig. 2.3.

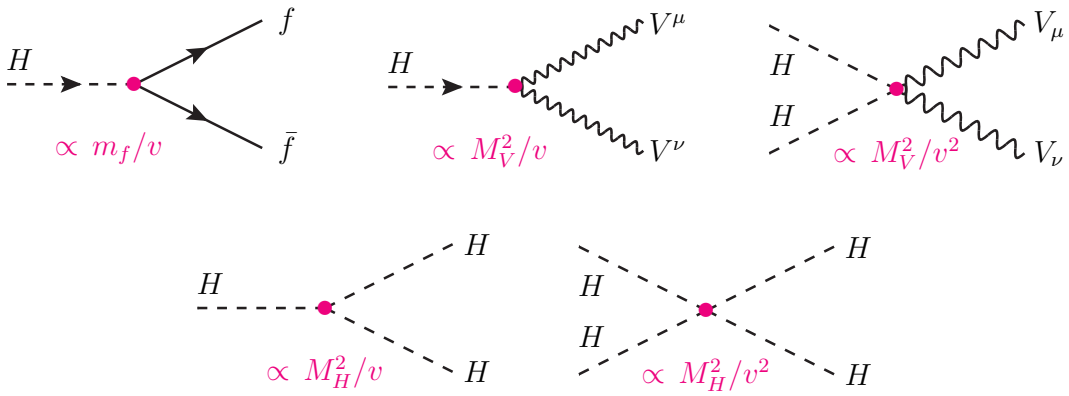

Figure 2.3.: Feynman diagram of the SM Higgs couplings.

2.2.2. Higgs Production at the LHC

In hadron colliders, Higgs bosons are produced by interactions involving gluons and quarks. The dominant processes at the LHC are depicted in Fig. 2.4.
All numerical cross section values quoted in the following were calculated for a centre-of-mass energy of $\sqrt{s} = 8$ TeV and a Higgs mass of $m_H \simeq 125$ GeV [20, 25].

The *gluon-gluon fusion* in Fig. 2.4a is the dominant production mode at LHC with a cross section of $\sigma(pp \to H) \simeq 40.25$ pb. The process is mediated by triangular loops of heavy quarks, primarily the top-quark in the SM. Higher-order corrections play an important role for this process, reflected in factorisation and renormalisation scale dependence.

The *vector-boson fusion* sketched in Fig. 2.4b is the subdominant production mode with $\sigma(pp \to Hqq) \simeq 4.72$ pb and has a unique signature. The scattered quarks

create two separated jets with large transverse momenta in the forward and backward detector region, which can be used for efficient background suppression. Only small additional jet activity is expected in the central region of the detector for this process.

In *Higgs-strahlung* processes, as shown in Fig. 2.4c, a weak gauge boson radiates a Higgs boson. This production channel has a cross section of $\sigma(p \to VH) \simeq 2.54$ pb. At the LHC this production mode is important for low-mass Higgs searches. The decay products of the associated weak gauge boson can be used to distinguish between signal and background events.

The fourth most dominant production channel at the LHC is the *associated production* of a Higgs boson with pairs of heavy quarks, mainly top-quarks, depicted in Fig. 2.4d. This channel allows for a measurement of the Yukawa coupling to the top-quark. The production cross section is $\sigma(pp \to t\bar{t}H) \simeq 0.70$ pb.

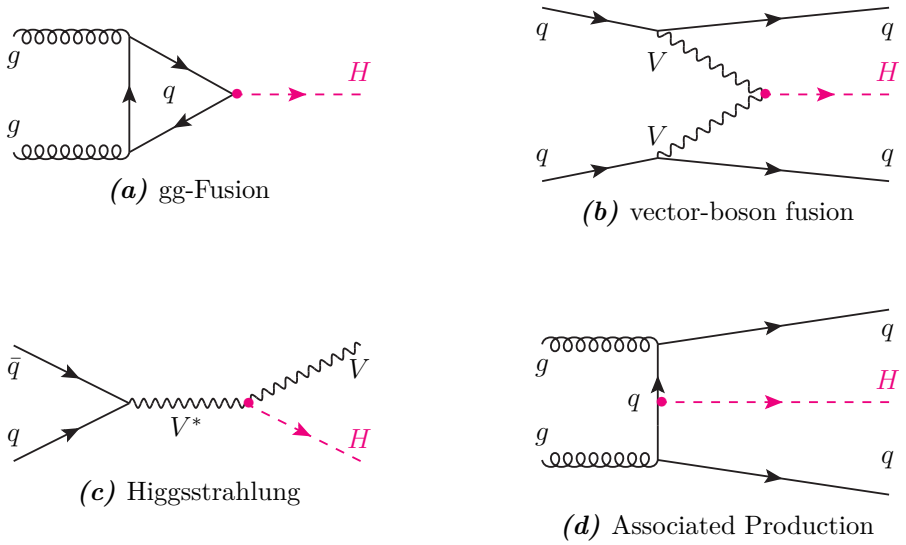

(a) gg-Fusion

(b) vector-boson fusion

(c) Higgsstrahlung

(d) Associated Production

Figure 2.4.: Feynman Diagrams of the dominant Higgs production channels at pp-colliders like the LHC.

A comparison of the different Higgs cross sections in dependence of the Higgs mass at the LHC is shown in Fig. 2.5 for $\sqrt{s} = 8$ TeV. Each of the dominant channels is drawn separately. For increasing masses, the cross-sections decrease.

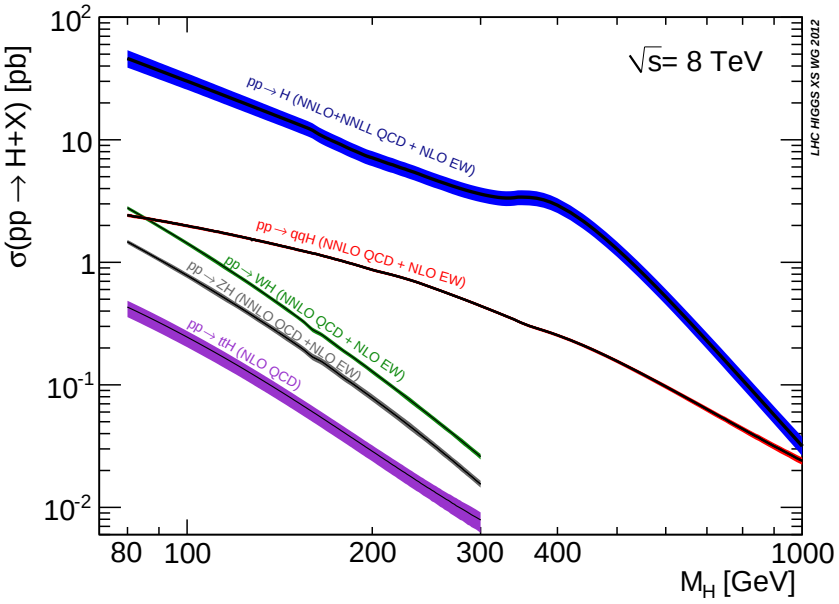

Figure 2.5.: Production cross sections for the Higgs boson in pp collisions at $\sqrt{s} =$ 8 TeV [25].

2.2.3. Higgs-Searches and Decay Channels

The Higgs coupling strengths to particles in Fig. 2.3 are proportional to the masses of the fermions and gauge bosons. Therefore, it is most probable that the Higgs boson decays into the heaviest particles allowed by phase space. For a fixed Higgs mass, all partial decay widths can be predicted [20].

Decays into massless particles like photons $H \to \gamma\gamma$ and gluons $H \to gg$ are realised via loops of W bosons, charged fermions or, in the gluon case, only quark loops similiar to Fig. 2.4a. The branching ratio $BR(H)$ in dependence on the Higgs mass are sketched in Fig. 2.6.

For each Higgs mass range different decay modes and hence search strategies have to be considered. In the low mass range interesting decay modes in terms of discovery potential are [26, 27]

- $H \to b\bar{b}$ has the highest branching ratio for low masses but is experimentally difficult to detect due to the large multi-jet background. When produced with leptonic decaying W/Z boson (associated production or Higgs-strahlung), the event topology can be triggered upon. An excellent b-tagging algorithm is required.

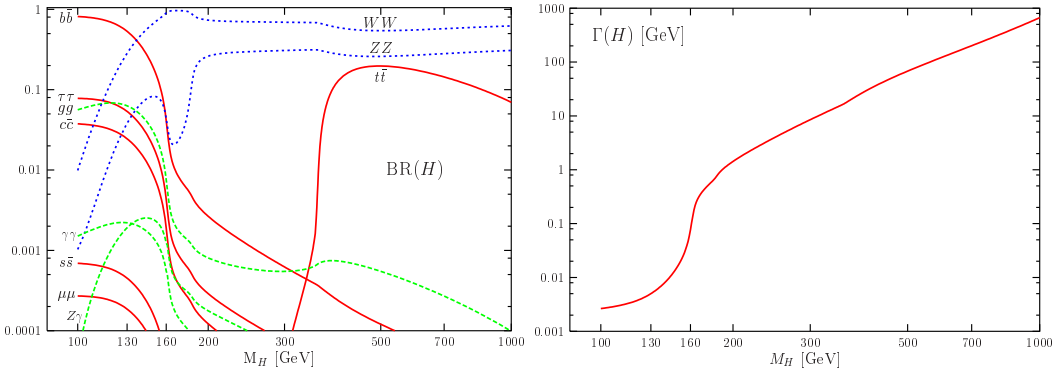

Figure 2.6.: The branching ratios $BR(H)$ for Higgs decays as a function of the Higgs mass (left) and the full mass-dependent Higgs boson decay width $\Gamma(H)$ (right) [20].

- $H \to \tau\tau$ is the only channel where the Yukawa coupling in the lepton sector can be measured at the LHC. In combination with vector boson fusion as production process, background events can be rejected efficiently because of the distinctive event topology.
- $H \to \gamma\gamma$ has a rather low branching ratio of a few per mille but can be detected accurately since a high mass resolution can be provided for the photon pair. This requires a high energy- and angular resolution of the electromagnetic calorimeter as well as an accurate particle identification.

With increasing mass, the decay into two gauge bosons $WW^{(*)}$ and $ZZ^{(*)}$ becomes dominant. Below the kinematic threshold, one of the bosons is off-shell and hence virtual. After passing the threshold, the decay into WW is dominant and the branching ratio approximately 1. Passing the ZZ threshold, the corresponding branching ratio increases to $\sim 1/3$ but the WW channel remains dominant since there are two possible decay configurations. For $m_H > 350$ GeV, the Higgs can also decay into a top-pair.
In this higher mass region two particularly interesting modes are

- $H \to ZZ \to \ell\ell\ell\ell$ with $\ell = e, \mu$ because of its very clean signature of four leptons with high p_t. Due to the highly suppressed background contribution and the possibility to fully reconstruct the final state, allowing for high precision measurements, the mode is called *golden channel*.
- $H \to WW \to \ell\nu_\ell\,\ell\nu_\ell$ which has a high branching ratio. For an estimation of

the Higgs mass the transverse mass m_T is used because of the neutrinos in the final state.

In Fig. 2.6, the mass dependent total decay width of the Higgs boson is shown. For low mass regions its decay width is very narrow. With increasing mass the decay width becomes rapidly wider resulting in a very broad resonant structure [20].

Prior to the LHC, direct Higgs searches were conducted by experiments at the *Large Electron-Positron Collider* LEP at CERN and the TEVATRON Collider at FERMILAB. Indirect constraints for the Higgs mass were achieved by global fits using the dependence of the W boson mass on loop contributions from the Higgs boson and the top quark [28].

A total amount of 2.4 fb^{-1} of data at a centre-of-mass energy between $189 - 209$ GeV was recorded at LEP. The lower bound for the Higgs mass set by LEP is 114.4 GeV at a confidence level (CL) of 95% [29].
The combined results from CDF and DØ at the TEVATRON use up to 10 fb^{-1} of $p\bar{p}$ data at $\sqrt{s} = 1.96$ TeV. An exclusion of the region $147 < m_H < 180$ GeV at 95% CL was achieved. Furthermore, an excess with a global significance of $\sim 2.7\sigma$ was observed between $115 < m_H < 140$ GeV [30, 31].

On July 4th 2012, the ATLAS and CMS collaborations announced the discovery of a new boson.
The CMS collaboration combined 5.1 fb^{-1} at $\sqrt{s} = 7$ TeV and 5.3 fb^{-1} at $\sqrt{s} = 8$ TeV and observed an excess with local significance of 5.0σ at a mass of $m_H = 125.3 \pm 0.4(\text{stat}) \pm 0.4(\text{sys})$ GeV [2].

The ATLAS collaboration's combination of the full 2011 data sample with 4.8 fb^{-1} at $\sqrt{s} = 7$ TeV and the 2012 data sample with 5.8 fb^{-1} at $\sqrt{s} = 8$ TeV yields an excess with local significance of 5.9σ at a mass of $m_H = 126.0 \pm 0.4(\text{stat}) \pm 0.4(\text{sys})$ GeV. The probability of this excess to be caused by a statistical fluctuation of the background is $1.7 \cdot 10^{-9}$ and depicted in Fig. 2.7. For these results, the channels $H \to \gamma\gamma$, $ZZ^{(*)}(\to 4\ell)$, $WW^{(*)}$ as well as $H \to b\bar{b}$, $\tau^+\tau^-$ in 7 TeV data and $H \to \gamma\gamma$, $ZZ^{(*)} \to 4\ell$, $WW^{(*)}(\to e\mu\nu_e\nu_\mu)$ in 8 TeV data were combined [3].
By including 13 fb^{-1} of data at $\sqrt{s} = 8$ TeV available in November 2012, the observed excess reached a significance of 7σ [32].
The new particle decays into two photons or Z-pairs indicating its bosonic nature from spin conservation arguments. The two photon channel suggest furthermore, that the new bosons spin is different from one [6]. In order to verify, that the

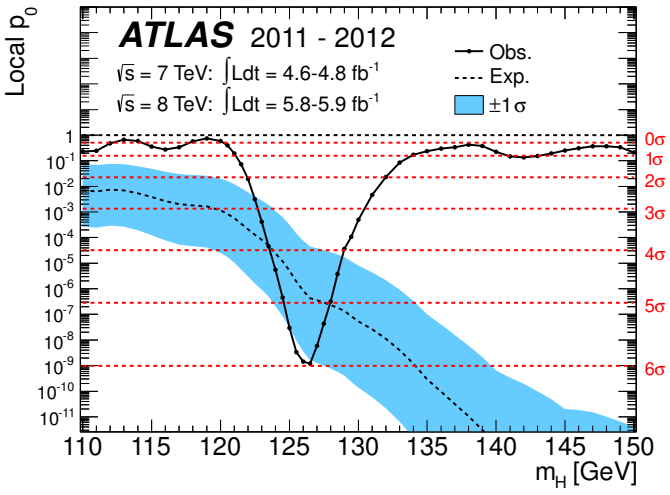

Figure 2.7.: The local background fluctuation probability as a function of the reconstructed mass for the discovery announced on July 4th 2012 [3].

discovered boson is the predicted SM Higgs boson, its properties need to be studied in detail. The boson's coupling to fermions, spin and parity properties, as well as signal strength for all channels need to be studied precisely in order to investigate the boson's nature. Studies of the boson's couplings with 13 fb^{-1} of data in November 2012 are in agreement with the SM predictions [33].
Studies of the Higgs' triple and quartic couplings are difficult at the LHC because of the insufficient sensitivity, but will be possible with future high-luminosity upgrades [27]. Future collider projects, like the *International Linear Collider* (ILC), will be able to provide complementary measurements [34].

2.3. Hadron Collider Physics

The interacting particles at the LHC are the constituents of the proton - gluons and quarks, also called *partons*. A profound knowledge of the structure of the proton is required in order to describe the proton-proton interactions and to calculate total cross sections. In the following, the description of the proton's structure is presented together with phenomenological QCD models which are crucial for describing data at ATLAS [26].

2.3.1. Parton Density Functions

The structure of the proton depends on its energy. For low energies, a proton can be described by the three valence-quarks $p = (uud)$, while at high energies additional sea-quark and gluon contributions have to be taken into account. Determining a proton's structure is hence dependent on the energy scale at which the proton is probed, called *factorisation scale* μ_F^2.

Each parton i of a proton carries a fraction x_i of the protons total momentum, called the *Bjorken-x* [35]. The probability density of finding parton i with a momentum fraction x_i at an energy μ_F^2 is modelled by the *parton density functions* (PDF) $f_i(x_i, \mu_F^2)$. A perturbative calculation of the PDFs from first principles is not possible, since they receive contributions from the long-distance part of the strong interaction, as described in Sec. (2.1.1). Instead, experimental data is used. In *deep inelastic scattering* (DIS) experiments, like the *ep* collider HERA at DESY, the PDFs were measured at certain energy scales [36, 37]. By using the DGLAP[1] QCD evolution equations, the PDFs are extrapolated to higher energy scales, as present at the LHC [38]. Different strategies for the description of the PDFs can be used, e.g. the approaches by the CTEQ or MRST groups [39–43]. These PDFs introduce theoretical and experimental uncertainties for calculations of total and differential cross sections. In this thesis the CTEQ-PDF sets are used.

2.3.2. Cross Sections

For the calculation of QCD cross sections strong interactions are categorised into two types according to their energy regimes: the *hard* scattering processes at short

[1] Dokshitzer-Gribov-Lipatov-Altarelli-Parisi equations

distances and the *soft* interactions for long distances. Perturbative QCD calculations can be used to describe the hard interactions, while for soft processes non-perturbative effects dominate. The separation is realised by calculating the cross section of the hard processes up to the factorisation scale μ_F^2.
The leading order (LO) cross section for a process $pp \to AB$ can be expressed by a convolution of the PDFs with the cross sections $\hat{\sigma}_{ij\to AB}$ of the hard partonic process. where i and j indicate the involved partons. With the squared partonic centre-of-mass energy $\hat{s} = x_i x_j s$, the LO cross section is given as

$$\sigma(pp \to AB) = \sum_{i,j} \int \mathrm{d}x_i \int \mathrm{d}x_j \; f_i(x_i, \mu_F^2) f_j(x_j, \mu_F^2) \hat{\sigma}_{ij\to AB}(x_i, x_j, \alpha_s, \hat{s}) \; . \quad (2.21)$$

In order to include higher order corrections like next-to-leading order (NLO) or next-to-next-to-leading order (NNLO) QCD contributions, a *K-factor* is introduced. It describes the ratio between calculations for cross sections with higher order contributions and the leading order cross section, e.g. for NNLO

$$K = \frac{\sigma_{NNLO}}{\sigma_{LO}} \quad . \quad (2.22)$$

Thus processes can be simulated with LO cross sections and the overall rate can later be corrected for contributions from virtual loops, initial and final state radiation, determined by higher order QCD calculations.

2.3.3. Hadron Collision Characteristics

Alongside hard interactions resulting in quarks or gluons, partons can also radiate collinear and low energy quarks and gluons from the initial and final state of each process. These higher-order QCD processes are called initial state radiation (ISR) and final state radiation (FSR). Parton shower algorithms are used to model ISR and FSR processes, which are not covered by matrix element calculations. The probability for these radiations can be determined by the DGLAP equations and calculated up to a cutoff value for the radiated parton's energy.
For energies above the cutoff value, perturbative calculations can not be used due to the long-distance structure of QCD. Instead, the partons in each shower are combined to colourless hadrons, since confinement implies only bound free states of quarks or gluons. This part of shower evolution is called *hadronisation* or *fragmentation*. Different models are used to describe hadronisation, e.g. the *string*

fragmentation and the *cluster fragmentation* are used in various generators, currently employed in the ATLAS simulation chain [44–47].
The physics objects arising from these QCD particle showers are referred to as *jets*.

Pile-Up and Underlying Event Since bunches of protons are collided at the LHC, typically several proton interactions are recorded per event. Multiple vertices emerging from interactions within the same bunch crossing are called *in-time pile-up*. Additionally, *out-of-time pile-up* emerges from overlapping signals in the detector from neighbouring bunch crossings. Typical numbers of interactions per crossing for 2012 are ~ 20, as shown in Fig. 2.8.

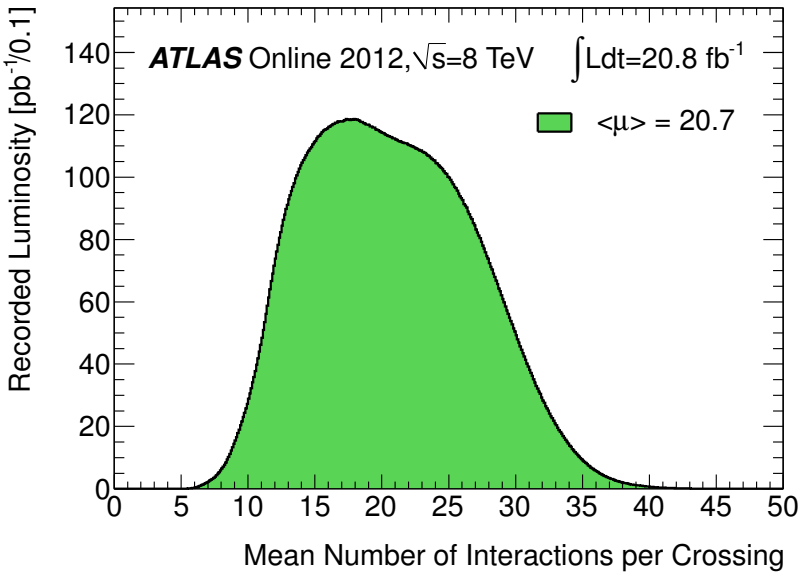

Figure 2.8.: Luminosity-weighted distribution of the mean number of interactions per bunch crossing for 2012 [48].

Additional contributions for each event come from interactions of the remaining partons, the proton remnants, after the hard scattering in a pp collision. These multiple parton interactions together with interactions involving beam remnants are called *underlying event* (UE). The description of the UE requires non-perturbative phenomenological models, which are tuned to LHC data [49].

3. Experimental Setup

The *Large Hadron Collider* (LHC) located at CERN, the European Organisation for Nuclear Research in Geneva is the largest and most powerful particle collider in the world. The experimental results presented in this thesis are based on data which were recorded with the ATLAS detector, one of four main experiments at the LHC. This chapter gives a short overview of the LHC's experimental facility and the performance up to 2012, followed by a description of the ATLAS detector and its components.

3.1. The Large Hadron Collider

The LHC is a proton-proton (pp) collider with a design centre-of-mass energy of $\sqrt{s} = 14$ TeV. It is installed in the tunnel of the *Large Electron Positron* (LEP) collider, a synchrotron running between $1989 - 2000$ at CERN. The tunnels lie underneath the ground with a circumference of approximately 27 km. The vacuum and magnet systems of the two separate beam pipes allow for a second operation mode of the LHC - collisions of heavy ions, e.g. lead, at a design centre-of-mass energy of 2.76 TeV/ Nucleus.

In Fig. 3.1 a sketch of the LHC complex and its pre-accelerators is shown. Starting from a canister of hydrogen gas, protons are produced by ionisation and injected into the *Linear Accelerator* LINAC2. After being accelerated to 50 GeV the protons enter the *Proton Synchrotron Booster* (BOOSTER), which injects them in the *Proton Synchrotron* (PS) with a energy of 1.4 GeV. Before leaving the PS and entering the *Super Proton Synchrotron* SPS they are accelerated to 25 GeV. Finally the protons reach the nominal LHC injection energy of 450 GeV in the SPS.

After injection in one of the separate beam pipes of the LHC main ring, the protons are accelerated either clock- or counterclockwise. By using cavities with radio frequency technique the protons are grouped and kept together in bunches while being accelerated to the collision energy; as for 2012 4 TeV per beam. Superconducting

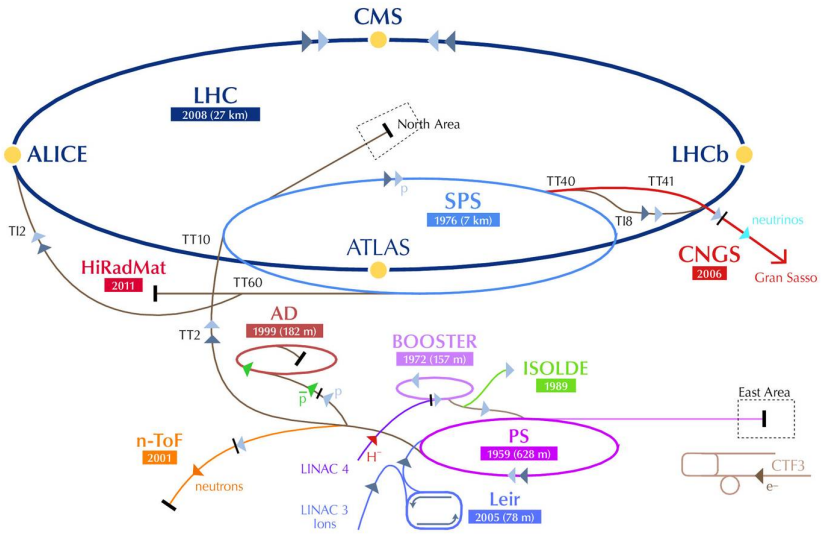

Figure 3.1.: The CERN accelerator complex. After preacceleration by LINAC2, BOOSTER, PS and SPS the protons enter the main LHC ring. At the four main experiments the proton beams collide [50].

dipole magnets with a field of up to 8.33 T are used to keep the proton bunches in their orbit. Quadrupole and higher multipole magnets keep the beam focused and the protons aligned in the bunches. The magnets are cooled by liquid helium to 1.9 K. At design values the energy of each beam will be 7 TeV.

At a collider the event rate for a process with production cross section σ is given by

$$\frac{\mathrm{d}N}{\mathrm{d}t} = \sigma \cdot L$$

where L is the instantaneous luminosity. For the LHC, the latter can be defined as

$$L = \frac{n_b N_1 N_2 f_{\mathrm{rev}} R}{\pi \sqrt{\sigma_{x,1}^2 + \sigma_{x,2}^2}\sqrt{\sigma_{y,1}^2 + \sigma_{y,2}^2}}$$

with the number of bunches n_b, the number of protons per bunch for both beams $N_{1/2}$ and the revolution frequency f_{rev}, also referred to as bunch spacing $1/f_{rev}$ [51]. The factor R takes luminosity reducing effects into account. The denominator describes the width of both beams in x and y dimension. Hence a smaller beam width corresponds to higher luminosity. The LHC is designed to reach an instantaneous luminosity of $L = 10^{34}\ \mathrm{cm}^{-2}\mathrm{s}^{-1}$ with 2808 bunches per beam and a bunch spacing

of 25 ns [52].

The four main detectors are situated at four collision points along the beam pipes. These experiments are dedicated to certain physics topics and use different methods to achieve their goals. Namely

- ATLAS and CMS are multi-purpose detectors, mainly designed to detect new physics and the Higgs boson [53, 54].
- the ALICE experiment is designed to cope with the lead ion collisions to study the quark-gluon plasma [55].
- LHCb is designed to study b-physics, especially $\mathcal{CP}$-violating processes in the b-sector [56].

Performance of the LHC The very first beam circulated on September 10th 2008. In November 2009 the first collisions at 450 GeV beam energy were successfully detected by all four experiments. On March 30th 2010 the first pp collisions at $\sqrt{s} = 7$ GeV were performed, marking the start of the LHC research programme.

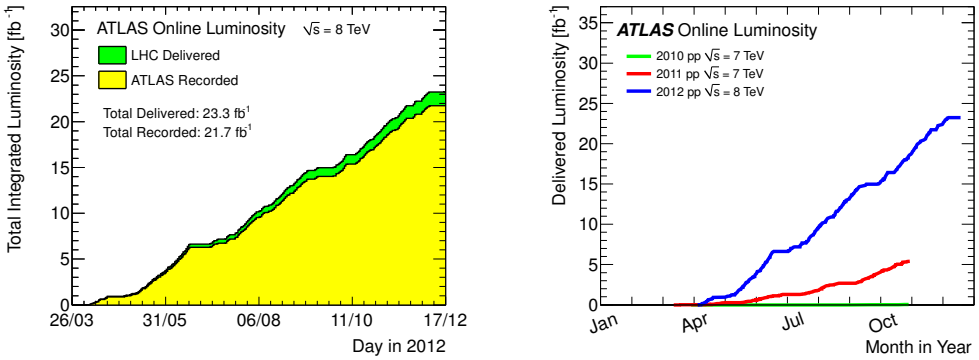

Figure 3.2.: The integrated luminosity for 2012 (left) and a comparison of the delivered integrated luminosities between 2010 and 2012 (right) at the ATLAS experiment [48].

Figure 3.2 shows the delivered integrated luminosity for 2012 and a comparison to the years before. In 2010 the LHC reached a peak luminosity of $L = 2.05 \cdot 10^{32}$ cm^{-2}s^{-1}, twice the expected value [51]. The ATLAS detector recorded 45 pb^{-1} of data. Increasing the luminosity of the LHC up to a peak value of $L = 3.65 \cdot 10^{33}$ cm^{-2}s^{-1}, ATLAS was able to record 5 fb^{-1} in 2011, five times the target integrated luminosity. In 2012, the centre-of-mass energy was increased up

to $\sqrt{s} = 8$ TeV, and the LHC reached a peak luminosity of $L = 7.73 \cdot 10^{33}$ cm^{-2}s^{-1}. Overall, the ATLAS detector recorded 20.1 fb^{-1} data in 2012 at $\sqrt{s} = 8$ TeV.

3.2. The ATLAS Experiment

ATLAS is the largest physics collaboration in the world with about 3000 physicists from over 40 countries. The ATLAS detector is one of the LHC's two multi-purpose detectors. With a length of 44 m, a height of 25 m and a weight of 7000 t it is the largest detector at CERN. Designed to be sensitive to new physics - hence covering a broad range of physics - the detector has to cope with the two main challenges set by the LHC: the high event rate and the large QCD background produced in the collisions of the proton bunches. The latter requires a very precise particle identification which has to be combined with robust detector elements to handle the extreme occupancy and radiation hardness.

The detector has an onion like shell structure as shown in Fig. 3.3. Starting around the beampipe the *inner detectors* are immersed in a *solenoid magnetic field* and surrounded by the *electromagnetic* and *hadronic calorimeter systems*, the *muon spectrometer* and the *toroid magnet systems*. The detector components are described in the following sections.

Coordinate system For defining a position at ATLAS a right-handed coordinate system is used, its origin being the centre of the detector. The x-axis points to the middle of the LHC, the y-axis upwards and the z-axis along the beam pipe. Because of the detectors cylindrical shape the azimuthal angle ϕ in the xy-plane and the pseudorapity η, defined as

$$\eta = -\log\left[\tan\left(\frac{\theta}{2}\right)\right]$$

with the polar angle θ in the yz-plane are commonly used. The pseudorapity η is a high momentum approximation ($p \gg m$) of the rapidity y. An advantage of using the rapity is that the QCD particle production rate is constant per rapidity interval. Furthermore rapidity intervals remain constant under Lorentz transformations. The same holds approximately for the pseudorapity η.

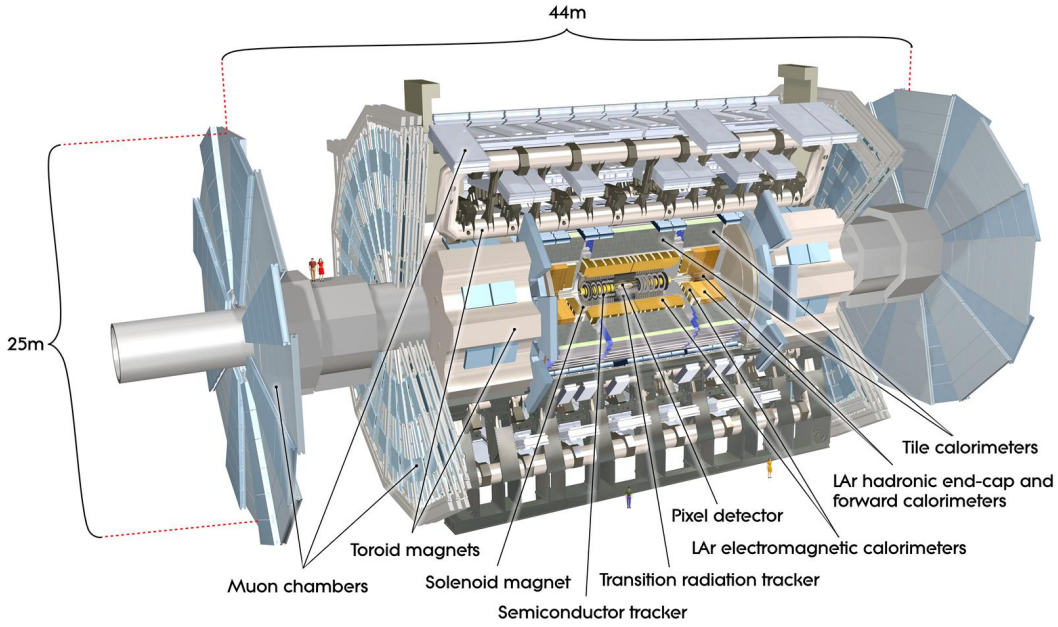

Figure 3.3.: The ATLAS detector with highlighted main components [53].

Angular distances between objects are commonly described by the variable

$$\Delta R = \sqrt{\Delta\eta^2 + \Delta\phi^2} \ .$$

Since protons contain partons moving at various fractions of the protons momentum the initial momentum and energy of interacting particles is not known. Nevertheless the sum of initial momentum and energy in the xy-plane are both 0. Hence it is useful to describe particles using the *transverse momentum* p_t and the *transverse energy* E_t defined as

$$p_t = \sqrt{p_x^2 + p_y^2} \quad \text{and} \quad E_t = \sqrt{E_x^2 + E_y^2} \quad .$$

An imbalance in transverse energy allows for a quantification of undetectable particles such as neutrinos and is quantified by the *missing transverse energy* $\not{E}_T$.

3.2.1. Inner Detectors

Closest to the interaction point is the Inner Detector (ID), designed for precision tracking of charged particles and vertex measurements. The ID, as shown in Fig. 3.4 (left), consists of the three components *pixel detector*, *semiconductor tracker* (SCT) and *transition radiation tracker* (TRT). Along the z-axis the components are divided in a barrel region and end-cap disks as sketched in Fig. 3.4 (right).

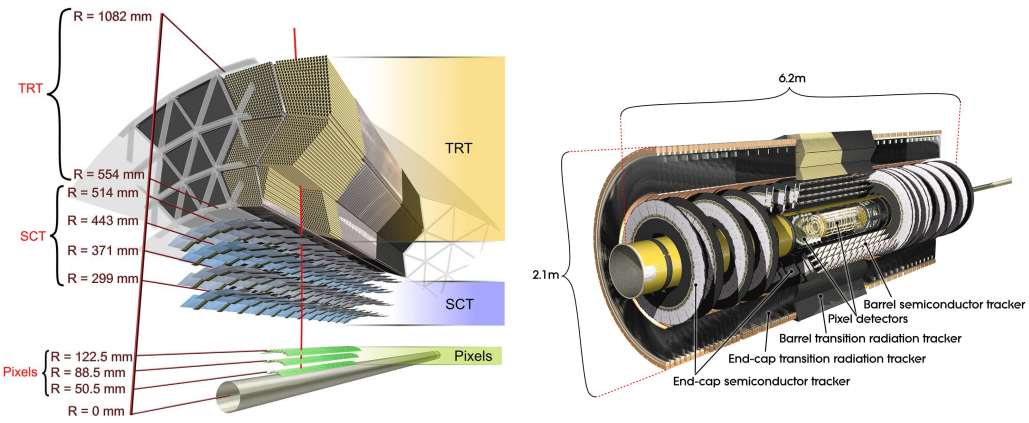

Figure 3.4.: Schematic cut-away views of the ATLAS inner detector. On the left a cross section of the ID-layers are shown and on the right the overall layout is presented [53].

The innermost part of the ID is the pixel detector consisting of approximately 80 Million silicon pixel sensors. Each of the pixels is read out separately by front-end chips which are bump-bonded to the pixels. The three pixel layers allow for a measurement of charged tracks within $|\eta| \lesssim 2.6$. The pixel detector's resolution is up to 12 µm. Because of a performance loss due to the very high radiation close to the beam pipe an additional layer, the *insertable-b-layer* (IBL) will be installed during the shutdown of the LHC in 2013 [57].

The pixel detector is followed by the SCT which uses semiconducting silicon strips for track measurements. Each of the four barrel layers consists of single sided silicon microstrip detectors glued back-to-back. The strips are aligned with a stereo angle to provide a measurement of the azimuthal angle in each layer. The SCT barrel region together with its 9 end-caps cover the range $|\eta| \lesssim 2.5$ and reaches a maximum

resolution of 17 µm [58].

The third part of the ID is the TRT, which comprises about 400 000 straw tubes. It consists of a barrel region and two end-caps. Around the straws foils with different dielectric constants are placed, such that traversing charged particles produce transition radiation, allowing for an identification of different charged particles, i.e. electrons and pions. Tracking information from the TRT with a typical per-straw resolution of 130 µm are combined with the other ID components to increase the precision of the transverse momentum measurement [58].

3.2.2. Calorimeter Systems

For energy measurements a calorimeter system is used in ATLAS. Traversing particles deposit their energies in the calorimeter cells by interaction with the material, undergoing the so-called *showering*. By using alternating layers of dense and active material, the particles' deposited energy in the calorimeter systems can be measured. Since the deposition of energy depends on the particles type, the calorimeter system consists of the electromagnetic and the hadronic calorimeter (ECAL and HCAL).

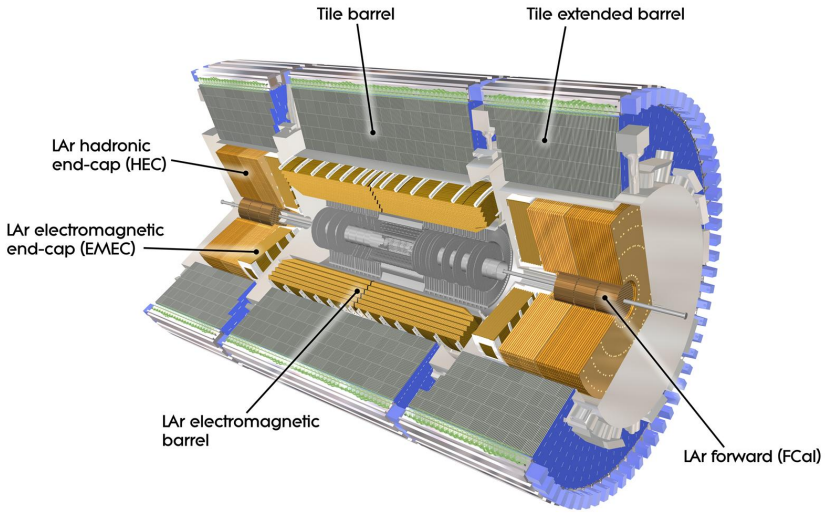

Figure 3.5.: A labelled scheme of the ATLAS detector's calorimeter system showing its subdetector systems [53].

By electromagnetic interaction with the material, namely bremsstrahlung and e^+e^- pair-production, high-energetic electrons and photons traversing the ECAL are

stopped. Lead and copper are used as absorber material and liquid argon as active material to measure the energy of the charged particles produced by showering. As shown in Fig. 3.5 the ECAL is split in the barrel region and two end-caps. It covers a range of $|\eta| \lesssim 3.2$. The ECAL is designed to stop the majority of electrons and photons by depositing all of their energy in the calorimeter.

Hadronic particles need more and denser material to deposit their energy since they are typically minimum ionising particles and need to interact hadronically to undergo showering. Surrounding the ECAL, the HCAL is divided into three parts. The *tile calorimeter* in the barrel region with $|\eta| \lesssim 1.8$ uses steel as absorber and scintillators together with wavelength-shifting fibres as active material [59]. Covering a range up to $|\eta| = 4.9$, the hadronic end-caps (HEC) and the forward calorimeter (FCAL) use liquid argon for measuring the deposited energy and tungsten and copper as absorber.

All calorimeter parts are finely granulated. The barrel-region is constructed with a unique accordion structure. The calorimeter's energy resolution can be parametrised as

$$\frac{\sigma_E}{E} = \underbrace{\frac{a}{\sqrt{E}}}_{\text{stoch.}} \oplus \underbrace{\frac{b}{E}}_{\text{noise}} \oplus \underbrace{c}_{\text{sys.}}$$

with a stochastic, a noise and a systematic term. The number of particles produced in a shower is proportional to the energy E of the incoming particle. The resolution therefore contains a stochastic term following the Poisson statistics. The relative noise contribution in the calorimeter cells is proportional to $1/E$. Finally dead detector material and other systematic uncertainties decrease the resolution by a constant term c.

3.2.3. Muon Spectrometer

The muon spectrometer (MS) is the outermost component of the detector, pictured in Fig. 3.6. By ionisation and excitations of surrounding atoms massive charged particles loose energy when traversing through matter. Muons with energies of the order $10 - 100$ GeV are minimum ionising particles (MIP) according to the Bethe-Bloch-formula [1]. Hence, they traverse through the ID and calorimeters only depositing small amounts of their energy.

For detecting muons and measuring their transverse momenta the MS comprises four components. The *monitored drift tubes* (MDT) are gas filled drift chambers used for tracking in the barrel region $|\eta| < 2.0$. In the same region *Resistive plate chambers* (RPC) are used for triggering and position measurement. In the end-cap region $2.0 < |\eta| < 2.7$ *thin gap chambers* (TGC) trigger muon events. The *cathode strip chambers* (CSC) are used for tracking traversing muons in the end-cap region.

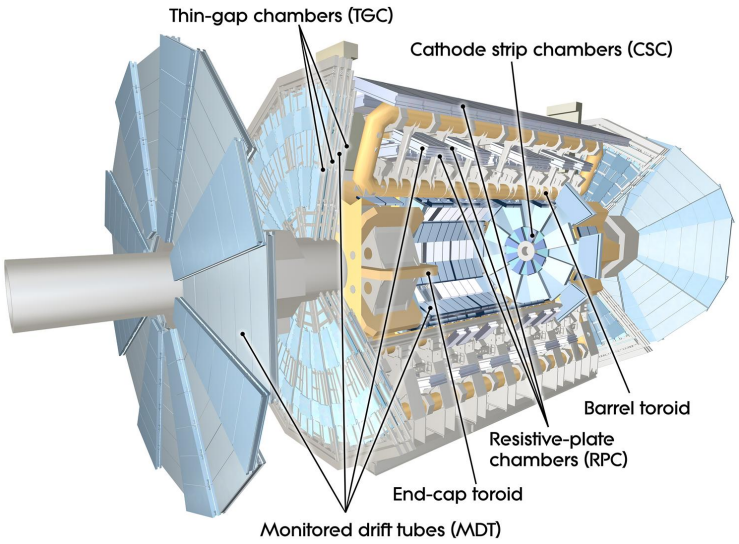

Figure 3.6.: A labelled scheme of the muon system. The tracking and trigger components are shown [53].

For muons with energies $10 - 200$ GeV the p_t-resolution of the MS is up to 3 %. For very high momentum ~ 1 TeV the p_t-resolution is approximately 10 %. Since the MS extends from a radius of 4.25 m out to the full detector radius of 11 m, an accurate measurement of the muon tracks is possible.

3.2.4. Magnet System

A significant difference between the ATLAS and the CMS detector is the outer magnetic field. While the CMS detector uses one solenoidal field ATLAS uses two separate fields, a solenoid field within the ID and a toroidal field encompassing the MS. Both magnetic fields are used to perform measurements of momenta by bending the tracks of charged particles. The solenoid inner magnetic field has a field strength of 2 T. The toroid systems provide a non-uniform average field of 0.5 T. By the curvature of their tracks, the momenta of charged particles can be measured. The error on

the curvature decreases with increasing measured values. Since the p_t is inversely proportional to the curvature, the resulting resolution on the muon p_t decreases with increasing p_t.

3.2.5. Trigger System

Due to the high luminosity of the LHC, a three-level trigger system is used. With a bunch spacing of 25 ns an event rate around 40 MHz and approximately 25 interactions per event is achieved. Since the majority of events are soft QCD interactions only events which are of interest for physics need to be recorded [60]. With the full trigger system, the recorded event rate is reduced to 200 Hz.

The three trigger levels are

- the hardware-based **Level-1** (LV1) trigger which reduces the event rate to 75 kHz using only the information from muon chambers and the calorimeter. Before passing the event to the next trigger level, a region-of-interest (ROI) is defined. The LV1 trigger's decision time or *latency* is 2 µs.
- the software-based **Level-2** (LV2) trigger combines information from LV1 and the ROI for each detector trigger component separately to determine the pass or failure of an event. The event rate is reduced to an order of 1 kHz with a latency of $\sim$ 10 ms.
- the software-based **Event Filter** (EF) uses the full event information from offline algorithms including tracking and jet reconstruction for decision-making. The event rate is decreased to 200 Hz and the decision time is approximately 4 s.

In-between the three stages, each event passing LV1 is buffered until the high-level triggers are ready for processing. Events passing the EF are stored permanently [60].

With so-called *trigger menus*, selections of different trigger signatures are collected. The trigger menus depend on the data taking conditions and hence ensure an optimal usage of the available band width.

4. Object Reconstruction and Definitions

A particle traversing the ATLAS detector produces characteristic signals in the different detector components. Using a variety of reconstruction algorithms, the raw data delivered by the detector can be converted to physics objects which are suitable for physics analysis.
In the following, the reconstruction algorithms for the physics objects used for the analysis in this thesis are briefly discussed. The object definitions used in this thesis are summarised and follow the recommendations of the $H \to \tau^+_{\text{lep}}\tau^-_{\text{lep}}$ group for 2012 collision data [61].
In order to achieve a better description of data from MC simulation, scale factors for the reconstruction and identification efficiencies of electrons and muons, as well as the trigger efficiency are applied to all MC samples.

4.1. Leptons

Muons In this thesis, muons which were reconstructed with the STACO algorithm are used [26].
Because of their minimum ionizing nature, muons with $p_t \gtrsim 6$ GeV are typically able to reach the muon spectrometer. In the STACO algorithm, tracks in the muon spectrometer are extrapolated to the beam line, forming standalone muons. Muons also leave a track in the inner detector. These inner detector tracks are combined with the MS tracks within the STACO algorithm by a matching procedure incorporating a global fit [62].

The muon's momentum, measured from track curvature, is corrected for energy loss in the calorimeter and required to be $p_t > 10$ GeV. In order to reduce the misidentification rate, several quality criteria for the inner detector tracks are applied as recommended by the muon combined performance group [63]. The muons are required to lie within $|\eta| < 2.5$, according to the instrumented region of the muon spectrometer. Cosmic and beam-induced backgrounds are reduced by requiring the

z-position of the origin of the muon's inner detector track to be close to the z-position of the primary vertex, which has to be smaller than 1 cm. In order to reject muons produced in semileptonic quark decays, isolation criteria are defined. The transverse energy in the calorimeter cells in a cone of $\Delta R < 0.3$ around the direction of the muon candidate's track, called *etcone*30, has to be less than 14 % of the muon's p_t. Additionally, the sum of all tracks with $p_t > 1$ GeV around the muon, called *ptcone*30 must be smaller than 13 % of the muon's p_t.

For a better agreement between data and simulation, the muons' momenta and resolution are smeared in the simulation to match the observations in data.

Electrons For the reconstruction of electrons, energy deposits in the electromagnetic calorimeter are used in the cluster-based sliding window algorithm [64]. The reconstructed electron candidates from the energy deposit are required to have an associated inner detector track, to exceed $p_t > 15$ GeV and to lie within the inner detector coverage, i.e. $|\eta| < 2.47$. The transition between barrel and endcap region $1.37 < |\eta| < 1.52$ is excluded, as electrons are difficult to describe in this *crack-region*. The identification quality is controlled, by requiring the electrons to pass the *mediumPP* criterion, constructed from several geometrical cluster shape observables, TRT and HCAL information, as well as track matching quality information [64]. Like in the case of the muons, electrons need to be isolated to suppress QCD background. The isolation is realised by the same cuts on *etcone*30 and *ptcone*30 as for the muons.

In order to avoid the reconstruction of physics objects from the same local detector response, an overlap removal is applied. On that account, electrons are removed from the event, if they are within a distance of $\Delta R < 0.2$ of a reconstructed muon.

As for the muons, the electrons' energy resolution is smeared in the simulation to match the observations in data. Furthermore, the energy of the electron is corrected in data with factors determined in in-situ calibration studies.

Taus Hadronically decaying tau-leptons τ_{had} are reconstructed to suppress $Z \to \tau_{\text{had}}\tau_{\text{had}}$ and $W \to \tau_{\text{had}}\nu$ background contributions in the selection and to remove overlaps with the $H \to \tau^+_{\text{had}}\tau^-_{\text{lep}}$ and $H \to \tau^+_{\text{had}}\tau^-_{\text{had}}$ analyses. Characteristic for a τ_{had} candidate is a collimated shower profile with a small amount of associated tracks. Energy deposits in the calorimeter are used to reconstruct the τ_{had} candidate, while a boosted decision tree discriminator is used to reject jets faking the hadronically

decaying tau signal [65]. A τ_{had} candidate must have one or three associated tracks, corresponding to one or three charged pions from its decay. Furthermore, the candidate is required to have $p_t > 20$ GeV and a total charge of ± 1. Only taus within $|\eta| < 2.5$ are considered. If the τ_{had} is within a distance $\Delta R < 0.2$ of an electron or muon, the tau-lepton is removed from the event.

4.2. Jets

Starting from *topological clusters* in the calorimeter, jets are reconstructed with the anti-k_t algorithm [66–68]. In this algorithm, calorimeter clusters with an energy deposit above a given threshold are merged with the surrounding clusters, if the latter fulfil a threshold criterion based on the distance ΔR. For jets in the analysis, $\Delta R = 0.4$ is used.

In order to interpret the objects formed by the algorithm as physical jets, it is crucial to understand the translation of the detector response back to the energy of the hadronic particle, called jet energy scale (JES). In the EM+JES scheme, jets are reconstructed from energy depositions in the calorimeter at the electromagnetic energy scale (EM) and corrected for non-compensation, as hadrons induce a lower calorimeter response than electrons. These depositions are furthermore corrected for e.g. dead detector material, energy loss due to particles escaping the calorimeters and signal losses in the calorimeter. The calibration is depending on the jet's p_t and η [65, 69].

After the calibration, a threshold of $p_t > 20$ GeV is set for the jets. Jets are only used if they are within $|\eta| < 4.5$. If a jet candidate is identified as out-of-time activity or calorimeter noise, the whole event is discarded. Jets originating from pile-up activity are suppressed by requiring the jet vertex fraction (JVF) to be $|\text{JVF}| > 0.5$ for jets within $|\eta| < 2.4$. The JVF is defined as the p_t sum of all tracks matched to a jet from the primary vertex divided by the total p_t-sum of jet-matched tracks.

In order to suppress top-quark processes like $t \to Wb$, jets originating from b-quarks need to be identified. B-mesons, formed from the b-quarks have a long lifetime of ~ 10 sec and thus a large flight length of ~ 1 mm [70]. The decay of these mesons gives rise to a displaced secondary vertex and a large *impact parameter*. b-tagging algorithms exploit this topology to distinguish between light jets and heavy b-jets by associating a weight to each jet.

In this analysis, the neural network-based b-tag algorithm MV1 is used to identify b-jets [71]. MV1 combines the weights of the b-tagging algorithms SV0, IP3D and JetFitterCombNN [72]. At a working point of MV1 weight = 0.795 the algorithm has an efficiency of 70 %. By applying b-tagging scale factors, differences between data and MC b-tag efficiency and mistag rates are accounted for [73].

If the jet candidate is within a cone of $\Delta R < 0.2$ of a selected muon, electron or tau it is removed from the event .

4.3. Missing Transverse Energy

Events with undetected particles in the final state, e.g. neutrinos from a τ-lepton decay, are characterised by large missing transverse energy. For the measurement of $\not{E}_T$, an object based algorithm, called *RefFinal* is used, combining information from energy measurements in the calorimeters and muon momentum measurements in the MS. Following the selection criteria above, the transverse energy from electrons and photons with $p_t > 10$ GeV, from anti-k_t jets with $p_t > 20$ GeV as well as jets calibrated at the electromagnetic scale with 7 GeV $< p_t <$ 20 GeV are included in the calculation of $\not{E}_T$. Furthermore, the p_t of the muon measured in the MS and energy from topological clusters not associated to high-p_t objects, the *cell-out* terms, are taken into account.

In order to avoid a loss in Higgs mass resolution and to suppress contributions from energy deposits from pile-up activity, a weighting of the calorimetric contributions according to their relation to the primary vertex is applied.

Another definition of missing transverse energy, the $\not{E}_T^{\mathrm{HPTO}}$ is considered. This quantity is build from the leptons and jets in the event, according to

$$\not{E}_T^{\mathrm{HPTO}} = \sqrt{(-\sum_{\mathrm{l=lep}} p_x^l - \sum_{\mathrm{j=jet}} p_x^j)^2 + (-\sum_{\mathrm{l=lep}} p_y^l - \sum_{\mathrm{j=jet}} p_y^j)^2} \tag{4.1}$$

and well correlated with $\not{E}_T$ for events with neutrinos in the final state. For $Z \to ee/\mu\mu$ events, there is only a loose correlation between the two definitions, hence $\not{E}_T^{\mathrm{HPTO}}$ is employed to suppress this Drell-Yan background contributions.

5. Physics Process Modelling and Datasets

Simulations of high energy physics processes are crucial components for data analysis at the LHC experiments. Physics processes as well as detector responses can be modelled by Monte Carlo (MC) simulation techniques.
Simulated objects are reconstructed with the same algorithms as real data objects and fed into the identical analysis chain to ensure consistency. Therefore, predictions for experimental observables from MC simulations can be exploited to distinguish signal from background contributions, to determine signal selection efficiencies and to optimise data taking methods, like the trigger system.

In the next sections, an overview of the ATLAS event simulation procedure is given, followed by a description of the MC event generators and data samples used in this study.

5.1. MC Event Simulation

In Fig. 5.1, the MC event production at ATLAS is sketched. The event generation,

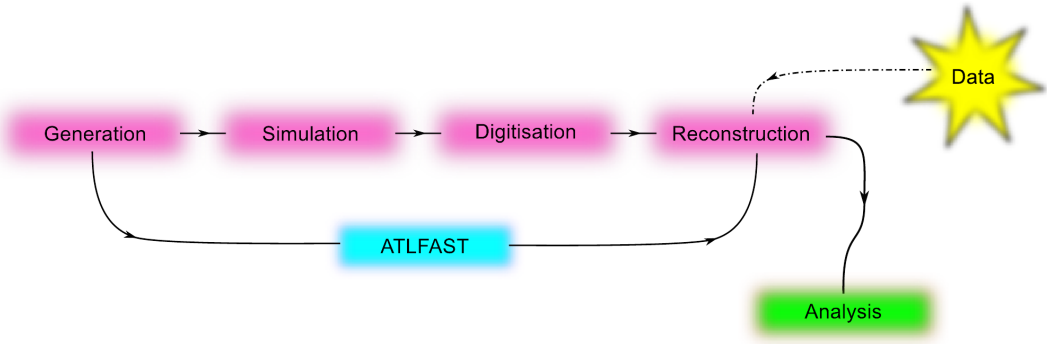

Figure 5.1.: The MC simulation chain at ATLAS.

described in the next section, yields momentum four-vectors of particles in the final

state of the simulated process. These are passed to GEANT4, a software framework for MC-based simulation of the interaction between particles and matter [74].
Using a detailed description of the ATLAS detector, the detector's response to the traversing particle is simulated. After a digitisation of the detector simulation output, the output objects include the same information as real, raw detector data and can hence be fed into the same reconstruction software. From the detector data, tracks and energy depositions are reconstructed. Successively, the physics objects are reconstructed in analogy to data, i.e. by algorithms described in Sec. (4). For the final analysis, a data format only containing the reconstructed objects and little additional information is used.

In order to avoid the CPU intensive full simulation chain, a fast simulation, called ATLFAST II, combining simulation, digitisation and reconstruction into one step, is available [75]. By using a parametrisation of the ATLAS detector, the generator output is directly converted to analysis objects. Thus, high statistics samples can be achieved with comparably small CPU consumption. A disadvantage of using the ATLFAST II program is a less detailed detector description, which is required for precision measurements.

5.2. MC Event Generation

MC event generators simulate the full decay chain of a process. Following the factorisation theorem in Equ. 2.21, hard processes and parton showers can be separated from non-perturbative QCD effects in the event generation. Specific programs are used to generate the hard process final states and are interfaced with programs capable of simulating the non-perturbative evolution of the final states including hadronisation, the decay of the hadrons and simulation of underlying events. Figure 5.2 shows a sketch of the successive event generation steps. In the following, the generators used in this analysis are briefly introduced.

Alpgen ALPGEN is a tree-level matrix element generator, specialised on the simulation of hard scattering processes using perturbative QCD [76]. Using exact leading order (LO) matrix element calculations for different parton multiplicities, a wide range of processes can be simulated. Processes like $Z + jets$, are split in different parton multiplicities in the matrix element from $0 - 5$ and the three lepton flavours for simulation. For simulation of parton showering and hadronisation, ALPGEN is

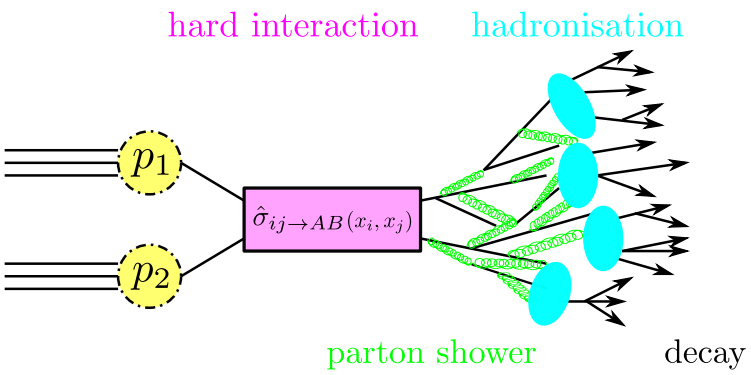

Figure 5.2.: Schematic view of the different Monte Carlo event generation steps.

interfaced with full event generators, described in the following.
In order to avoid double counting of events, overlapping jets from the LO calculation and the parton showering are matched following the MLM-matching scheme [77, 78]. The overlap primarily occurs for high-p_t jets or wide-angle gluon emission.
Following a study in 2011 data, all ALPGEN $Z + jets$ samples are corrected for a mis-modelling of the Z-rapidity by a scale factor of 1.06 [79].

Pythia Non-pertubative QCD evolution of final states can be simulated with the general purpose showering and hadronisation generator PYTHIA [46]. By providing phenomenological models, contributions from multiple parton interactions and pile-up contributions can be calculated. PYTHIA uses the Lund string fragmentation model to describe the hadronisation of partons. The underlying event contributions are modelled using a colour string fragmentation model and p_t ordered (PYTHIA 6) or angular ordered parton showers (PYTHIA 8).

Herwig Another general purpose generator is HERWIG [80]. Using angular ordered parton showering, a large range of hard processes can be simulated, including ISR and FSR. Hadronisation and underlying events are modelled using a cluster algorithms. JIMMY, an extension of the HERWIG generator, tuned with first collison data in 2010, takes into account all remnants of the interacting protons, thereby describing multiple parton interactions [81, 82] .

Sherpa SHERPA is a general-purpose event generator using a dipole formulation for parton showering and a cluster fragmentation model for hadronisation [83]. SHERPA is able to perform stand-alone merging of LO matrix element jet production for

different parton multiplicities with parton showers. For this, the CKKW matching scheme is used, to avoid double counting and enable large final state multiplicity simulations. For simulation of multiple parton interactions, a PYTHIA -based model is used.

MC@NLO Since the MC@NLO generator uses full next to leading order (NLO) QCD calculation, a more precise description of radiation can be achieved compared to other generators [84]. Soft, collinear emissions are simulated by interfacing MC@NLO with HERWIG. The resummation technique used for implementation of NLO QCD corrections can lead to negative event weights.

PowHeg Another generator using full NLO QCD calculations is POWHEG [85]. Starting from the simulation of hardest radiation, the exact NLO matrix elements are used for the corrections with a method yielding only positive event weights. POWHEG can be interfaced with other generators like PYTHIA for parton showering and hadronisation.

5.3. Datasets and Cross Sections

In this section, the data and MC data samples together with their cross sections used for this thesis' study are presented. All MC data samples were simulated at $\sqrt{s} = 8$ TeV.
For modelling of the τ-lepton decays, the program TAUOLA is interfaced with the generators [86, 87]. PHOTOS models photon radiation in decays produced by PYTHIA , MC@NLO and HERWIG [88].
The simulation of the processes is done in (N)LO. When weighting the events from each sample, a global K-factor, as definded in Equ. 2.22, is used to scale the events according to the highest-order cross section available. Differential shapes are not influenced by this scaling but the event yields correspond more precisely to the actual cross section. The properties for the Higgs boson, the top-quark, the W-bosons and the Z-boson used in the event generation are depicted in Tab. 5.1 [8].

Higgs boson production The production of the SM Higgs boson with a mass of $m_H = 125$ GeV in the vector boson fusion channel was simulated using POWHEG interfaced with PYTHIA 8 with the AU2 tune [89]. Only $H \to \tau^+\tau^-$ decays with

Particle	Mass [GeV]
Higgs boson	125
top quark	172.5
W-boson	80.4
Z-boson	91.19

Table 5.1.: Masses of the Bosons used for the event generation.

both taus decaying leptonically were considered in the simulation. For description of the proton's structure the PDF-set CT10 was used [90].
The cross section is calculated at next-to-next-to leading order (NNLO), following the prescription of the LHC Higgs cross-section working group (HSXWG) [91]. For this calculation, the program VBF@NNLO was used [92]. The branching ratio of $H \to \tau^+\tau^-$ is determined by the programs HDECAY and PROPHECY4F [93–95]. For $H \to \tau^+\tau^-$ decays, the branching ratio is determined to be 6.32% [96].

$Z/\gamma^* \to \ell^+\ell^- + jets$ production The simulation of background contributions from Z-bosons and photons γ^*, also referred to as Drell-Yan (DY) background, is done using ALPGEN interfaced with PYTHIA 6 with the Perugia2011C tune [49]. The samples are simulated for the low-mass region 10 GeV $\leq m_{\ell\ell} \leq$ 60 GeV and high-mass region $m_{\ell\ell} >$ 60 GeV and for each lepton channel $\ell = e, \mu, \tau$ separately. As previously mentioned, the simulation is done separately for each parton multiplicity n - exclusively for $n = 0, ..., 4$ and inclusively for $n \geq 5$. The production is simulated at a renormalisation and factorisation scale of $m_Z^2 + p_t^2(Z)$ using the LO PDF set CTEQ6L1. The MLM-matching is done using a cut of $p_t < 20$ GeV for jets originating from the parton showering simulation. The FEWZ code is used to calculate the cross-sections for each sample in NNLO QCD [97].

VBF $Z \to \ell^+\ell^-$ production Since the VBF production modes of $Z \to \ell^+\ell^-$ events are not implemented in ALPGEN, SHERPA is used to simulate these processes. The production of a Z boson together with 2 jets in the VBF mode is simulated using the CT10 PDF set.

$W^\pm(\to \ell^\pm\nu) + jets$ production Background events with a W-boson and $jets$ were simulated using ALPGEN interfaced with HERWIG and JIMMY in the AUET2

tune [98]. The PDFs are modelled using the CTEQ6L1 set [40]. As in the $Z + jets$ sample, the production is split into different parton multiplicities from $n = 0, .., 5$ in the ME and the cross-sections are calculated in NNLO QCD using the FEWZ code. The associated partons produced with the W-boson are light quarks u, d, s and heavy quarks c, b. The inclusive $W + jets$ samples contain both, light and heavy quarks, the latter being simulated in the parton showering. In order to cover all final states, additional samples containing the W-production in association with heavy quarks ($W + bb/cc/c + jets$) are considered. The overlap between these samples, mainly originating from gluon splitting in the light samples, is removed using the heavy flavour overlap removal tool [99].

Diboson production The electroweak production of pairs of vector bosons, namely events with WW, ZZ and WZ was generated using HERWIG, which includes all decay modes for the vector bosons [61]. The HERWIG configuration followed the AUET2 tune and used the CTEQ6L1 PDF set. The NLO cross section was calculated using POWHEG and MC@NLO [100]. At least one lepton is required at generator level.

Top-quark production For estimating the background contributions from events involving top-quarks, top-pair $t\bar{t}$, as well as single-top production are considered. For the generation of the $t\bar{t}$ sample, MC@NLO interfaced with HERWIG and JIMMY for parton showering in the AUET2 tune is used. The cross section was calculated for NLO + next-to-next-to leading logarithmic (NNLL) pQCD [101]. For the generation, the CT10 PDF set was used. On generator level, at least one lepton is required.

Single-top production is split in s- and t-channel (according to Mandelstam-variables [1]) and in associated Wt production. The s-channel and the Wt-production were simulated using MC@NLO with HERWIG and JIMMY for parton showering in the AUET2 tune and the CT10 PDF set. The t-channel is generated with the LO generator ACERMC [102] which is interfaced with PYTHIA , tuned according to AUET2B and using the CTEQ6L1 PDF set. Again, the cross sections are calculated in NLO+NNLL pQCD [103].

In Tab. 5.2 an overview for the cross section and statistics of each sample is shown. All values and samples are calculated for $\sqrt{s} = 8$ TeV.

Process	Generator	# Events	σ_{LO} [pb]	K-factor
$Z/\gamma^* \to e^+e^- + jets$	Alpgen + Pythia	10495051	4627.37	1.18
$Z/\gamma^* \to \mu^+\mu^- + jets$	Alpgen + Pythia	10490476	4627.34	1.18
$Z/\gamma^* \to \tau^+\tau^- + jets$	Alpgen + Pythia	10826099	4627.13	1.18
$Z/\gamma^* \to e^+e^- + b\text{-}jets$	Alpgen + Herwig	278999	13.32	1.00
$Z/\gamma^* \to \mu^+\mu^- + b\text{-}jets$	Alpgen + Herwig	279999	13.32	1.00
$Z/\gamma^* \to \tau^+\tau^- + b\text{-}jets$	Alpgen + Herwig	280000	13.31	1.00
$t\bar{t}$	Mc@nlo + Herwig	11550546	129.27	1.00
Single-top (s-chan)	Mc@nlo + Herwig	765108	28.44	1.00
Single-top (t-chan)	Mc@nlo + Herwig	507005	1.82	1.00
Single-top (Wt-chan)	Mc@nlo + Herwig	1767075	22.37	1.00
Di-Boson WW	Herwig	2484694	20.60	1.00
Di-Boson ZZ	Herwig	249999	1.55	1.00
Di-Boson WZ	Herwig	999797	6.81	1.00
$W \to \ell\nu$	Alpgen + Herwig	33130507	30824.62	1.19
$W \to \ell\nu + c$	Alpgen + Herwig	9144274	1170.18	1.19
$W \to \ell\nu + cc$	Alpgen + Herwig	3019294	384.94	1.19
$W \to \ell\nu + bb$	Alpgen + Herwig	1059395	135.32	1.19
VBF $Z \to e^+e^-$	Sherpa	1062084276	0.36	1.00
VBF $Z \to \mu^+\mu^-$	Sherpa	1033356864	0.36	1.00
VBF $Z \to \tau^+\tau^-$	Sherpa	62395460	0.46	1.00
VBF $H(\tau^+\tau^-) \to \ell^+\ell^-$	PowHeg + Pythia	1000000	1.088	1.45

Table 5.2.: Summary of the samples used for this study, the number of simulated events, their LO cross section σ_{LO} and the global K-factors. The $t\bar{t}$ sample does not include the fully hadronic final state.

Dataset During 2012, the ATLAS detector recorded data corresponding to 21.7 fb^{-1} at a centre-of-mass energy of $\sqrt{s} = 8$ TeV. For this analysis, a subset of 13.06 fb^{-1} is used, corresponding to the data recorded in Summer 2012.

A *good run list* (GRL) is used in this study, to assure stable and analysis-suitable data taking conditions. During the data taking, machine and detector conditions change, e.g. due to noisy subdetector systems. For short time periods - luminosity blocks of 1 min - the effects from changing conditions on the quality of the recorded data were studied and encoded in a list of good luminosity blocks for each run. According to this GRL, the dataset was chosen and the corresponding luminosity calculated.
Besides these temporary effects, also permanent machine defects need to be considered. The relevant issues were treated separately as described in Sec. (6.3).

Two different data-streams were considered for the analysis, one containing a trigger menu tuned for physics with electrons and photons and the other for events with muons. The streams are merged, while accounting for doubly recorded events.

6. Studies for VBF $H(\tau^+\tau^-) \to \ell^+\ell^- 4\nu$ Searches

In this chapter, the motivation, strategy and goals of the analysis conducted for this thesis is presented. Furthermore, applied preselection steps are discussed. Finally, an overview of the treatment of systematic uncertainties is given.

6.1. Motivation and Signal Topology

The search for the Higgs boson in $\tau^+\tau^-$ final states is important for the SM Higgs boson searches at the LHC, as the discovery of a Higgs-like boson in Summer 2012 could be confirmed in a fermionic final state.

6.1.1. τ-lepton Decays

A τ-lepton can either decay hadronically or into an electron or muon, each decay channel accompanied with neutrinos. The decay is mediated by a W-boson. The corresponding branching ratios are listed in Tab. 6.1. The main source of background

Process	BR
$\tau \to e\nu_e\nu_\tau$	0.174
$\tau \to \mu\nu_\mu\nu_\tau$	0.178
Hadronic	~ 0.65
$\tau\tau \to \ell\ell 4\nu$	0.124

Table 6.1.: Branching ratios for τ-lepton decays [8].

contributions in hadronic collisions arise from multi-jet events. Although providing the highest branching ratio, a hadronically decaying τ-lepton is difficult to identify, as large backgrounds from light jets in multi-jet events arise. Final states with at least one lepton with large transverse momentum p_t allow for a suppression of the

multi-jet contributions.

As shown in Fig. 2.6, the branching ratio for $H \to \tau\tau$ for low Higgs masses between 110 GeV $< m_H <$ 140 GeV is of the order of 7%. Despite the smaller branching ratios, both τ-leptons are required to decay leptonically in this study. This offers a signature which can be efficiently discriminated from background events, as two leptons and large missing transverse energy $\not{E}_T$ are present in the final state. The branching ratio for both taus decaying hadronically is shown in Tab. 6.1.

When accompanied by a high p_t jet, the Higgs boson acquires a boost in the transverse plane. This enhances the transverse momenta of the Higgs' decay products. As a consequence, the leptons momenta and the energy of the neutrinos from the τ decays are enlarged. This leads to a high $\not{E}_T$ for the signal events, improving the discrimination between signal and background events [104].
When produced by VBF, the signal-to-background ratio can be further enhanced by topological cuts, as will be explained in the following [73].
Three analysis categories are defined according to the lepton flavours in the final state of the $H(\tau^+\tau^-) \to \ell^+\ell^- 4\nu$ process: the ee, the $\mu\mu$ and the $e\mu$ channel.

6.1.2. VBF $H(\tau^+\tau^-) \to \ell^+\ell^- 4\nu$ Topology

In Fig. 6.1, the LO Feynman diagram for the $H(\tau^+\tau^-) \to \ell^+\ell^- 4\nu$ signal process produced in vector boson fusion (VBF) is shown, including the leptonic decays of both τ-leptons. As discussed in Sec. (4), events with a reconstructed hadronically decaying τ candidate are rejected and furthermore not simulated in the signal sample.

The two quarks involved in the VBF process carry only a fraction of the colliding protons' momenta, as described in Sec. (2.3.1). Thus, high, opposite longitudinal momenta and only comparably small transverse momenta are expected for the quarks in the initial state. During the scattering process, the two quarks receive only a small transverse momenta component. For that reason, the jet $j1$, formed by one of the quarks, is expected to propagate in the forward-region and the other jet $j2$, caused by the second quark, in the backward-region of the detector. The jets $j1$ and $j2$ are hence well separated in the pseudorapidity η [20, 105]. The two jets typically form a high invariant mass, as they arise from two independent, high energetic quarks. In the following, the jets $j1$ and $j2$ are referred to as *tagging jets*.
Another characteristic of a VBF event is the location of the leptons relative to the

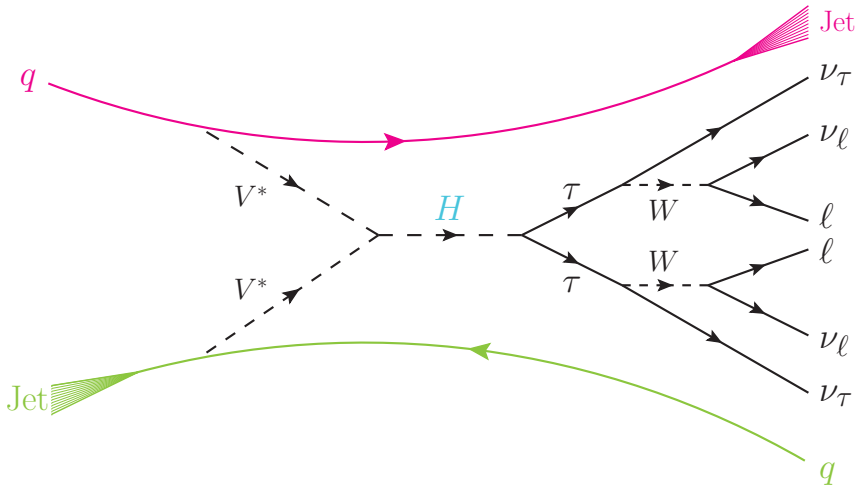

Figure 6.1.: LO Feynman diagram for the VBF $H(\tau^+\tau^-) \to \ell^+\ell^- 4\nu$ process. The colours emphasise the independent colour flow for the tagging jets.

jets. As the decay products of the τ-leptons from the Higgs decay are boosted in the transverse plane and the tagging jets propagate in the forward-backward region of the detector, the pseudorapidity η of the leptons from the τ-decay are expected to be in-between the η of the tagging jets.

6.1.3. Colour Flow in VBF Events and Central Jet Veto

In Fig. 6.1, a key feature of the VBF production mode is stressed: As the tagging jets are produced independently by the two scattered quarks, the flow of the strong colour charge between the jets is suppressed. It follows, that additional jet contributions arising from QCD interactions are suppressed as well. In particular, only marginal jet activity in the central region of the detector is expected for a VBF signal event, as the tagging jets are located in the forward and backward region of the detector.

The presence of a third jet in a selected VBF event can indicate a background event, which fakes the VBF $H(\tau^+\tau^-) \to \ell^+\ell^- 4\nu$ topology. But it is also possible, that a gluon is radiated from the tagging jets in the signal event, i.e. due to ISR or FSR. As this radiation is typically collinear to the tagging jets, these soft emissions are expected to form jets, which are also located in the forward or backward region of the detector.
Furthermore, it is possible, that the scattered quarks undergo the so-called colour reconnection in the fragmentation process [106]. Imposing a well-separated propa-

gation in space-time, both quarks undergo a separated fragmentation process, where colour confinement happens independently. If, on the other hand, the scattering process of the incoming quarks is interpreted as a pointlike interaction, a "cross-talk" between the quarks leading to a reorganisation of the colour flow is comprehensible. This affects the event topology, as investigated in WW scattering events in [107]. The colour reconnection process can lead to multiple soft gluon emissions caused by the reorganised colour flow.

In order to improve the VBF selection, a veto on events with additional jets can be applied. Vetoing all events with more than two jets leads to a reduction of signal events, as the effects described above are not accounted for. This has to be avoided in order to maintain sufficient statistics. From the above considerations it becomes evident, that the veto has to be defined in a way, which allows for a discrimination between background and signal events with additional jets. Hence, the discriminator has to describe the centrality of additional jets in the events. Such a veto on central jets, is referred to as central jet veto (CJV) in the following.

In this thesis, the CJV definition is optimised by comparing several approaches in terms of significance for the selection, using simulated MC data sets.

6.2. Analysis Strategy

The aim of this thesis is to explore the VBF $H(\tau^+\tau^-) \to \ell\ell 4\nu$ channel and to optimise the cut-based selection. In the following, the analysis strategy to achieve this goal is discussed.

6.2.1. Studies in $Z/\gamma^* \to e^+e^-$ Control Region

The most important backgrounds for the VBF $H(\tau^+\tau^-) \to \ell\ell 4\nu$ signal are $Z/\gamma^* \to \ell^+\ell^-$ with $\ell = e, \mu, \tau$ - also referred to as *Drell-Yan* (DY) processes -, top and diboson processes. The MC samples used to model these processes are described in Sec. (5.3). It is known, that MC generators can mis-model processes and especially jet kinematics [73]. This can lead to deviations in the estimated number of background events and hence mis-leading cut-optimisations. Thus, a study in a control region with the aim of validating the MC simulation is conducted.

For the verification of the DY modelling, a Higgs-signal free $Z/\gamma^* \to e^+e^- + jets$ control region is defined. The validation is performed by examining the agreement

between MC and data for different observables.
By applying further selection criteria concerning a VBF topology, the simulation of VBF relevant variables is verified in the $Z/\gamma^* \to e^+e^-$ events. As a final study in this control region, an efficiency describing the veto performance for third jets in the selected events is calculated.
This control study provides insights into generator and normalisation performance as well as physics with 8 TeV data.

6.2.2. Optimisation of the Central Jet Veto

After checking the simulation performance in the control region, the main study is conducted.
Following [73], selection criteria for VBF $H(\tau^+\tau^-) \to \ell\ell 4\nu$ events are applied. Since a different kinematic region is studied, additional MC samples need to be implemented and validated. This is achieved, by successively investigating the data to MC ratio for all variables used for the selection.
An important characteristic of the topology of a VBF $H(\tau^+\tau^-) \to \ell\ell 4\nu$ event is a marginal jet activity in the central region. Therefore, a central jet veto (CJV) is applied in the selection. In order to discriminate between signal and background events while maintaining sufficient statistics, certain observables can be introduced to optimise the CJV. Several of these CJV-observables were studied in the analysis and compared in terms of significance for the selection.

6.2.3. The Framework

For the data analysis, a local `C++`-framework, capable of handling the state-of-the-art software tools provided by the ATLAS collaboration was set up. The framework was constructed to process data sets from Monte-Carlo simulations and data from the ATLAS experiment. The object-oriented library ROOT is used in the framework, as it provides an analysis-suitable data format [108, 109].
In order to process the data samples locally, the contained information had to be reduced to save storage capacity. This was done using the LHC computing grid, a computer network infrastructure designed to cope with the tremendous amount of data produced at the LHC [47]. The reduction was synchronised with the analysis needs, meaning that only necessary variables and loosely preselected events were taken into account.

The functionality of the framework was validated by comparing the numbers of events at successive cut stages within the working group.

6.3. Preselection

For each event, a set of preselection criteria is applied. As mentioned before, machine issues need to be treated as well as pile-up effects and trigger settings.

For all events, at least one primary vertex is required with a minimum of 3 associated tracks. This rejects non-collision backgrounds, e.g. contributions from cosmics, and suppresses pile-up events. If an event contains a jet, which is not associated to real energy deposits in the detector, it is rejected in the analysis.

Depending on the analysed final state, two oppositely charged leptons of certain flavour are required. For the ee final state, two electrons, for the $\mu\mu$ final state, two muons and for the $e\mu$ final state an electron and a muon are required according to the object selection criteria in Sec. (4). Furthermore, events with a hadronically decaying tau candidate, reconstructed as described in Sec. (4) are rejected, as only leptonic final states are considered.

The effects from pile-up events are taken into account by adding the contributions from additional proton-proton collisions, simulated with PYTHIA 8. For this, the bunch train structure and spacing of the beams was modelled, using information from *minimum bias events*. These are events, recorded with minimal requirements on the topology, hence providing minimal biased information. The MC samples are reweighted for each MC process separately in the analysis, according to the average number of interactions per bunch crossing per run in the data sample. Thus, the pile-up conditions of the corresponding data can be reproduced.

Trigger As described in Sec. (3.2.5), a trigger system is used to reduce the amount of data. For this analysis, trigger objects passing all trigger levels listed below are considered. The triggers are chosen according to the lepton flavours selected in the final state. The following trigger configuration is a compromise of high trigger efficiency and minimal number of triggers as studied in [73].

- ee-channel: The di-electron trigger `EF_2e12Tvh_loose1` and the single-electron trigger `EF_e24vhi_medium1` are used for this final state. The di-electron trigger requires two electron trigger objects with $p_t > 12$ GeV and loose selection

criteria (`loose1`). The tag `Tvh` symbolises criteria for the trigger object at the first trigger stage L1: an electromagnetic cluster threshold (`T`), a variable η threshold (`v`) and a hadronic leakage cut (h) [73]. The single electron trigger requires an electron trigger object with $p_t > 24$ GeV passing the `medium1` selection criteria [110]. At L1 an isolation criterion is applied (`i`). An event is accepted, if it passes any of the two triggers.
To account for trigger efficiencies, trigger scale factors are applied. For this, a trigger logic is implemented. If a reconstructed electron with $p_t > 25$ GeV is present in the event, the single-electron trigger is used. Otherwise, the di-electron trigger is required.

- $\mu\mu$-channel: Only events passing the di-muon trigger **`EF_mu18_tight_mu8_EFFS`** are considered for this final state. Both muon trigger objects are reconstructed in the MS and combined with an inner detector track. One of the objects has to exceed $p_t > 18$ GeV, while the other one is required to have $p_t > 8$ GeV. Furthermore, the leading muon trigger object has to fulfil the `tight` selection criteria.

- $e\mu$-channel: For this channel, the di-lepton trigger **`EF_e12Tvh_medium1_mu8`** and the single-electron trigger **`EF_e24vhi_medium1`** are used. The di-lepton trigger requires a muon trigger object reconstructed in the MS with a combined inner detector track and $p_t > 8$ GeV. Additionally, an electron trigger object fulfilling the `e12Tvh_medium1` criteria with $p_t > 12$ GeV is required. Any event, not passing this or the single electron trigger is rejected for the $e\mu$-channel.
  The logic for application of trigger scale factors is requiring a reconstructed electron with $p_t > 25$ GeV for the single electron trigger and the use of the di-lepton trigger otherwise.

For each trigger setup, a matching of the trigger objects with the offline reconstructed leptons in $\Delta\eta$, $\Delta\phi$ and p_t is performed.
The p_t thresholds of the two leptons in the final states for the analysis are chosen depending on their flavour and summarised, together with the trigger requirements in Tab. 6.2.

Detector Conditions For the data taking periods C1-C8 in 2012 a problem with the powering of the forward calorimeter (FCAL) occurred. The effect was studied in $Z/\gamma^* \to \mu\mu$ events. The issue caused a reduction in the cluster cell occupancy and changed the p_t spectrum of the reconstructed jets. Hence, a veto on jets with

Final state	Triggers	p_t thresholds
ee	`EF_2e12Tvh_loose1` `EF_e24vhi_medium1`	$p_t(e_1) > 15$ GeV $p_t(e_2) > 15$ GeV
$\mu\mu$	`EF_mu18_tight_mu8_EFFS`	$p_t(\mu_1) > 20$ GeV $p_t(\mu_2) > 10$ GeV
$e\mu$	`EF_e12Tvh_medium1_mu8` `EF_e24vhi_medium1`	$p_t(e) > 15$ GeV $p_t(\mu) > 10$ GeV

Table 6.2.: Summary of the required triggers and the p_t thresholds for the leptons in the final state used in the analysis for each channel.

$p_t > 20$ GeV in the region $|\eta| > 3.2$ and $1.6 < \phi < 3.1$ is applied for events in this period.
During the periods B1-B2 of data taking, a hot tile calorimeter cell caused problems in the reconstruction of jets. Again, a veto on jets pointing to this region is applied.

These treatments follow the recommendations of the JetEtMiss working group at ATLAS [111].

6.4. Systematic Uncertainties

For the analysis, systematic and statistic uncertainties are taken into account. Statistical uncertainties arise from the limited number of data and MC events. They increase with progressing cut stages, as less events are observed.
Systematic uncertainties arise from e.g. detector simulation, MC generator uncertainties, energy calibrations of the reconstructed objects, as well as cross sections and luminosity calculation. The evaluation of systematics, as presented in the following, is based on [73].

Lepton Scale and Resolution The quadratic sum of the systematic and statistical uncertainties arising from the determination of the lepton scale factors are taken as a systematic uncertainty. Additional uncertainties are introduced by the smearing of the simulated muons and electrons as described in Sec. (4). The relative uncertainty on VBF Higgs signal events, arising from these scale factors is of the order $\sim 0.5\%$ [73].

Jet Energy Scale and Resolution The calibration of the jet energy from the electromagnetic detector response to the hadronic scale introduces an important systematic uncertainty for this analysis. Since the following studies are dependent on the calibration of the involved jets, the jet energy scale (JES) uncertainty is considered the main source of systematic uncertainty. The JES uncertainty is derived by dedicated MC simulations and dependent on η and p_t of the jets. The main contributions to the JES uncertainty are the uncertainty of the JES calibration method, calorimeter response and the detector simulation, as well as the uncertainties of the parton shower and underlying event models employed in the dedicated MC simulation. Furthermore contributions from pile-up events, the η-dependent detector response calibration and the identification of close-by jets contribute [69]. The impact of the JES uncertainty in this analysis is determined by varying the jet energy "up" and "down" according to their $\pm 1\ \sigma$ uncertainties and is of the order of 5% for VBF Higgs signal events [73].

The difference between the reconstruction efficiency in data and MC for jets is calculated by a tag and probe method and negligible for jets with $p_t > 40$ GeV [73]. The scale and resolution uncertainties can be propagated to the reconstruction of $\not{E}_T$. Specific uncertainties like soft jet energy scale and resolution and clusterised energy deposits outside of jets are taken into account as well in [73]. The relative uncertainty for VBF Higgs signal events is $\sim 0.7\%$ [73].

Another jet-related uncertainty source are the b-tagging scale factors. Systematics arising from the b-tagging efficiency and mistag rates can be accounted for by shifting the scale factors by $\pm 1\ \sigma$.

Process Cross Sections, PDF and Luminosity The theoretical evaluation of the SM process cross section introduce systematic errors on the normalisation of the MC data samples. In the analysis presented in [73], all normalisation uncertainties are considered. For the VBF Higgs signal process, the relative uncertainty on the cross section ranges from 1%-10%. The uncertainties for the background samples, ranging from 0.5%-4%, can be found in [73, 112–114].

As recommended by the PDF4LHC working group, uncertainties due to the PDF sets are considered. These are applied for the normalisation of each MC samples and range from 3%-4% [114].

The measurement of the luminosity for the data set used in this study also introduces an uncertainty, determined by dedicated measurements [115, 116]. The

uncertainty of 3.6% is applied to the normalisation of each MC sample in [73].

The aim of the study presented in this thesis is a comparison between different observables, rather than a precision measurement. For that reason, only systematics affecting the shape of distribution are taken into account. Following the studies in [73], only the JES systematics has a non-negligible shape effect and is hence considered in the following.

6.5. Studies in a $Z/\gamma^* \to e^+e^-$ Control Region

As motivated in Sec. (6.2.1), the simulation performance of the Drell-Yan (DY) $Z/\gamma^* \to \ell^+\ell^- + jets$ process is studied in the following section. After applying selection criteria for $Z/\gamma^* \to e^+e^-$ events, further requirements, following the vector boson fusion (VBF) mode selection for the $H(\tau^+\tau^-) \to \ell^+\ell^- 4\nu$ process, are applied. This allows for a study of the background contribution of $Z/\gamma^* \to e^+e^- + jets$ events in the kinematic region of the VBF Higgs signal events. Finally, as an outlook for the central jet veto optimisation, the veto efficiency on third jets is investigated and the modelling validated.

For this study, MC signal contributions from QCD produced $Z/\gamma^* \to e^+e^-$ events, as well as background contributions from di-boson, $t\bar{t}$ and single-top processes are considered. Furthermore, VBF $Z/\gamma^* \to e^+e^-$ contributions are added. The corresponding MC samples and cross sections are depicted in Tab. 5.2.

6.5.1. $Z/\gamma^* \to e^+e^-$ Selection

After applying the preselection criteria depicted in Sec. (6.3), $Z/\gamma^* \to e^+e^-$ candidates are selected with the physics objects reconstructed according to Chapter (4). In the rest frame of the Z-boson, the electrons decay back-to-back. Therefore, a high transverse momentum p_t is expected for the two electrons. In Fig. AI.1, the p_t distributions of the two electrons with the largest transverse momentum in the event, referred to as *leading* and *sub-leading* electrons, are depicted.
For the selection, two oppositely charged electrons are required, each exceeding $p_t > 20$ GeV. Background events from multi-jet processes with falsely identified electrons are suppressed by this p_t threshold and the isolation and quality criteria described in Chapter (4).

The invariant mass spectrum, calculated from the four-vectors of the electrons, is depicted in Fig. 6.2.
The upper part shows the number of entries per mass bin. The MC contributions are normalised to the integrated luminosity of 13.06 fb^{-1} of the data and stacked. The uncertainty arising from the jet energy calibration is depicted as hatched box around the nominal MC predictions per bin, but negligible for the mass spectrum. The markers in the lower part of the plot show the ratio between data and MC event yields for each bin. The yellow band is the combination of statistical and systematic

uncertainty and centred around the red line at 1. The same plot structure is used for displaying distributions in the following figures. The structure observed around the

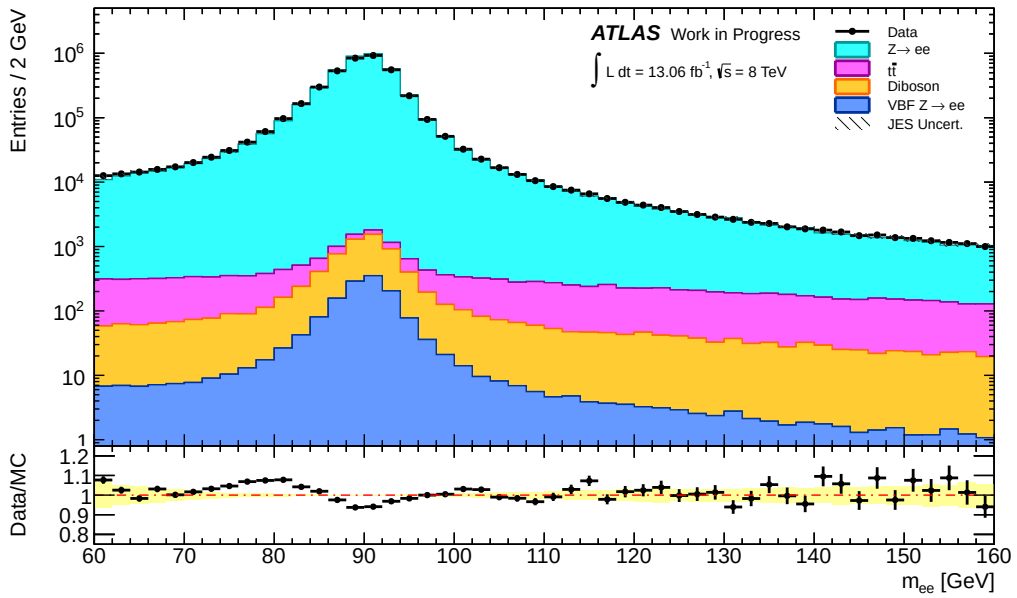

Figure 6.2.: Invariant mass spectrum for the selected electrons with $p_t > 20$ GeV in the $Z/\gamma^* \to e^+e^-$ control region. The yellow band is the combination of statistical and systematic uncertainty.

Z-pole at ~ 91 GeV can be attributed to known problems of the detector simulation [73]. Besides this structure, the modelling of the mass spectrum is consistent with data within the statistical uncertainty.
The invariant mass is required to cover the Z-peak by choosing a mass window of

$$70 \text{ GeV} < m_{ee} < 110 \text{ GeV} \quad .$$

The event yields for the selection are shown for all samples and the sum of MC events in Tab. AII.1, together with systematic and statistical uncertainties. The dominant background contribution are the DY processes. Over the whole spectrum a slight overestimation of $\sim 3\%$ is observed, as can be calculated from the sum of all MC events and the data event yields in Tab. AII.1.

6.5.2. VBF $Z/\gamma^* \to e^+e^-$ Selection

After the selection of $Z/\gamma^* \to e^+e^-$ events, selection criteria for the vector boson fusion production mode are applied. As explained in Sec. (6.1), two jets with high p_t are expected to form from the incoming scattered quarks in a VBF $H(\tau^+\tau^-) \to \ell^+\ell^- 4\nu$ event.

In Fig. 6.3 (left) the p_t distribution for the leading jet in the selected $Z/\gamma^* \to e^+e^-$

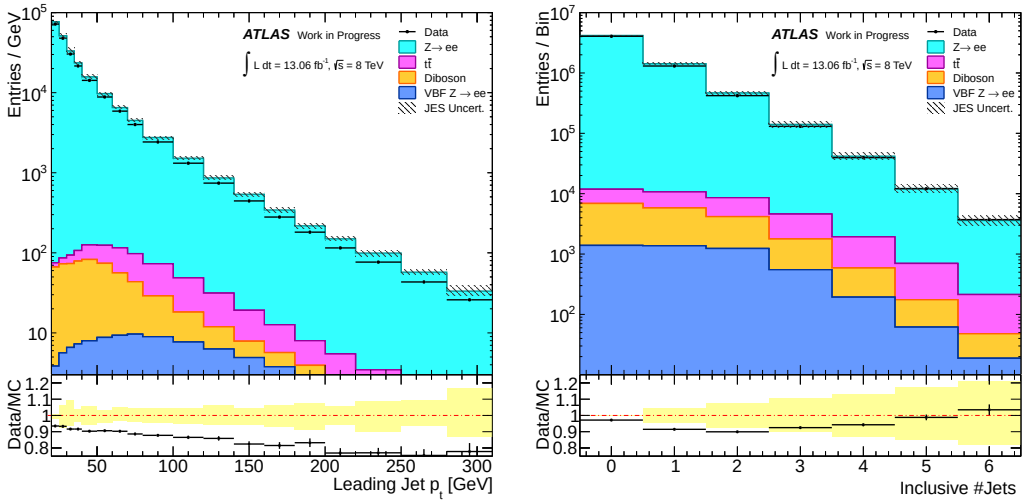

Figure 6.3.: The p_t distribution for the leading jet (left) and the inclusive jet multiplicity for jets with $p_t > 20$ GeV (left) for the selected $Z/\gamma^* \to e^+e^-$ events. The striped box depicts the uncertainty on the MC event yields per bin due to the jet energy scale calibration.

events is presented. An overestimation over the whole spectrum of up to 25% for jets with $p_t > 200$ GeV is observed. This indicates, that jet kinematic is modelled incorrectly with ALPGEN, i.e. the jet p_t overestimated. For the selection, a leading jet $j1$ with $p_t(j1) > 40$ GeV is required. The inclusive jet multiplicity of the $Z/\gamma^* \to e^+e^-$ events is shown in Fig. 6.3 (right). For jet multiplicities ≤ 5 the number of jets is overestimated between $\sim 5-12\%$. For jet multiplicities ≥ 3, the deviation is covered by the systematic uncertainty, which are between $\sim 5-15\%$ and increasing with higher multiplicities. As explained in Sec. (5.3), the $Z/\gamma^* \to e^+e^- + jets$ process is modelled with hard matrix element calculations with jet multiplicity of ≤ 5. Hence higher jet multiplicities arise from the parton showering. The slope in the distribution for multiplicities ≥ 3 indicates, that the parton showering overestimates the number of jets.

The overestimation of the jet kinematics modelling in ALPGEN is also visible in the η and ϕ distributions of the selected leading jets, shown in Fig. AI.2.

The p_t-spectrum of the sub-leading jet after the requirement on the p_t of the leading jet is presented in Fig. 6.4 (left) together with the inclusive jet multiplicity. Again, an overestimation, particularly for jets with high p_t is observed. The sub-leading jet $j2$ has to fulfil $p_t(j2) > 25$ GeV for the selection. The η and ϕ distributions of the these sub-leading jets is shown in Fig. AI.2 and suffer from the same mis-modelling effects.

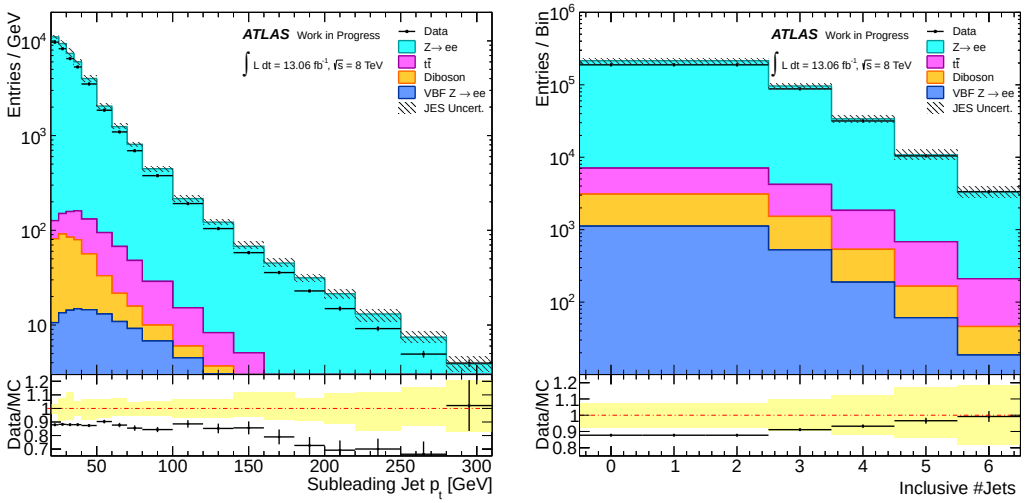

Figure 6.4.: The p_t distribution for sub-leading jet (left) and the inclusive jet multiplicity (right) after the leading jet requirement in the $Z/\gamma^* \to e^+e^-$ control region.

Pseudorapidity Difference As explained in Sec. (6.1), the tagging jets are expected to be well separated in η. This separation can be quantified by the pseudorapidity difference

$$\Delta\eta = |\eta_{j1} - \eta_{j2}| \tag{6.1}$$

and is expected to be large for VBF events. For the selected events after the sub-leading jet requirement, the pseudorapidity difference is shown in Fig. 6.5. In Fig. AI.2, the pseudorapidities for the selected leading jets is shown. The overestimation for small η is propagated to the pseudorapidity difference. For small differences $\Delta\eta < 3$, the MC deviates between $10 - 20\%$ percent from the data.

Larger differences are in better agreement and lie within the systematics. For very large $\Delta\eta > 5$ the systematic uncertainty is up to 20% and the statistical uncertainty between $5 - 10\%$. For the selection, a cut of $\Delta\eta > 3.0$ is chosen, thereby selecting a kinematic region with satisfying agreement and following the selection for a VBF Higgs signal event.

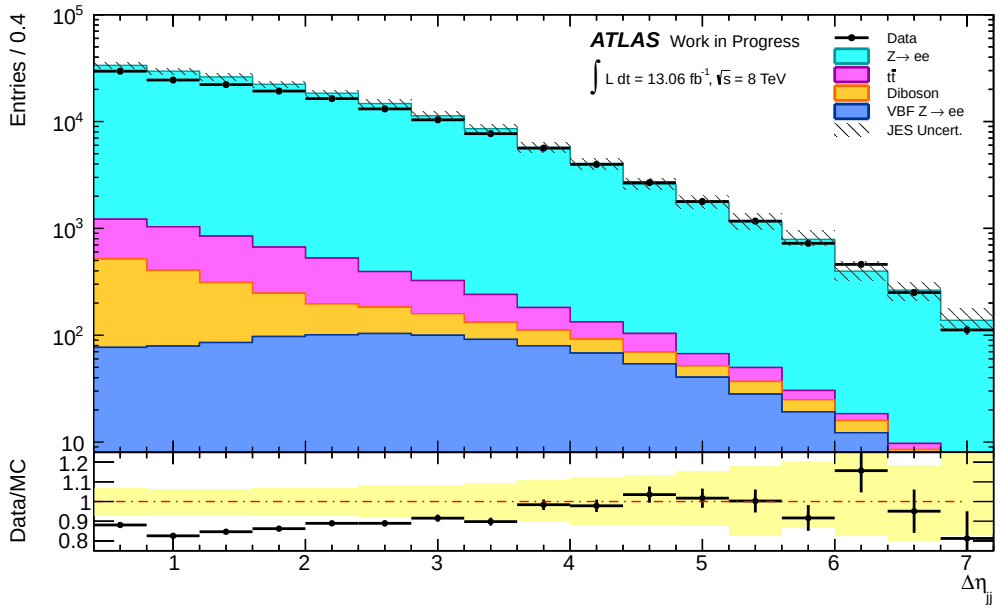

Figure 6.5.: The pseudorapidity difference $\Delta\eta$ between the two leading jets is shown for the $Z/\gamma^* \to e^+e^-$ control region.

Di-jet mass The invariant mass of the two jets is described by the *di-jet mass*, calculated from the jets' four momenta p^μ via

$$m(j1, j2) = \sqrt{p^\mu_{j1} p_{\mu,j_2}} \quad .$$

This di-jet mass is expected to be large for VBF-produced events, as motivated in Sec. (6.1). The distribution is shown for the events after the pseudorapidity difference cut in Fig. 6.6. The MC simulation and data yields are in good agreement within the uncertainties. The selected kinematic region is hence described well by the simulation. The systematic uncertainty is $\sim 10\%$ and the statistical uncertainty ranges between $5 - 15\%$. For the VBF Higgs signal selection in the following chapter, DY and $t\bar{t}$ processes are suppressed by requiring a minimum mass of $m(j1, j2) > 400$ GeV. The same cut is applied for this selection, in order to validate

the simulation of the resulting kinematic region.

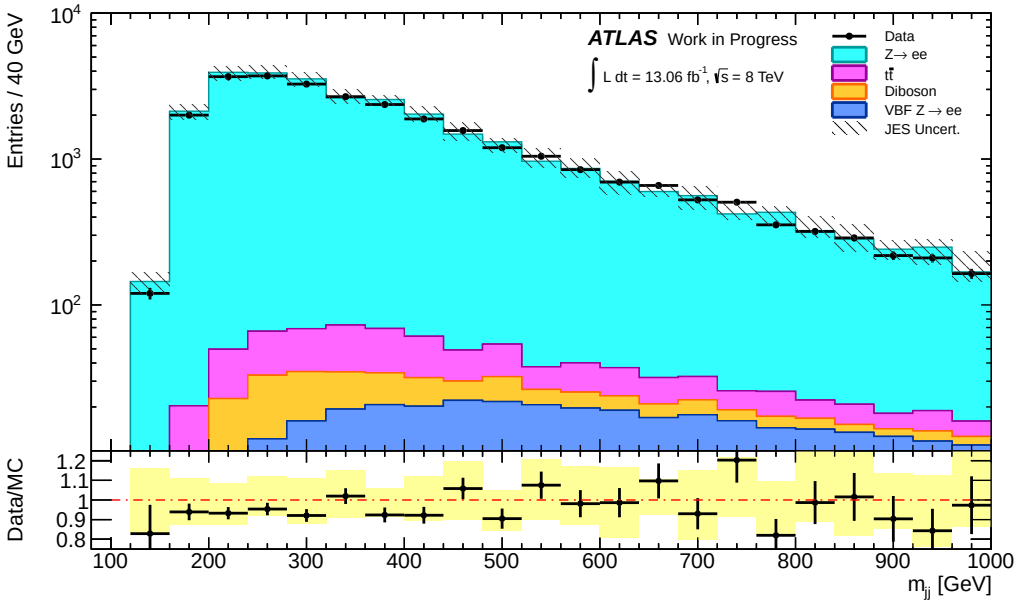

Figure 6.6.: Invariant mass distribution m_{jj} between the two leading jets after the $\Delta\eta_{jj}$ requirement.

The event yields for the $Z/\gamma^* \to e^+e^-$ events in the VBF selection are presented in Tab. AII.2. Furthermore, the inclusive number of jets for the remaining events is presented in Fig. 6.7. Data and MC are in a good agreement for the selected region. The systematic uncertainties range from $10 - 20\%$.

6.5.3. Veto-Efficiency

As explained in Sec. (6.1), no flow of colour charge occurs between the two quarks in a leading order VBF process. Events with additional jets originate from background processes or higher-order QCD signal events, i.e. from ISR/FSR.
The p_t and η distributions for the third leading jet in the selected events is shown in Fig. 6.8. All fluctuations are covered by the uncertainties. Third jets with high transverse momentum are rare, thus large uncertainties of $\sim 40\%$ are present for $p_t(j3) > 100$ GeV. Third leading jets in the VBF $Z/\gamma^* \to ee$ contribution are enriched at $|\eta| \approx 3$. This meets the expectations for a VBF-produced event, since additional jets in a VBF event are expected to be collinear to the tagging jets, as discussed in Sec. (6.1).

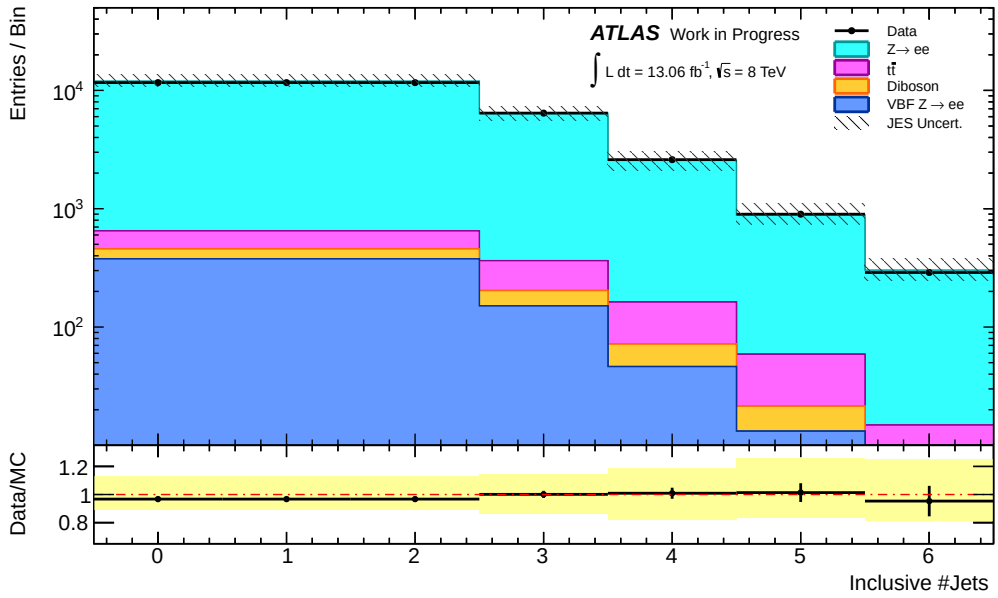

Figure 6.7.: Inclusive number of jets for the $Z/\gamma^* \to ee$ events in the VBF selection.

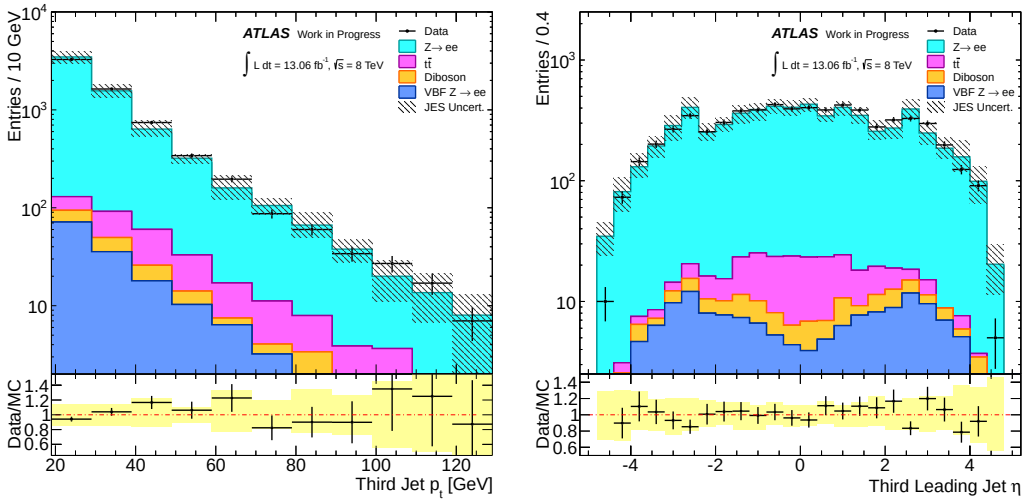

Figure 6.8.: The p_t (left) and η (right) distributions for the third leading jets in the VBF-selected $Z/\gamma^* \to e^+e^-$ events.

In order to improve the VBF selection, a simple veto on events with a third jet is defined as

⋆ reject all events containing a third jet with a p_t above a certain threshold.

In order to study the impact on the number of remaining events from such a veto, the p_t-threshold x is varied between 20 GeV $< p_t <$ 100 GeV. For each threshold, a survival efficiency defined as

$$\varepsilon_{\mathrm{x}} = 1 - \frac{\text{Number of events with } p_t(j3) > x \text{ GeV}}{\text{Total Number of Events after VBF Selection}} \tag{6.2}$$

is calculated, taking into account the total number of events in the VBF selection and the number of surviving events after applying the veto. Since the number of surviving events and the total number of events are correlated, the binominal uncertainty $\sigma_{\varepsilon_{\mathrm{x}}}$, defined as

$$\sigma^2_{\varepsilon_{\mathrm{x}}} = \frac{\varepsilon_x \left(1 - \varepsilon_x\right)}{\text{Total Number of VBF events}} \quad , \tag{6.3}$$

is used as statistical uncertainty for the efficiencies. Furthermore, systematic uncertainties arising from the JES calibration are considered. The resulting efficiencies are presented in Fig. 6.9 and listed in Tab. 6.3. For low p_t thresholds, an efficiency

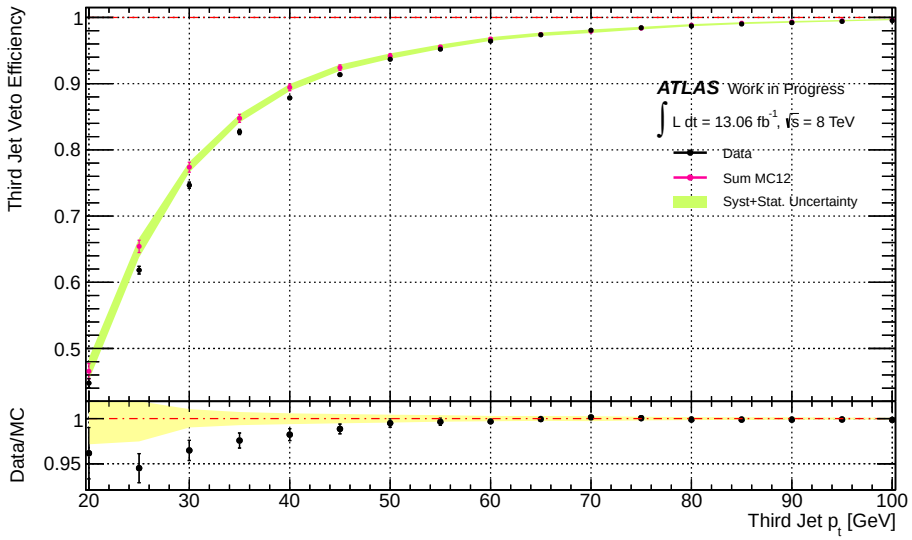

Figure 6.9.: The survival efficiency for the p_t dependent veto on third jets. The green error band is the combination of statistical and systematic uncertainty.

$\gtrsim 0.5$ is observed. This means, that most additional jets in the DY processes have a low transverse momentum, as can be verified with Fig. 6.8. For higher thresholds, the efficiency converges to 1 as only a small number of third jets carry high p_t. Since all jets are required to exceed $p_t > 20$ GeV at the preselection stage, the efficiency

for a 20 GeV threshold corresponds to strictly choosing only events with two jets. For low p_t thresholds < 45 GeV a small deviation of $\sim 5\%$ between data and simulation is observed.

Threshold		Efficiency	Syst. Uncertainty	Stat. Uncertainty
$p_t(j3) > 20$ GeV	MC	0.466	$+0.016$ -0.006	± 0.012
	Data	0.448	-	± 0.007
$p_t(j3) > 30$ GeV	MC	0.774	$+0.003$ -0.001	± 0.007
	Data	0.747	-	± 0.005
$p_t(j3) > 40$ GeV	MC	0.8943	$+0.000$ -0.002	± 0.005
	Data	0.878	-	± 0.003
$p_t(j3) > 80$ GeV	MC	0.988	$+0.000$ -0.000	± 0.002
	Data	0.987	-	± 0.001

Table 6.3.: Veto efficiencies on third jets for selected thresholds.

As this simple veto does not account for the higher-order effects for VBF events explained in Sec. (6.1), an improvement is achieved, by requiring the third leading jet to lie inbetween the two leading jets, i.e.

$$\min(\eta_{j1}, \eta_{j2}) < \eta_{j3} < \max(\eta_{j1}, \eta_{j2}) \quad .$$

In Fig. 6.10, the same efficiency was calculated with this additional constraint on the third leading jet. The p_t and η distributions for third jets fulfilling this requirement is shown in Fig. AI.3. The additional requirement increases the efficiency by $\sim 5\%$ for low-p_t thresholds. Hence, more DY background in the Higgs selection is expected with the additional centrality constraint. The same converging behaviour as before is observed. Furthermore, the deviation between MC and data for low thresholds is smaller with $\sim 3\%$ than in Fig. 6.9. As a comparison with Tab. 6.3, selected efficiencies are listed in Tab. 6.4.

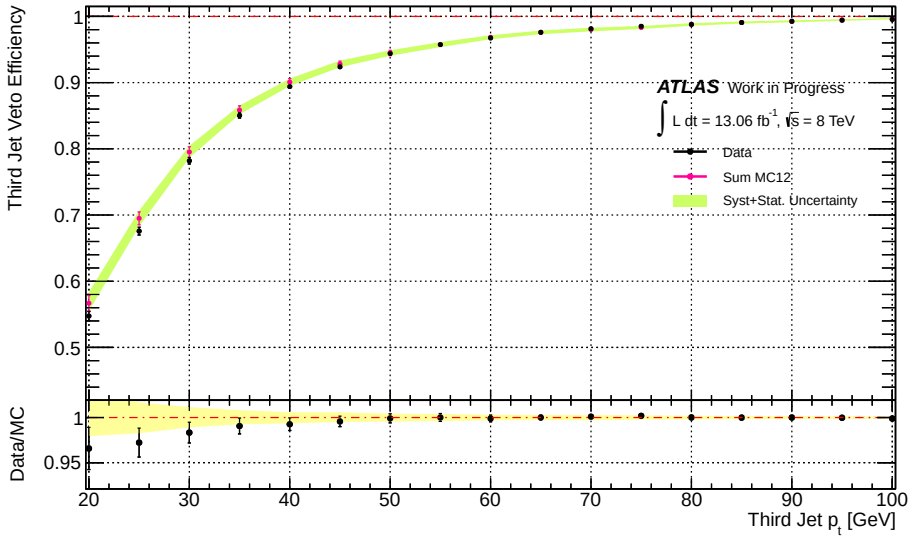

Figure 6.10.: The survival efficiency for the p_t dependent veto on third jets between the two leading jets is shown.

Threshold		Efficiency	Syst. error	Stat. Error
$p_t(j3) > 20$ GeV	MC	0.567	$^{+0.012}_{-0.001}$	± 0.012
	Data	0.547	-	± 0.007
$p_t(j3) > 30$ GeV	MC	0.795	$^{+0.005}_{-0.004}$	± 0.008
	Data	0.782	-	± 0.005
$p_t(j3) > 40$ GeV	MC	0.901	$^{+0.000}_{-0.002}$	± 0.005
	Data	0.894	-	± 0.003
$p_t(j3) > 80$ GeV	MC	0.988	$^{+0.000}_{-0.001}$	± 0.002
	Data	0.988	-	± 0.001

Table 6.4.: Veto efficiencies on third jets lying in-between the two leading jets for selected thresholds.

Synopsis In this section, a validation of the MC simulation of Drell-Yan processes $Z/\gamma^* \to \ell^+\ell^- + jets$ was performed, by studying events in a $Z/\gamma^* \to e^+e^-$ control region and investigating the data-to-MC ratio. At early cut stages the MC predictions for the jet kinematics overestimates the data up to $\sim 20\%$. In the kinematic region studied for the VBF Higgs selection in the following sections, a satisfying agreement between data and Monte Carlo within the uncertainties is observed. In particular VBF relevant variables are modelled correctly.

6.6. Studies for VBF $H(\tau^+\tau^-) \to \ell^+\ell^- 4\nu$ Searches

In this section, a summary of the main study conducted for the search of the Standard Model Higgs boson in the vector boson fusion (VBF) produced $H(\tau^+\tau^-) \to \ell^+\ell^- 4\nu$ channel is given.

Following [73], selection criteria for $H(\tau^+\tau^-) \to \ell\ell 4\nu$ events are applied, including all the production modes presented in Sec. (2.2.2). Thereafter, requirements on VBF specific variables are applied in order to select the VBF production mode. The selection is based on studies in [73, 104, 117]. After the discussion of the selection criteria, the optimisation study for the central jet veto (CJV) is presented, as motivated in Sec. (6.1).

For the study, the VBF $H(\tau^+\tau^-) \to \ell^+\ell^- 4\nu$ signal sample for a Higgs mass of $m_H = 125$ GeV is used. In all following plots, the signal contribution is scaled by a factor of 10 for better visibility. MC background contributions arising from diboson, $t\bar{t}$ and single-top processes are considered. Furthermore, Drell-Yan processes $Z \to \ell\ell$, VBF $Z \to \ell\ell$ and $W \to \ell\nu$ with $\ell = e, \mu, \tau$ are taken into account. Background arising from false identification of jets as leptons (*fake leptons*) is partly modelled by adding samples of heavy flavour jet production accompanied with the latter processes, i.e. $Z \to \ell\ell + bb$ and $W \to \ell\nu + bb/cc/c$. Further background from multi-jet processes is rejected by dedicated selection criteria, as will be discussed in the following.
Physics objects - electrons, muons or jets - with the highest p_t in the events are referred to as *leading* objects in the following. The following plots are constructed as described in Sec. (6.5.1). On top of the plots, it is indicated for which channel the distributions are presented.

In Tab. 6.5, all criteria which will be applied for the VBF $H(\tau^+\tau^-) \to \ell^+\ell^- 4\nu$ signal selection are summarised. The cut variables and chosen thresholds will be motivated in the following sections.

$e^+e^- + \mu^+\mu^-$	$e\mu$
$H(\tau^+\tau^-) \to \ell^+\ell^- 4\nu$ selection	
Preselection according to Sec. (6.3)	
30 GeV $< m_{ee+\mu\mu} <$ 75 GeV	30 GeV $< m_{e\mu} <$ 100 GeV
$p_t(\ell\ell) > 35$ GeV	$p_t(\ell\ell) > 45$ GeV
At least one jet with $p_t > 40$ GeV	
$\not{E}_T > 40$ GeV and $\not{E}_T^{\mathrm{HPTO}} > 40$ GeV	$\not{E}_T > 20$ GeV
Visible momentum fractions $0.1 < x_{1/2} < 1.0$	
$0.5 < \Delta\phi(\ell\ell) < 2.5$	
VBF $H(\tau^+\tau^-) \to \ell^+\ell^- 4\nu$ selection	
$H(\tau^+\tau^-) \to \ell^+\ell^- 4\nu$ selection requirements	
At least a second jet with $p_t > 25$ GeV	
Pseudorapidity difference $\Delta\eta_{jj} > 3.0$	
$m_{jj} > 400$ GeV	
b-tag veto	
Central Jet Veto	
Lepton centrality requirement	

Table 6.5.: Summary of the criteria for the selection of VBF $H(\tau^+\tau^-) \to \ell^+\ell^- 4\nu$ signal events.

6.6.1. $H(\tau^+\tau^-) \to \ell^+\ell^- 4\nu$ Selection

All considered events in this study are preselected according to the criteria presented in Sec. (6.3). The physics objects are reconstructed as described in Sec. (4). If a hadronically decaying τ candidate is present, the event is rejected.

For all events, two oppositely charged leptons are required. The lepton flavours in the final states of the $H(\tau^+\tau^-) \to \ell^+\ell^- 4\nu$ process form three categories: the ee, $\mu\mu$ and $e\mu$ channel. The transverse momentum p_t thresholds of the two leptons are chosen depending on their flavour and summarised in Tab. 6.2. The p_t thresholds for electrons is 15 GeV, chosen to suppress fake lepton background from multi-jet events.

The muon threshold is 10 GeV except for the leading muon in the $\mu\mu$ channel, which has to exceed $p_t > 20$ GeV, chosen to suppress background events [73].

The p_t distributions for all leptons are presented in Fig. BI.1-BI.2. In order to increase statistics, the ee- and the $\mu\mu$-channels are combined in the following, as the background contributions arise from similar processes.

In Fig. 6.11, the invariant mass spectrum for the combined $ee + \mu\mu$ channel is shown. The dominating contributions are $Z/\gamma^* \to ee/\mu\mu$ (DY) events followed by top-quark processes. The invariant mass of leptons from $Z/\gamma^* \to \tau\tau$ is shifted away from the Z-peak towards lower values, as the energy of the undetected neutrinos does not contribute to the spectrum. $W \to \ell\nu$ processes give rise to background contributions along the whole mass spectrum. The mass of the leptons from the signal process is mainly between 20 GeV $< m_{\ell\ell} <$ 100 GeV. Overall, data and MC simulation show a good agreement with only small deviations. The detector simulation effect also seen in Sec. (6.5.1) is again visible around the Z-peak.

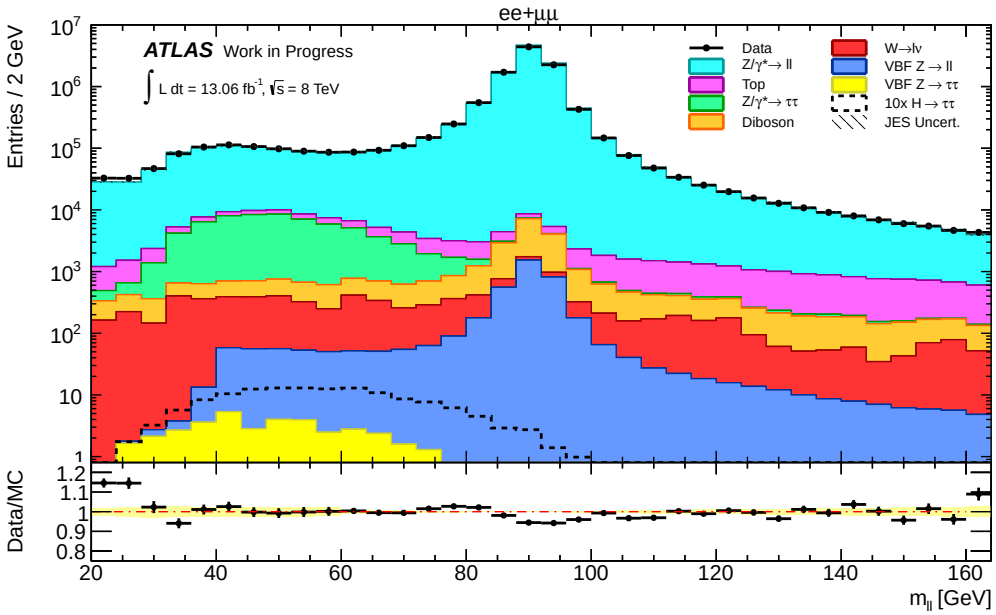

Figure 6.11.: Invariant mass spectrum of the selected leptons in the combined $ee+\mu\mu$ channel. The MC contributions are normalised to the integrated luminosity of the data set. The dotted line depicts the Higgs signal with a simulated Higgs mass of $m_H = 125$ GeV. The yellow band is calculated by combining statistical and systematic uncertainty.

The invariant spectrum for the $e\mu$ channel is shown in Fig. BI.3. The main

background contributions are caused by $t\bar{t}$ and single top processes, followed by $Z/\gamma^* \to \tau\tau$ events. Because of the different flavours of the leptons in the final state, the $Z/\gamma^* \to ee/\mu\mu$ process is suppressed. The deviation of the MC contributions from data, especially for low invariant mass values is caused by fake leptons from multi-jet background, as can be seen in the mass spectrum in Fig. BI.4 and will be removed in the following by dedicated cuts [73].
As the background contributions differ for the combined and for the $e\mu$ channel, different mass windows are selected. In the combined channel, a tighter requirement needs to be applied in order to suppress the DY contributions. The mass windows are defined as

$$\begin{aligned} 30 \text{ GeV} < \ & m_{ee+\mu\mu} < 75 \text{ GeV} \\ 30 \text{ GeV} < \ & m_{e\mu} \quad\ < 100 \text{ GeV} \quad . \end{aligned}$$

The event yields after this requirement are presented in Tab. BII.1. Overall, 11.6 VBF Higgs signal events and 110200 background events are expected in the combined channel, while 13.7 signal events and 88100 background events are modelled for the $e\mu$ channel,

In order to reject the multi-jet background, a cut on the transverse momenta of the di-lepton system, calculated from the four-vector of each lepton, is applied.

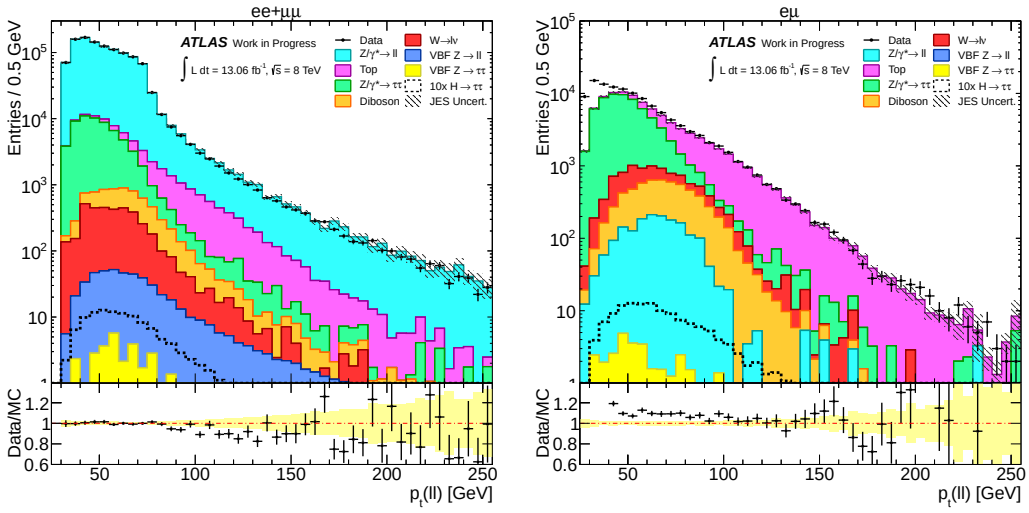

Figure 6.12.: The $p_t(\ell\ell)$ spectrum of the di-lepton systems after the mass window cut. The hatched box depicts the uncertainty on the MC event yields per bin due to the jet energy scale calibration.

The spectra for both channels are shown in Fig. 6.12. For the combined $ee + \mu\mu$ channel, a threshold of $p_t(\ell\ell) > 35$ GeV is chosen. As more multi-jet contributions for the $e\mu$ channel are observed and enriched in a low-p_t region, a higher threshold of $p_t(e\mu) > 45$ GeV is applied. This rejects the majority of the multi-jet background [73].

In Fig. 6.13, the p_t spectrum for the leading jet in the selected events is shown. In order to suppress Drell-Yan (DY), di-boson and $W \to \ell\nu$ backgrounds, a leading jet with $p_t > 40$ GeV is required for the selection. The inclusive number of jets with $p_t > 40$ GeV and the η and ϕ distributions for the selected leading jet is presented in Fig. BI.5. The contributions of the top backgrounds are only marginally affected by this cut.

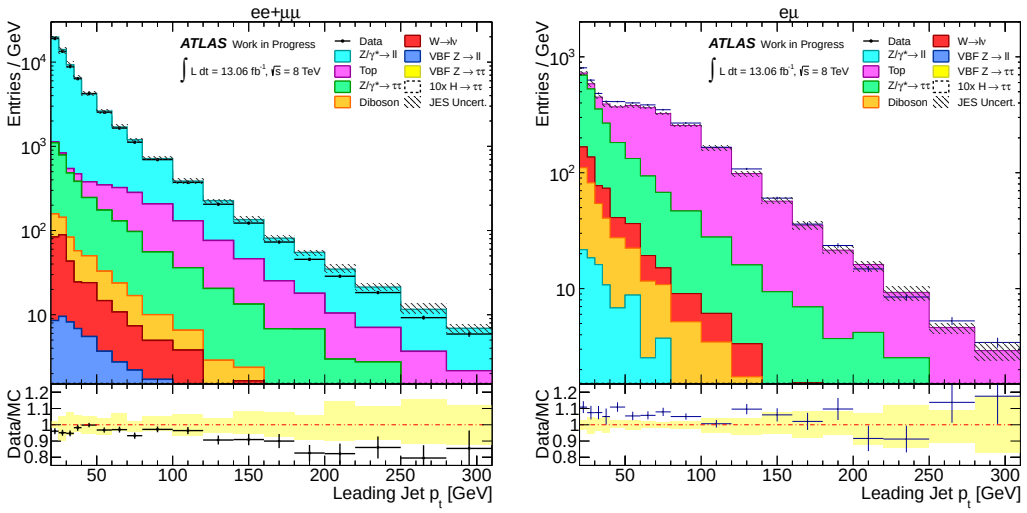

Figure 6.13.: The p_t spectrum of the leading jet in the selected events after the di-lepton p_t requirement.

As motivated in Sec. (6.1), the presence of a high-p_t jet in the selection leads to a boost of the Higgs' decay products in the transverse plane. As a consequence, the missing transverse energy $\not{E}_T$ of the signal events is expected to be large. The distribution of $\not{E}_T$ can be seen in Fig. 6.14. The cut $\not{E}_T > 40$ GeV for the combined channel is chosen to be tighter than cut for the $e\mu$ channel with $\not{E}_T > 20$ GeV in order to reject DY background efficiently.
As shown in [73], an additional cut on the high-p_t object missing transverse energy $\not{E}_T^{\mathrm{HPTO}}$, defined in Equ. 4.1, is expected to improve the suppression of DY backgrounds. The distribution of $\not{E}_T^{\mathrm{HPTO}}$ is shown in Fig. 6.15. The kink observed at

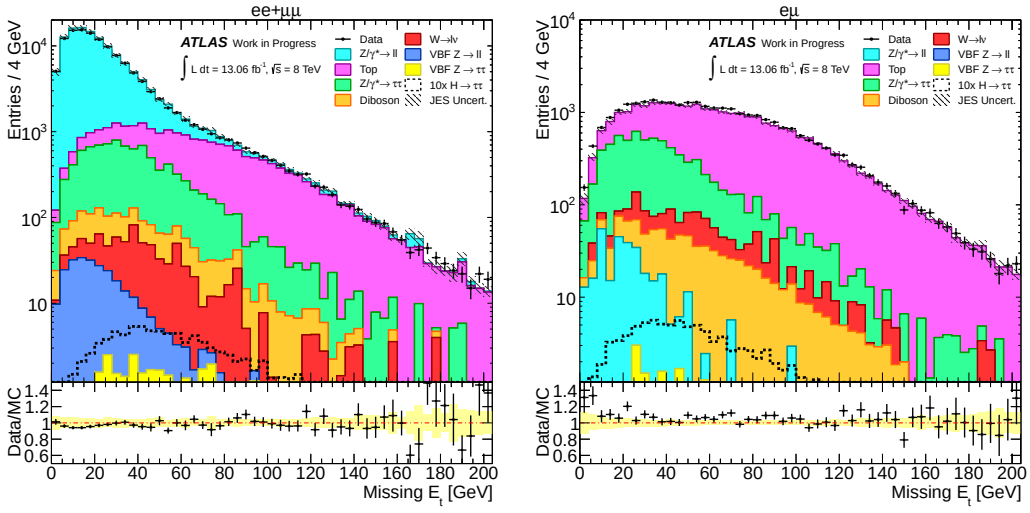

Figure 6.14.: Distributions of $\not{E}_T$ for events after the $p_t > 40$ GeV requirement for the leading jet.

40 GeV in the distributions is caused by the contribution of the leading jet to the calculation of $\not{E}_T^{\text{HPTO}}$. By requiring $\not{E}_T^{\text{HPTO}} > 40$ GeV DY background as well as top backgrounds are suppressed, while maintaining the majority of the signal events.

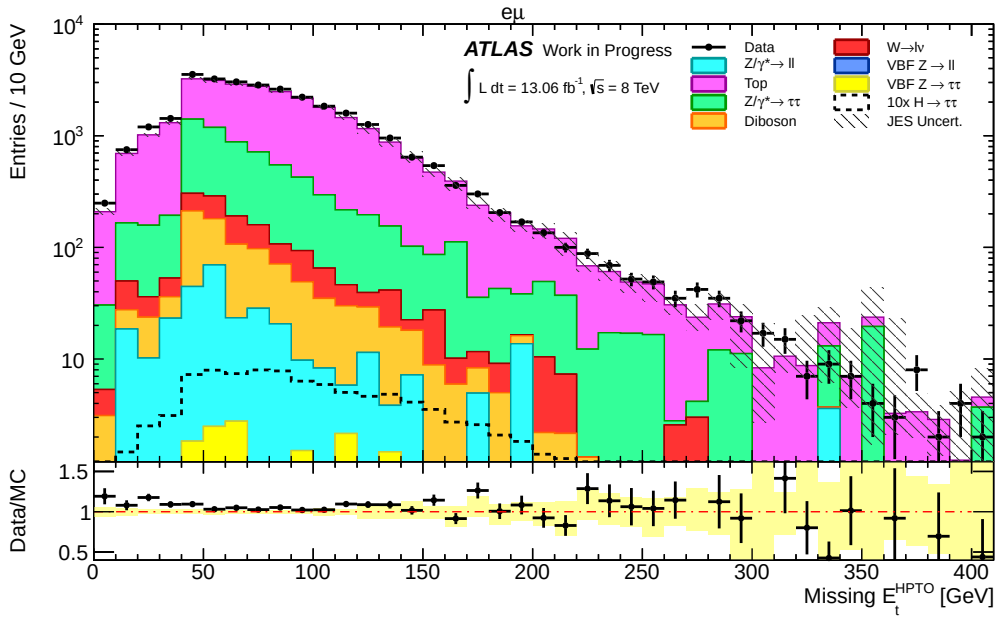

Figure 6.15.: Spectrum of the $\not{E}_T^{\text{HPTO}}$ for the $e\mu$-channel after the $\not{E}_T$ cut.

Visible Momentum Fraction Because of the boost of the τ-leptons produced by the Higgs boson, their decay products are also boosted. In the collinear approximation, discussed more detailed in Sec. (6.6.3), it is assumed that the decay products of the τ are produced collinearly. This means, that the neutrinos are aligned with the visible leptons from the τ decay [118].
Background events, not originating from τ leptons can be suppressed by a requirement on the visible momentum fractions $x_{1/2}$. They describe the detected fraction of the τ momentum, i.e. x_1 the fraction for the τ-parent of the leading lepton and x_2 for the sub-leading lepton. They can be calculated as

$$x_{1/2} = \frac{p_{1/2}^{\text{vis}}}{p_{1/2}^{\text{vis}} + p_{1/2}^{\text{miss}}} \tag{6.4}$$

where $p_{1/2}^{\text{vis}}$ denote the leptons' momenta and $p_{1/2}^{\text{miss}}$ the momenta associated with the neutrinos. The exact definitions are given in Sec. (6.6.3). The fractions, depicted in Fig. 6.16, are required to be $0.1 < x_{1/2} < 1.0$, thereby suppressing $t\bar{t}$ and DY backgrounds in both channels.

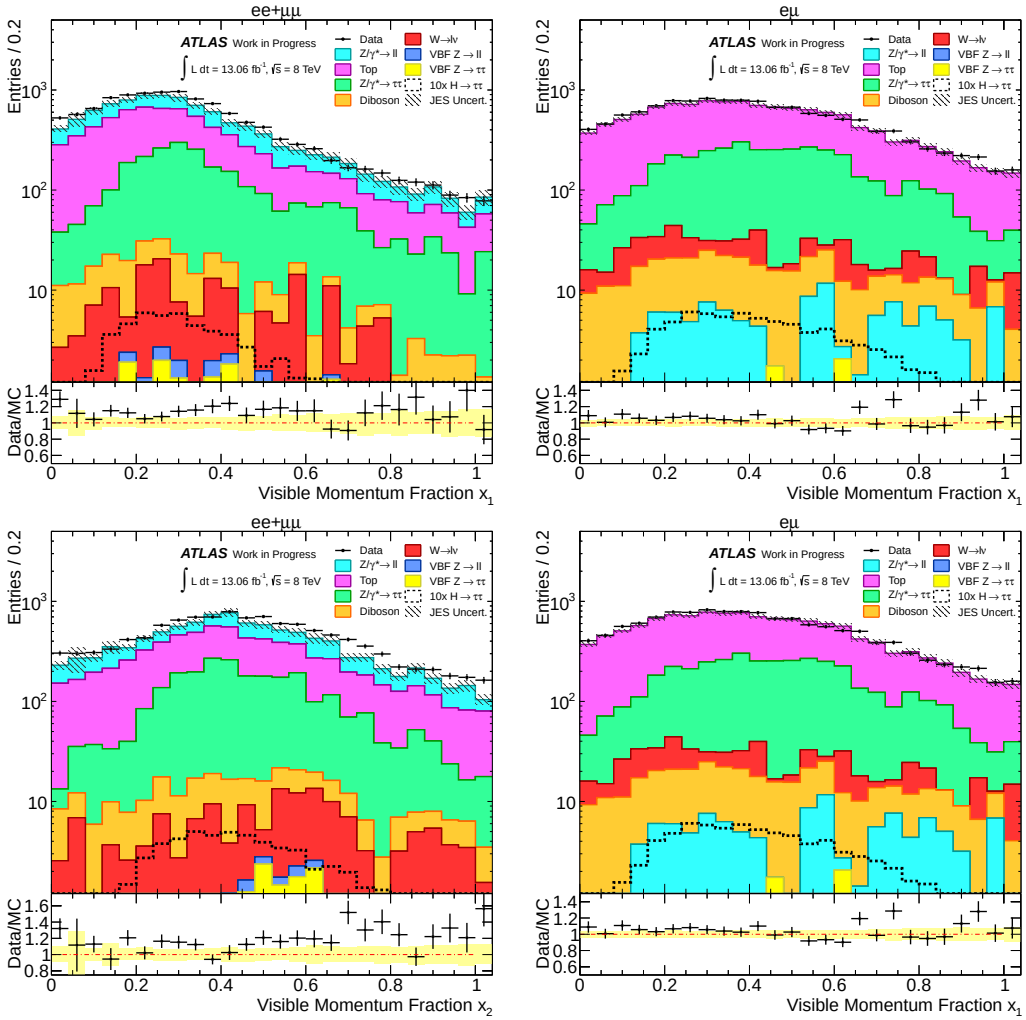

Figure 6.16.: Visible momentum fractions x_1 (top) and x_2 (bottom) after the $\not{E}_T$ (combined) and $\not{E}_T^{\mathrm{HPTO}}$ (emu) requirements.

Finally, a requirement on the difference in ϕ between the two leptons in the final state is applied. In Fig. 6.17, the distribution of $\Delta\phi_{\ell\ell} = |\phi(\ell 1) - \phi(\ell 2)|$ is shown. As the two τ-leptons from the Higgs decay are boosted, their decay products are as well. Hence the leptons are not back-to-back in the transverse plane of the laboratory frame. By choosing a cut window of $0.5 < \Delta\phi(\ell\ell) < 2.5$ large amounts of DY background events are suppressed. Furthermore, events with leptons originating from top events are rejected.

The event yields after these selection steps are shown in Tab. BII.2. For the com-

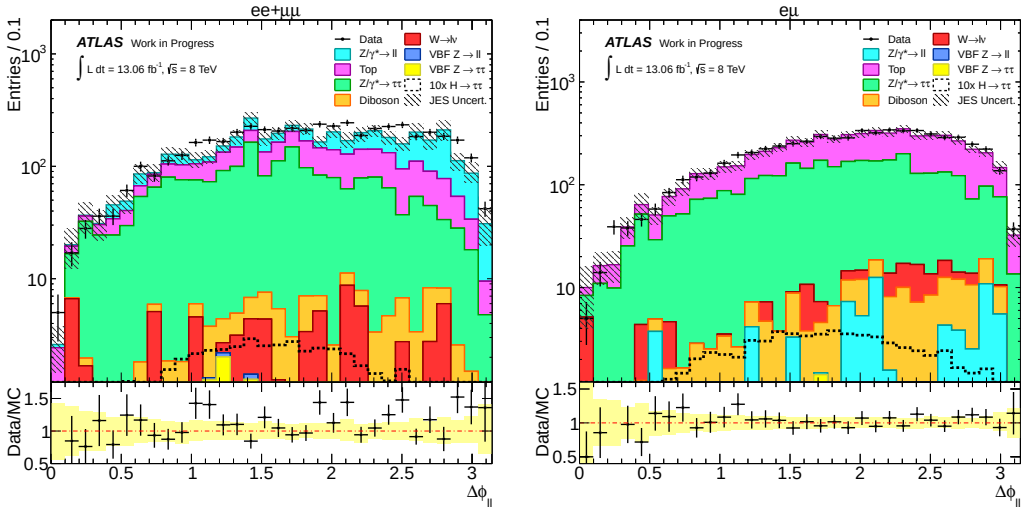

Figure 6.17.: Distribution of the angular difference $\Delta\phi_{\ell\ell}$ after the visible momentum fraction cuts.

bined channel, 48% of the background events after the $\Delta\phi_{\ell\ell}$ requirement originate from $Z \to \tau\tau$, 28% from top and 21% from $Z \to \ell\ell$ processes. For the $e\mu$ channel, $Z \to \tau\tau$ events give rise to 51% of the background events, while 46% originate from top processes. Compared to the event yields after the mass window cut, the signal events in the combined channel are reduced by 64% and the background events by 99.6%. 99.7% of the data events are vetoed. For the $e\mu$ channel, the applied cuts yield a reduction of 59% signal, 95% background events and 97% of data.

6.6.2. VBF $H(\tau^+\tau^-) \to \ell^+\ell^- 4\nu$ Selection

After the selection of $H(\tau^+\tau^-) \to \ell^+\ell^- 4\nu$ events produced in any of the modes introduced in Sec. (2.2.2), selection criteria concerning the vector boson fusion production (VBF) mode are applied. The full process is described in detail in Sec. (6.1). The jets originating from the quark scattering are referred to as *tagging* jets in the following.

A leading jet with $p_t > 40$ GeV is already required for the considered events. A second tagging jet is expected for a VBF signal event. The $p_t(j2)$-spectrum for the sub-leading jet in the events after the $\Delta\phi_{\ell\ell}$ cut is shown in Fig. 6.18 and the η and ϕ distributions can be found in Fig. BI.6. A second jet with $p_t > 25$ GeV is required for the selection, reducing background contributions from $W \to \ell\nu$ and DY events.

The inclusive number of jets after the $p_t(j2)$ cut is shown in Fig. BI.6.

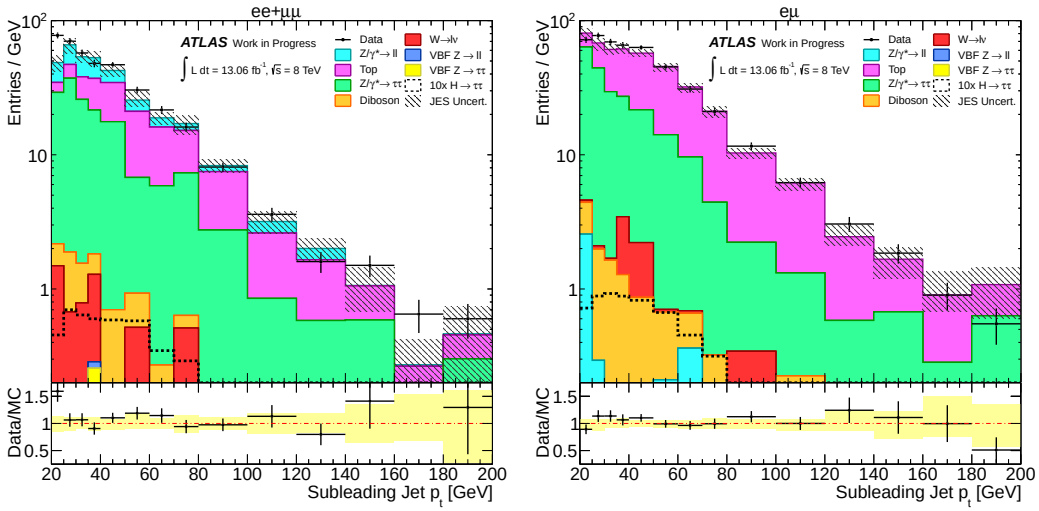

Figure 6.18.: The $p_t(j2)$ spectrum of the sub-leading jet in the selected events after the $\Delta\phi_{\ell\ell}$ requirement.

As motivated in Sec. (6.1), the tagging jets are expected to be well separated in η for a VBF signal event, while the difference in η for the leading jets in the background events is expected to be small.

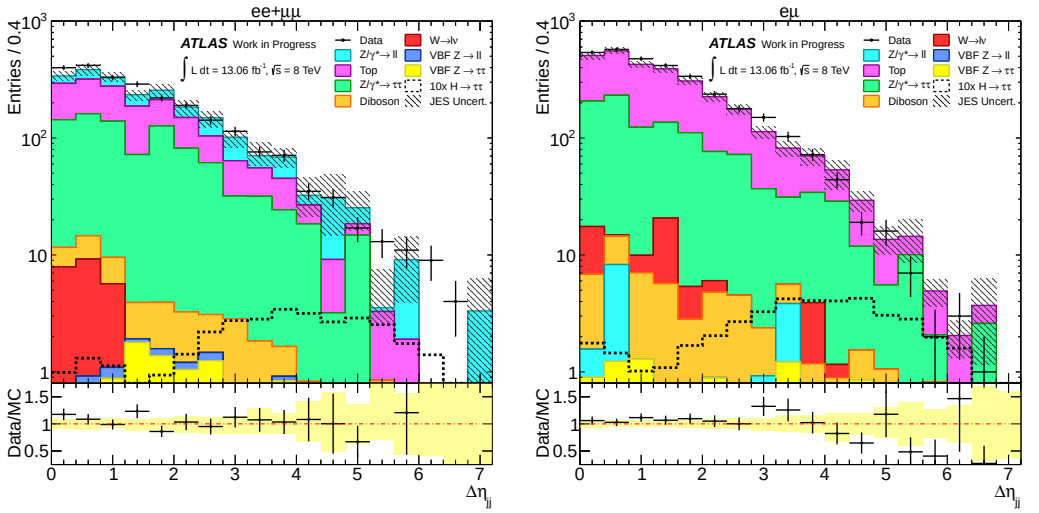

Figure 6.19.: The pseudorapidity difference $\Delta\eta_{jj}$ after requiring a second jet.

In Fig. 6.19, the corresponding distributions for $\Delta\eta_{jj} = |\eta(j1) - \eta(j2)|$ are presented.

For the tagging jets, mainly large $\Delta\eta_{jj} \sim 4$ are modelled, while the majority of the leading jets in the background events only show small $\Delta\eta_{jj} < 2$. An optimal cut value of $\Delta\eta_{jj} > 3.0$ is imposed for the event selection, in order to efficiently suppress large amounts of all background contributions.

Furthermore, the tagging jets in a VBF event typically form a high invariant mass. The distribution for this di-jet mass is shown in Fig. 6.20 after the $\Delta\eta_{jj}$ cut. In order to suppress DY, $t\bar{t}$ and di-boson processes, the di-jet mass is required to exceed $m_{jj} > 400$ GeV.

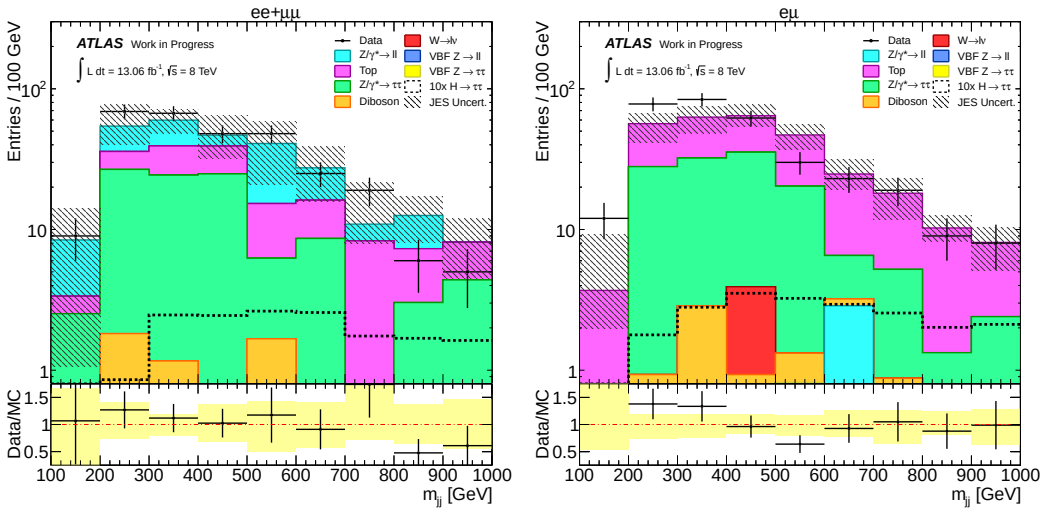

Figure 6.20.: Invariant mass spectrum of the leading jets m_{jj} after the $\Delta\eta_{jj}$.

The event yields at this selection stage are presented in Tab. BII.3. For the combined channel, 35% of the background contribution arises from $Z \to e^+e^-/\mu^+\mu^-$ processes, 34% from top events and 30% from the $Z \to \tau^+\tau^-$ process. A reduction of 95% of the background events is achieved, compared to the yield after the $\Delta\phi_{\ell\ell}$ requirement, while 64% signal are lost. The number of data events is reduced by 95%.
In the $e\mu$ channel, 61% of the background contribution are originating from top processes and 35% from the $Z \to \tau^+\tau^-$ events. Compared to the yield after the $\Delta\phi_{\ell\ell}$ requirement, the background events are reduced by 96% and the signal events by 56%. 95% of the data events are rejected.
In Fig. BI.7 the inclusive number of jets in the remaining events is presented.

In order to suppress remaining background contributions from $t\bar{t}$ and single-top processes, a b-tag veto is applied, using the MV1-tagger, as discussed in Sec. (4). If

a jet with a b-tag weight of > 0.795 is found, the event gets rejected. The impact of this veto, can be inferred by comparing the event yields after the $\Delta\phi_{\ell\ell}$ requirement in Tab. BII.3 with the yields after a veto in Tab. BII.4. Additionally, the inclusive jet multiplicity after the b-tag veto is shown in Fig. BI.8 and can be compared with the multiplicity before the veto in Fig. BI.7. The b-tag veto efficiently rejects 73% of the top background and 26% of the total background in the combined channel, while 1.6% of the signal events is vetoed. 22% of the data events are rejected.
In the $e\mu$ channel, 72% of the top events and 45% of total background processes are vetoed. A loss of 5% of the signal events is expected. In data, 42% events are vetoed.

As motivated in Sec. (6.1), a veto on events with an additional central jet can be applied in order to discriminate between VBF signal and background events. Following [73], the veto on events with additional jets with $p_t(j3) > 25$ GeV within $|\eta| < 2.4$ is applied, if they lie in-between the two leading jets $|\eta_{j1/2}| < |\eta_j 3| < |\eta_{j2/1}|$. This reduces the remaining DY and top background, as can be seen in the p_t spectrum of the third leading jet, fulfilling the centrality constraint in Fig. 6.21.

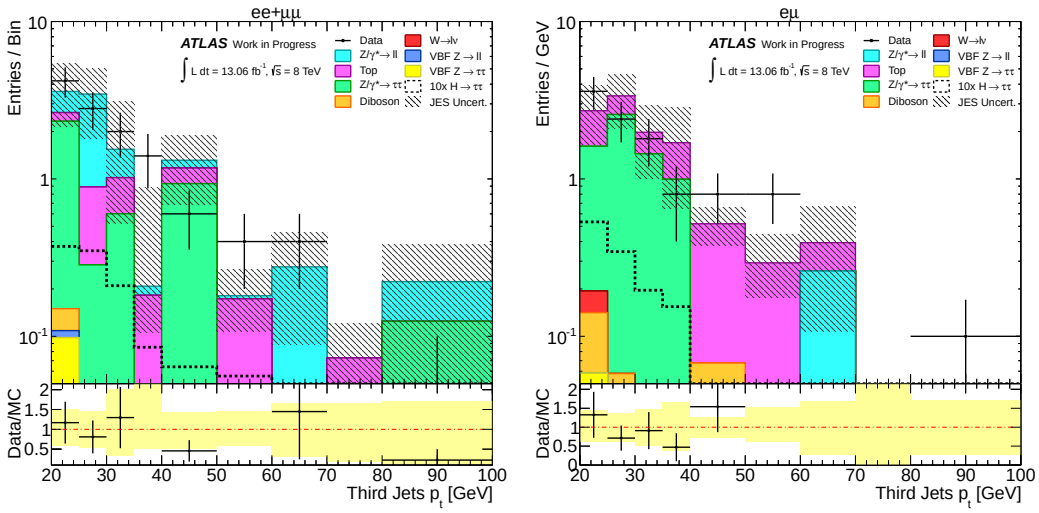

Figure 6.21.: The $p_t(j3)$ spectrum of third leading jet with $|\eta < 2.4|$, located between the tagging jets after the b-tag veto.

The $\eta(j3)$ distributions of third jets in-between the tagging jets without the $|\eta| < 2.4$ requirement is shown in Fig. BI.9. The definition of this central jet veto can be optimised, as will be presented in Sec. (6.6.4).

As a final selection criterium, the leptons in the final state are required to lie

between the two leading jets, i.e.

$$\min(\eta_{j1}, \eta_{j2}) < \eta_{\ell 1,\ell 2} < \max(\eta_{j1}, \eta_{j2}) \tag{6.5}$$

This requirement is another characteristic of the VBF event topology, as explained in Sec. (6.1). The η distributions of the leptons and jets in the events before the cut are shown in Fig. BI.10-BI.11.

This concludes the event selection for VBF $H(\tau^+\tau^-) \to \ell^+\ell^- 4\nu$. The final event yields are depicted in Tab. BII.5. For the combined channel, 1.7 signal events and overall 70 background events remain, of which 54% originate from $Z \to e^+e^-/\mu^+\mu^-$, 30% from the $Z \to \tau^+\tau^-$ processes and 5% from top events.
For the $e\mu$ channel, 2.0 signal events are present after all selection steps. The 43 remaining background events are composed of 59% $Z \to \tau^+\tau^-$ and 31% top contributions.
The statistical uncertainty after the full selection is large, as only a small amount of events survive the selection.

6.6.3. Collinear Mass Approximation

The presence of neutrinos in τ decays introduces an experimental challenge for the exact reconstruction of the kinematics in a $H \to \tau^+\tau^-$ event. Several techniques were proposed to reconstruct the invariant mass $m_{\tau\tau}$ of the τ-pairs, such as the collinear mass approximation, the effective mass or the missing mass calculator [62, 119–121].

As a final observable, the invariant mass $m_{\tau\tau}$ is reconstructed with the collinear approximation in the following. When the mass of the parent particle of the τ-leptons is larger than the mass of the τ-leptons themselves, the latter are boosted in the parent particle's rest frame. For the signal sample with a Higgs mass of 125 GeV this condition is fulfilled.

The collinearity requirement allows to write the energy of the τ as sum of the neutrino's energy E_ν and the visible energy from the lepton E_ℓ, $E_{\tau 1} = E_\ell + E_\nu$. When neglecting the mass of the τ-leptons, $m_\tau \approx 0$, the invariant mass of a di-tau

system can be calculated as

$$\begin{aligned} m_{\tau\tau}^2 &= 2m_\tau^2 + 2(E_{\tau 1}E_{\tau 2} - \vec{p}_{\tau 1}\vec{p}_{\tau 2}) \\ &= 2E_{\tau 1}E_{\tau 2}\,(1 - \cos\vartheta(\tau 1, \tau 2)) \\ &= 2E_{\tau 1}(E_{\ell 1} + E_{\nu 1})(E_{\ell 2} + E_{\nu 2})\,(1 - \cos\vartheta(\tau 1, \tau 2)) \end{aligned} \tag{6.6}$$

where $\vartheta(\tau 1, \tau 2)$ denotes the angle between the two leptons.

The fraction of the τ momentum, which is carried by the neutrinos can be parametrised by the visible momentum fractions $x_{1/2}$, which were introduced earlier. By assuming that the x- and y-components of $\not{E}_T$ are equal to the neutrinos' momenta, the visible momentum fraction can be written as

$$\begin{aligned} x_1 &= \frac{p_1^{\text{vis}}}{p_1^{\text{vis}} + p_1^{\text{miss}}} = \frac{p_x^{\ell 1}p_y^{\ell 2} - p_y^{\ell 1}p_x^{\ell 2}}{p_x^{\ell 1}p_y^{\ell 2} - p_y^{\ell 1}p_x^{\ell 2} + \not{E}_{Tx}p_y^{\ell 2} - \not{E}_{Ty}p_x^{\ell 2}} \\ x_2 &= \frac{p_2^{\text{vis}}}{p_2^{\text{vis}} + p_2^{\text{miss}}} = \frac{p_x^{\ell 1}p_y^{\ell 2} - p_y^{\ell 1}p_x^{\ell 2}}{p_x^{\ell 1}p_y^{\ell 2} - p_y^{\ell 1}p_x^{\ell 2} - \not{E}_{Tx}p_y^{\ell 1} + \not{E}_{Ty}p_x^{\ell 1}} \end{aligned} \quad . \tag{6.7}$$

By combining Equ. 6.6 and Equ. 6.7, the invariant mass of the di-tau system can be written as

$$m_{\tau\tau} = \frac{m_{\ell 1 \ell 2}}{\sqrt{x_1 x_2}} \tag{6.8}$$

when requiring $x_1 x_2 > 0$. The definitions of the visible momentum fractions are only meaningful, if the two τ-leptons do not decay back-to-back in the laboratory frame. This is the case for the Higgs signal and ensured by the $\Delta\phi_{\ell\ell}$ cut.

In Fig. 6.22, the $m_{\tau\tau}$ spectrum following the definition in Equ. 6.8 for the selected events is shown for both channels. The collinear mass for the Higgs signal is near the generated mass of 125 GeV, hence validating the used method.

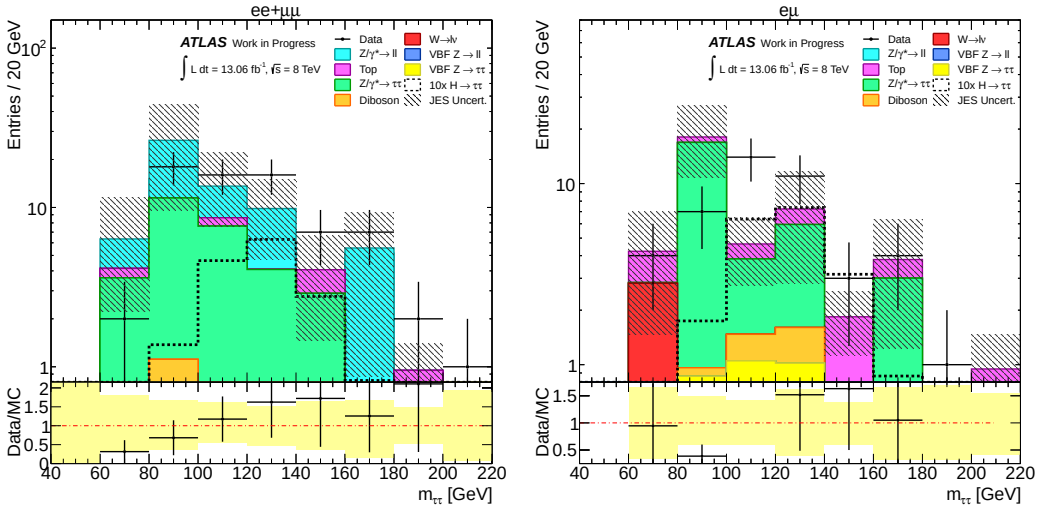

Figure 6.22.: Reconstructed $m_{\tau\tau}$ spectrum in the collinear approximation for events after the full VBF Higgs signal selection.

6.6.4. Central Jet Veto Optimisation Studies

As motivated in Sec. (6.1), the presence of a third jet in a selected VBF event can either indicate a background event, or a higher order signal process, like ISR and FSR or colour reconnection. For the latter processes, only marginal jet activity in the central region is expected.
The definition of a central jet veto (CJV) has to be chosen carefully, such that the topology of the VBF events are described correctly. In the selection in Sec. (6.6.2), a veto on central third jets with $p_t(j3) > 25$ GeV and $|\eta(j3)| < 2.4$ in-between the tagging jets of the VBF event was applied. In the following, three different CJV-observables are defined and compared with this definition in terms of significance for the selection.
For the signal, a Higgs mass of 125 GeV is assumed. The MC samples are normalised to an integrated luminosity of 13.06 fb^{-1}. Only events passing the b-tag veto, as described in Sec. (6.6.2) are considered.

Variables

From the previous considerations in Sec. (6.1) it becomes evident, that a requirement needs to be defined, which allows for a discrimination between background and signal

events with additional jets. This discriminator has to describe the centrality of the additional jets in the VBF events. Four different observables are defined as follows:

- The pseudorapidity of the additional jets in the selected events, denoted as

  $$\eta_{j3}$$

  is considered. For a signal event, the rapidity for an additional jet is expected to be large, as the jet arises from collinear emissions of the tagging jets, which are located in the forward and backward detector region.
  The veto condition is formulated as: If any additional jet is found within an area smaller than the threshold on $|\eta_{j3}|$, the event is rejected.

- The second considered variable is again the pseudorapidity of the additional jet, but with a constraint on the location of the jet. This constraint states, that only jets are considered for the veto, which lie within the tagging jets, i.e.

  $$\eta_{j3}^{\mathrm{c}} \equiv \eta_{j3}, \quad \text{if } \min(\eta_{j1}, \eta_{j2}) < \eta_{j3} < \max(\eta_{j1}, \eta_{j2}) \quad .$$

  The veto condition then states, that events are rejected, if a jet within the threshold $|\eta_{j3}^{\mathrm{c}}|$ is found. If no jet fulfilling the centrality constraint is present, the event is accepted. This corresponds to the veto definition applied in the selection in Sec. (6.6.2), but with a variable $|\eta(j3)|$ threshold.

- Are more sophisticated formulation is introduced with the variable η^*, which is the difference between the pseudorapidity of the additional jet $j3$ and the mean rapidity of the tagging jets, i.e.

  $$\eta^* \equiv \eta_{j3} - \frac{1}{2}(\eta_{j1} + \eta_{j2}) \qquad .$$

  Hence, this observable describes the position of the additional, third jet with repsect to the pseudorapidity difference formed by the two tagging jets. If the third jet is near the centre of both tagging jets, $|\eta^*|$ is very small. Large values for $|\eta^*|$ describe a configuration, where the third jet is near one of the tagging jets. Therefore, a discrimination between background events with central jets and signal events with additional collinear jets is possible.
  The veto therefore states, that events with a jet with $|\eta^*|$ smaller than a certain threshold are rejected.

- The final CJV variable considered in this study, is the direction of the addi-

tional jet with respect to the tagging jets, defined as

$$Z^* \equiv \frac{\eta^*}{|\eta_{j1} - \eta_{j2}|} \quad .$$

It is hence a normalisation of η^* on the pseudorapidity difference of the two leading jets. For a third jet within the region formed by the tagging jets, $|Z^*| < \frac{1}{2}$ and for a third jet outside this region $|Z^*| > \frac{1}{2}$. The veto condition is similar to the previous ones, as only events are accepted, which contain only jets above a certain threshold of $|Z^*|$.

If no third jet is present in the selected events, the event is accepted for all veto definitions.

For the optimisation of the CJV, all introduced variables are calculated after the b-tag veto in Sec. (6.6.2). All additional jets in an event are taken into account for the performance comparison, in order to increase statistics. Furthermore, the $p_t(j3)$ threshold for the considered jets is varied in three steps for all variables. A loose $p_t(j3) > 20$ GeV, a medium $p_t(j3) > 25$ GeV and a tight requirement of $p_t(j3) > 30$ GeV is defined. Each CJV variable is calculated with third jets, which fulfil the applied $p_t(j3)$-criterion. If no jet fulfils the specified requirement, the event is accepted. Hence, for each variable three distributions are calculated. This allows for a two-dimensional optimisation, as the performance between different $p_t(j3)$ thresholds for each variable can be compared.

The distribution for η^* for all additional jets in the events with a threshold of $p_t(j3) > 20$ GeV and $p_t(j3) > 30$ GeV after the b-tag veto are shown in Fig. 6.23. The signal events are enriched for large $\eta^* \sim 3$, which meets the expected behaviour described in Sec. (6.6.4). In Fig. BIII.13-BIII.15, the distributions for all other variables and all thresholds are presented. With increasing p_t-threshold, less additional jets with high p_t are modelled in the MC.

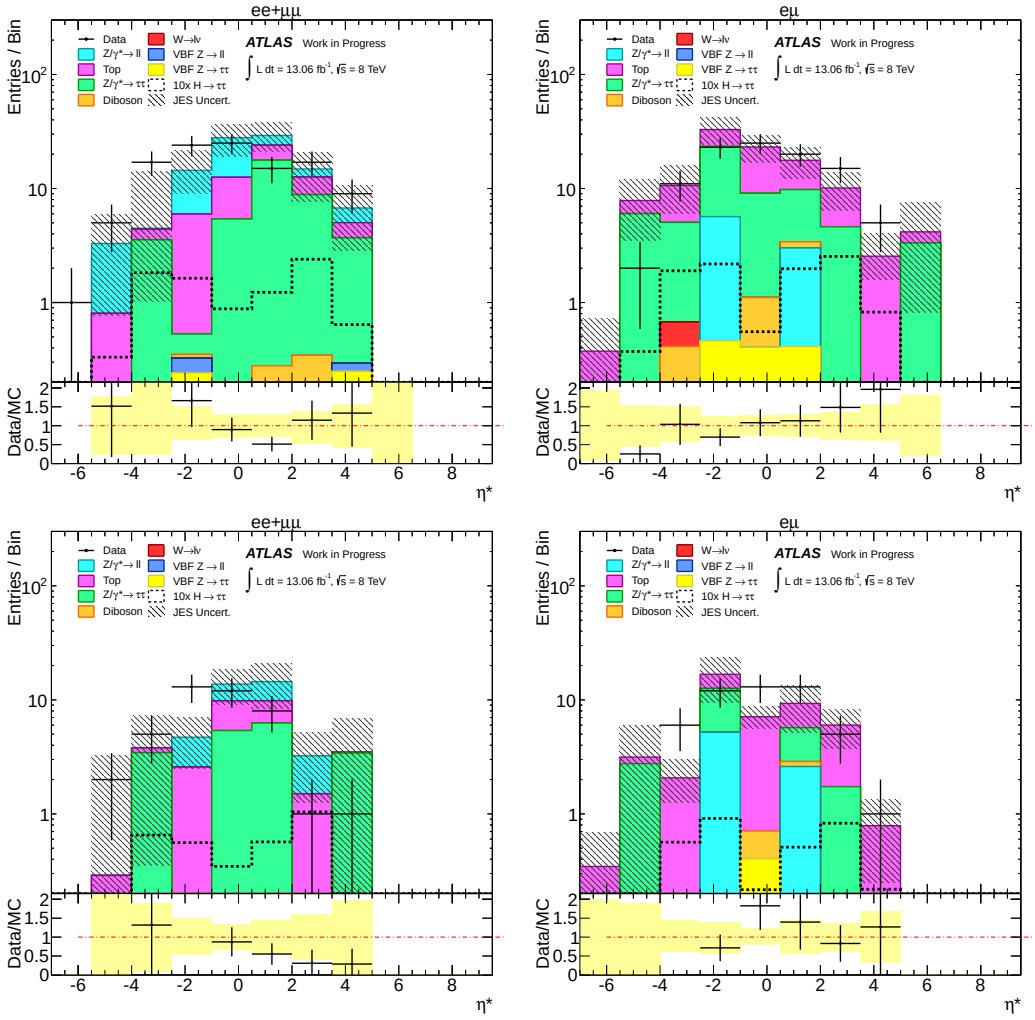

Figure 6.23.: Distribution for η^* and $p_t(j3) > 20$ GeV (top) and $p_t(j3) > 30$ GeV (bottom) after the b-tag veto. The right bin in each distribution contains all events which do not exhibit a third jet above the corresponding $p_t(j3)$ threshold.

Optimisation Strategy

The performances of the CJV definitions are compared, using the selected events from signal and background MC samples. In order to quantify the performance, a figure-of-merit for the significance S of the CJV is defined as

$$S = \frac{N_{\text{Sig}}}{\sqrt{N_{\text{Sig}} + N_{\text{Bg}}}} \tag{6.9}$$

where N_{Sig} denotes the expected number of VBF $H(\tau^+\tau^-) \to \ell^+\ell^- 4\nu$ surviving the veto and N_{Bg} the expected number of remaining background events. The statistical uncertainty of this significance is calculated assuming that $N_{\mathrm{Bg}} >> N_{\mathrm{Sig}}$. The variation is then given as

$$\begin{aligned}\sigma_S^2 &= \left(\frac{\partial S}{\partial N_{\mathrm{Sig}}}\right)^2 \sigma_{N_{\mathrm{Sig}}}^2 + \left(\frac{\partial S}{\partial N_{\mathrm{Bg}}}\right)^2 \sigma_{N_{\mathrm{Bg}}}^2 \\ &= \frac{S^2}{4\left(N_{\mathrm{Sig}} + N_{\mathrm{Bg}}\right)^2}\left[\frac{\left(N_{\mathrm{Sig}} + 2N_{\mathrm{Bg}}\right)^2}{N_{\mathrm{Sig}}^2}\sigma_{N_{\mathrm{Sig}}}^2 + \sigma_{N_{\mathrm{Bg}}}^2\right]\end{aligned}$$

with $\sigma_{N_{\mathrm{Sig}}}^2$ and $\sigma_{N_{\mathrm{Bg}}}^2$ calculated from the quadratic sum of the statistical errors of each bin contributing to N_{Bg} and N_{Sig}. The systematic uncertainty of the event yields is not propagated to the uncertainty of the significance, as a reasonable calculation of the systematics suffers from the lack of statistics.
The veto thresholds are successively raised and the corresponding significance calculated. A high significance corresponds to a good discrimination between signal and background events. Hence, the veto providing the maximal significance will be determined.

Results

In Fig. 6.24-6.25, the significances of the vetos with successively increasing thresholds for all variables is presented for each $p_t(j3)$ threshold on the considered jets. The red line corresponds to the significance of a strict veto, rejecting all events with an additional third jet with $p_t(j3) > 20$ GeV. Each significance curve converges towards the corresponding strict $p_t(j3)$ veto, as it gets unlikely to find additional jets with very high values of the CJV-observables. For better visibility, only the strict $p_t(j3) > 20$ GeV veto is presented.

The statistical errors of the significances in the curves are correlated, since events passing one veto threshold are also included in the previous calculation. An event including a jet with $|\eta^*| = 3$, for example, is contributing to the significance of a veto $|\eta^*| < 2$ as well as to $|\eta^*| < 2.5$. Hence, the statistical errors do not reflect the fluctuation of the curves but rather the overall statistics uncertainty. The errors are therefore only shown for the maximum of the curves. For all variables and each $p_t(j3)$ threshold, the maximal significances are depicted in Tab. 6.6.

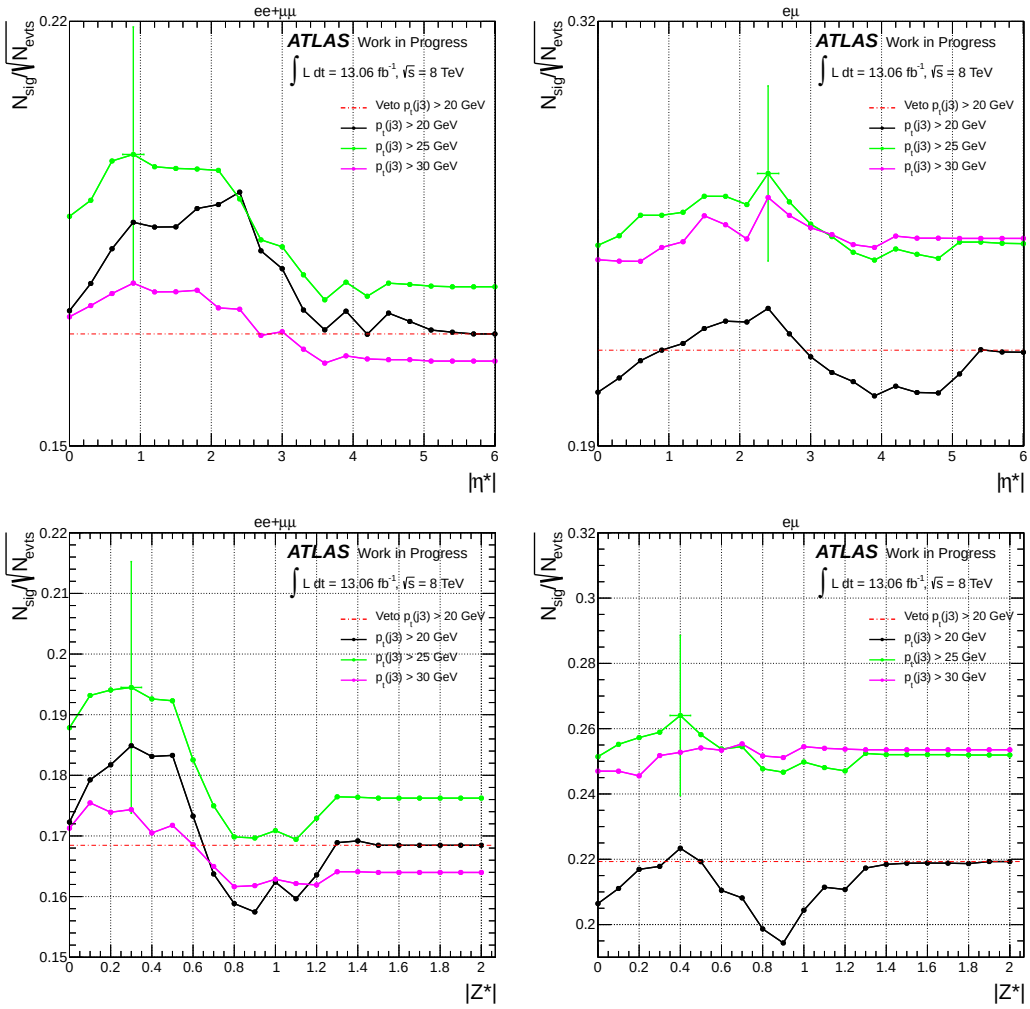

Figure 6.24.: The significances for successively increasing veto thresholds on η^* (top) and Z^* (bottom) are presented. The black line corresponds to the loose, the green to the medium and the pink line to the tight $p_t(j3)$ threshold. The statistical error is only shown for the maximal significance.

For the combined channel, the highest significance among all variables is achieved by a veto on

$$|\eta^c_{j3}| < 0.85 \;\text{ with }\; S = 0.267 \pm 0.024 \;\text{ for }\; p_t(j3) > 25 \text{ GeV}$$

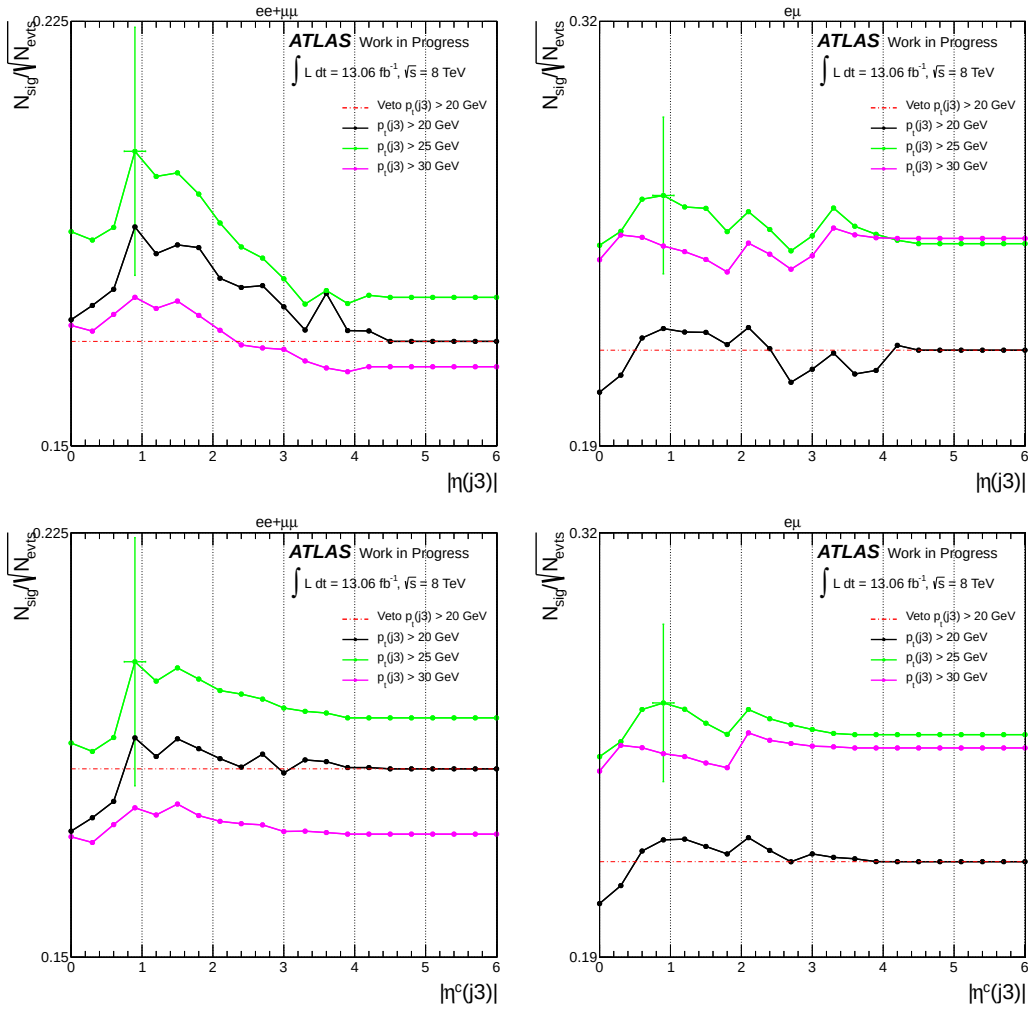

Figure 6.25.: The significances for successively increasing veto thresholds on $\eta_j 3$ (top) and $\eta_j^c 3$ (bottom). The black line corresponds to the loose, the green to the medium and the pink line to the tight $p_t(j3)$ threshold. The statistical error is only shown for the maximal significance.

For the $e\mu$ channel, the veto

$$|\eta^*| < 2.20 \;\text{ with }\; S = 0.278 \pm 0.027 \;\text{ for }\; p_t(j3) > 25 \text{ GeV}$$

is most successful in discriminating background from signal events. In general, a $p_(j3)$ threshold of 25 GeV yields the highest significances.

The standard central jet veto

$$|\eta^{\mathrm{c}}_{j3}| < 2.40 \;\text{ for }\; p_t(j3) > 25 \text{ GeV}$$

applied in the VBF $H(\tau^+\tau^-) \to \ell^+\ell^- 4\nu$ selection in Sec. (6.6.1) yields significances of

- $S = 0.256 \pm 0.025$ for the combined and
- $S = 0.263 \pm 0.025$ for the $e\mu$ channel.

The optimisation of the CJV hence results in a $\sim 4\%$ more significant discrimination between background and signal for the combined channel and $\sim 6\%$ for the $e\mu$ channel compared to the current standard.

Channel	$ee + \mu\mu$		$e\mu$	
$p_t(j3)$	Veto	Significance	Veto	Significance
> 20 GeV	$\lvert\eta_{j3}\rvert < 1.00$	0.189 ± 0.019	$\lvert\eta_{j3}\rvert < 1.25$	0.228 ± 0.017
	$\lvert\eta^{\mathrm{c}}_{j3}\rvert < 1.25$	0.228 ± 0.017	$\lvert\eta^{\mathrm{c}}_{j3}\rvert < 2.10$	0.227 ± 0.018
	$\lvert\eta^*\rvert < 1.95$	0.196 ± 0.023	$\lvert\eta^*\rvert < 2.20$	0.238 ± 0.020
	$\lvert Z^*\rvert < 0.38$	0.186 ± 0.020	$\lvert Z^*\rvert < 0.34$	0.227 ± 0.017
> 25 GeV	$\lvert\eta_{j3}\rvert < 0.90$	0.202 ± 0.022	$\lvert\eta_{j3}\rvert < 0.85$	0.267 ± 0.024
	$\lvert\eta^{\mathrm{c}}_{j3}\rvert < 0.85$	0.267 ± 0.024	$\lvert\eta^{\mathrm{c}}_{j3}\rvert < 0.85$	0.268 ± 0.024
	$\lvert\eta^*\rvert < 1.95$	0.199 ± 0.023	$\lvert\eta^*\rvert < 2.20$	0.278 ± 0.027
	$\lvert Z^*\rvert < 0.14$	0.197 ± 0.020	$\lvert Z^*\rvert < 0.34$	0.266 ± 0.024
> 30 GeV	$\lvert\eta_{j3}\rvert < 0.90$	0.176 ± 0.016	$\lvert\eta_{j3}\rvert < 3.30$	0.257 ± 0.025
	$\lvert\eta^{\mathrm{c}}_{j3}\rvert < 3.30$	0.257 ± 0.025	$\lvert\eta^{\mathrm{c}}_{j3}\rvert < 2.10$	0.259 ± 0.024
	$\lvert\eta^*\rvert < 0.90$	0.177 ± 0.016	$\lvert\eta^*\rvert < 2.20$	0.269 ± 0.025
	$\lvert Z^*\rvert < 0.10$	0.175 ± 0.016	$\lvert Z^*\rvert < 0.62$	0.259 ± 0.025

Table 6.6.: A summary of the optimised discriminating veto thresholds and the resulting significances together with their statistical error is shown for all CJV variables. For example, a veto on $|\eta^*| < 1.0$ means, that all events fulfilling this requirement are rejected.

7. Conclusion and Outlook

In this thesis, a study conducted with data corresponding to an integrated luminosity of 13 fb^{-1} data at $\sqrt{s} = 8$ TeV recorded with the ATLAS detector is presented. The aim of this study is an optimisation of the cut-based selection of $H(\tau^+\tau^-) \to \ell^+\ell^- 4\nu$ events produced in vector boson fusion (VBF) for the search of the Standard Model Higgs boson.

In order to validate the performance of the constructed framework and the Monte Carlo (MC) samples used for the analysis, a control region for studying the Drell-Yan background simulation performance of ALPGEN was defined. At early selection stages, overestimations for the modelling of high-p_t jet kinematics are observed. After selecting a kinematic region similar to the one used to select VBF events, a good agreement between data and MC simulation within the uncertainties is found. As an intermediate result, the survival efficiency for a veto on third jets in the selected events was calculated. The efficiencies reveal, that most of the additional jets in the Drell-Yan background events carry a low transverse momentum, as they converge to 1 for high-p_t thresholds. Only small deviations of $\sim 4\%$ between data and MC simulation are observed for veto-efficiencies at low-p_t thresholds. Hence, ALPGEN provides a satisfying simulation performance of the background modelling for the VBF Higgs signal region.

After the validation, the selection of VBF $H(\tau^+\tau^-) \to \ell^+\ell^- 4\nu$ events was performed. For the three lepton flavour combinations in the final state, ee, $\mu\mu$ and $e\mu$, the effects of each selection step was studied in data and simulation. The ee and $\mu\mu$ channels were combined to increase statistics. A good agreement between simulation and data within the uncertainties is observed. As a final discriminant, the invariant mass of the two *tau*-leptons from the Higgs decay was reconstructed after the selection, using the collinear approximation.

An important characteristic of the VBF $H(\tau^+\tau^-) \to \ell\ell 4\nu$ event signature is a marginal jet activity in the central region. In order to discriminate background and signal events, a central jet veto (CJV) was applied in the selection. For the

optimisation of the selection, different definitions for the CJV were investigated and compared. The most successful discriminating definition was determined by maximising the significance for the signal selection.
For the $ee + \mu\mu$ channel, a veto on third jets located between the tagging jets with $p_t(j3) > 25$ GeV and $|\eta| < 0.85$ provides the highest significance. Vetoing events including third jets with $|\eta^*| < 2.20$, proved to be the best discriminator in the $e\mu$ channel. Compared to the veto applied in the VBF $H(\tau^+\tau^-) \to \ell^+\ell^- 4\nu$ selection, a $4 - 6\%$ higher significance was achieved.

Outlook For a complete picture of the study, all systematic uncertainties on the normalisation and physics object reconstruction need to be taken into account.
In order to expedite the analysis efforts of the Higgs physics group in Göttingen, the constructed framework can be delocalised and moved to the GRID for analysis runs. This would simplify programming validations and increase the speed of the analysis runs.
Multivariate analysis (MVA) techniques take into account the impact of a variation in one variable on the other considered observables. This gives an advantage over cut-based optimisations, as multi-dimensional cross-checks can be conducted and the impact on the whole analysis can be studied. The usage of such a MVA for the CJV optimisation would hence result in a more mature statement and increased sensitivity and should be used for full exploitation of the CJV.
The final discrimination between signal and background events can be performed, by using a more sophisticated reconstruction of the τ-pair mass, like the Missing Mass Calculator (MMC) and fitting the MMC mass after applying the MVA selection.

In order to state, whether the discovered boson is indeed the SM Higgs boson with certainty, its coupling to fermions, triple and quartic self couplings, spin and parity properties, as well as signal strength for all channels need to be studied precisely in future analyses.

A. Studies in a $Z \to e^+e^-$ Control Region

I. Control Plots

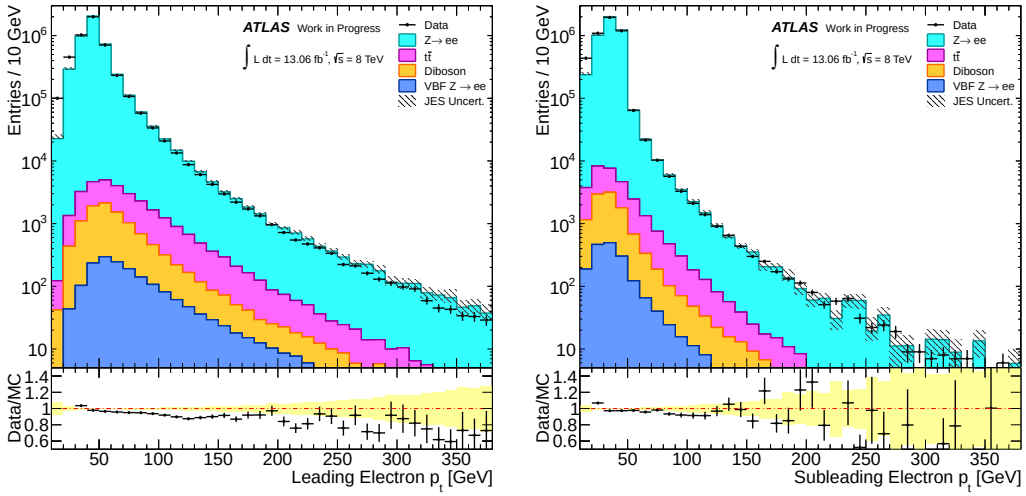

Figure AI.1.: The p_t spectrum of the leading electron (left) and sub-leading electron (right) after the preselection.

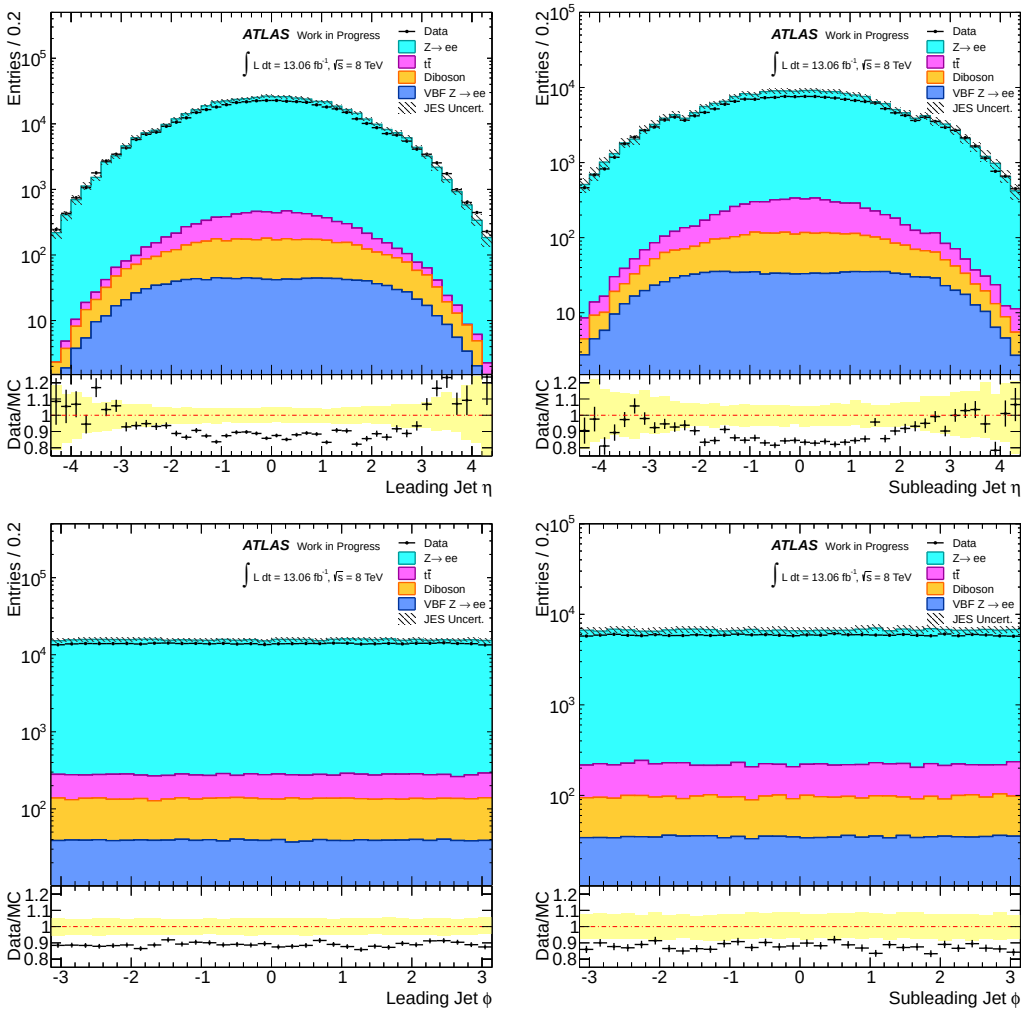

Figure AI.2.: The η and ϕ distributions of the leading (left) and sub-leading jet (right) for $Z \to e^+e^-$ events after the mass window requirement.

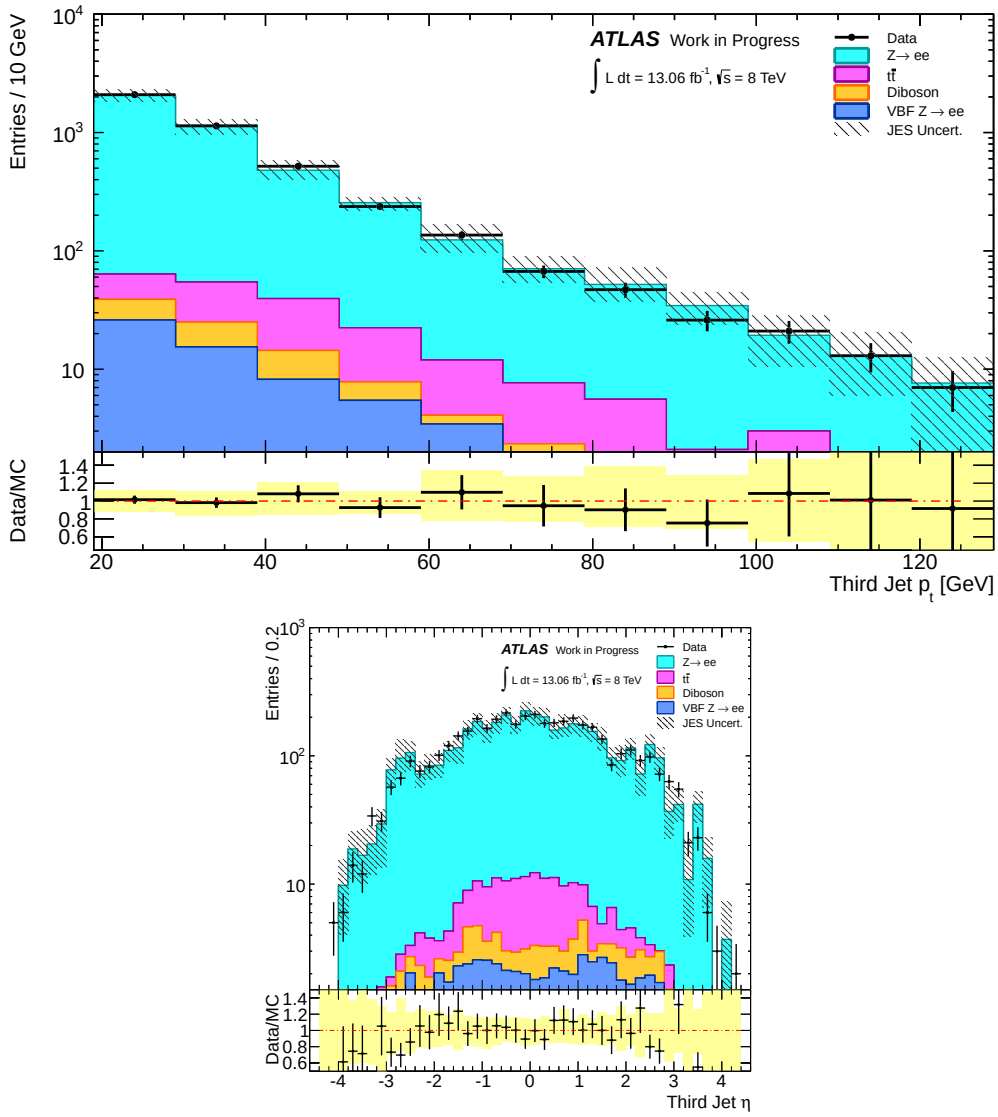

Figure AI.3.: The p_t, η and ϕ distributions for third jets in-between the two leading jets for the $Z \to e^+e^-$ events after the m_{jj} requirement.

II. Event Yield Tables

Process	#Events	Syst. Uncert.	Stat. Uncert.
$Z/\gamma^* \to e^+e^- + jets$	4159109	$^{+0}_{-2}$	± 3438
Top	4947	$^{+0}_{-0}$	± 38
Di-boson	5494	$^{+0}_{-0}$	± 27
VBF $Z/\gamma^* \to e^+e^-$	1388	$^{+0}_{-0}$	± 4
MC Sum	4170938	$^{+0}_{-2}$	± 3438
Data	4054402	-	± 2014

Table AII.1.: Event yields for the $Z \to ee$ candidates after the mass window cut.

Process	#Events	Syst. Uncert.	Stat. Uncert.
$Z/\gamma^* \to e^+e^- + jets$	11348	$^{+1550}_{-1254}$	± 192
Top	192	$^{+12}_{-8}$	± 8
Di-boson	81	$^{+8}_{-8}$	± 3
VBF $Z/\gamma^* \to e^+e^-$	376	$^{+9}_{-10}$	± 2
MC Sum	11994	$^{+1550}_{-1254}$	± 192
Data	11632	-	± 108

Table AII.2.: Event yields for the $Z \to e^+e^-$ candidates after the m_{jj} requirement.

B. Studies for VBF $H(\tau^+\tau^-) \to \ell^+\ell^- 4\nu$ Searches

I. Control Plots

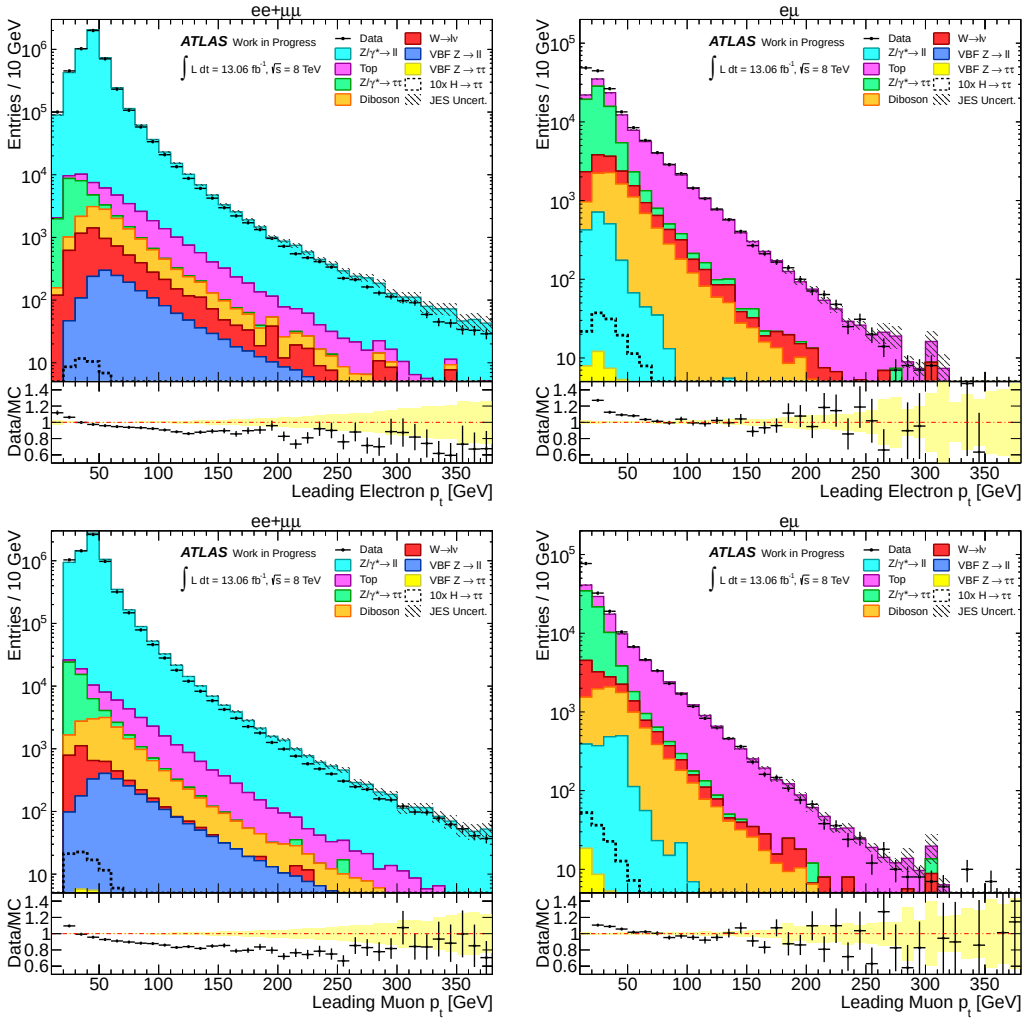

Figure BI.1.: p_t spectra for the leading leptons after the preselection.

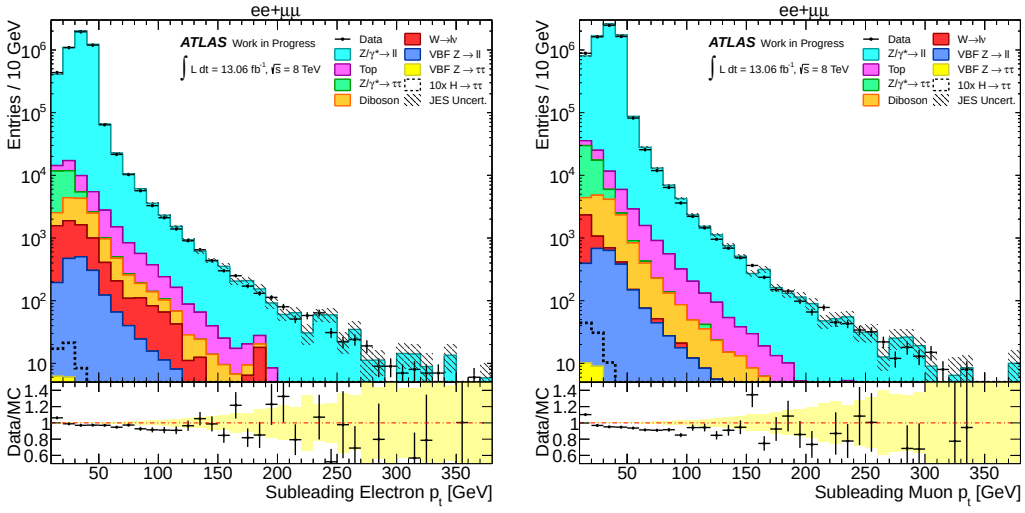

Figure BI.2.: p_t spectra for the subleading leptons.

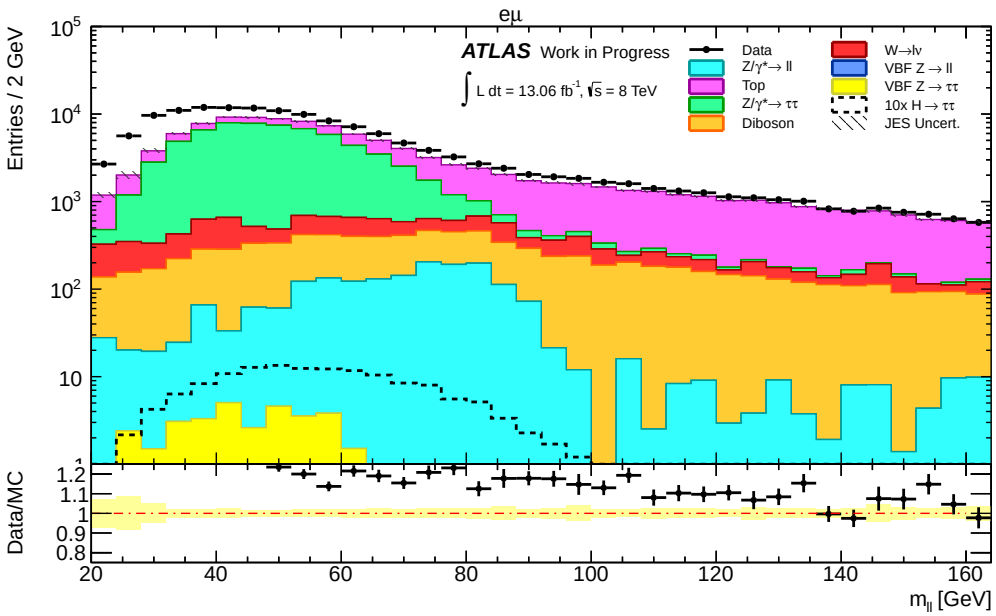

Figure BI.3.: Invariant mass spectrum of the selected leptons in the $e\mu$ channel after the lepton requirement.

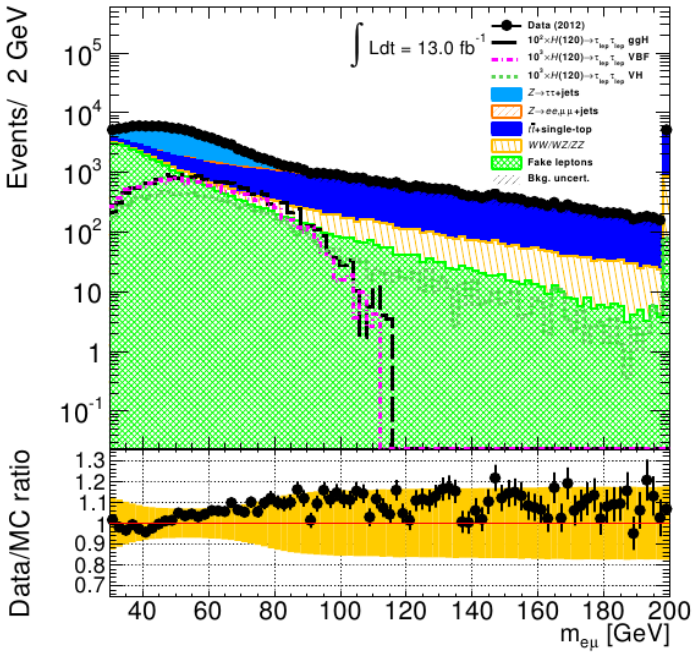

Figure BI.4.: Invariant mass spectrum for $e\mu$ channel from [73].

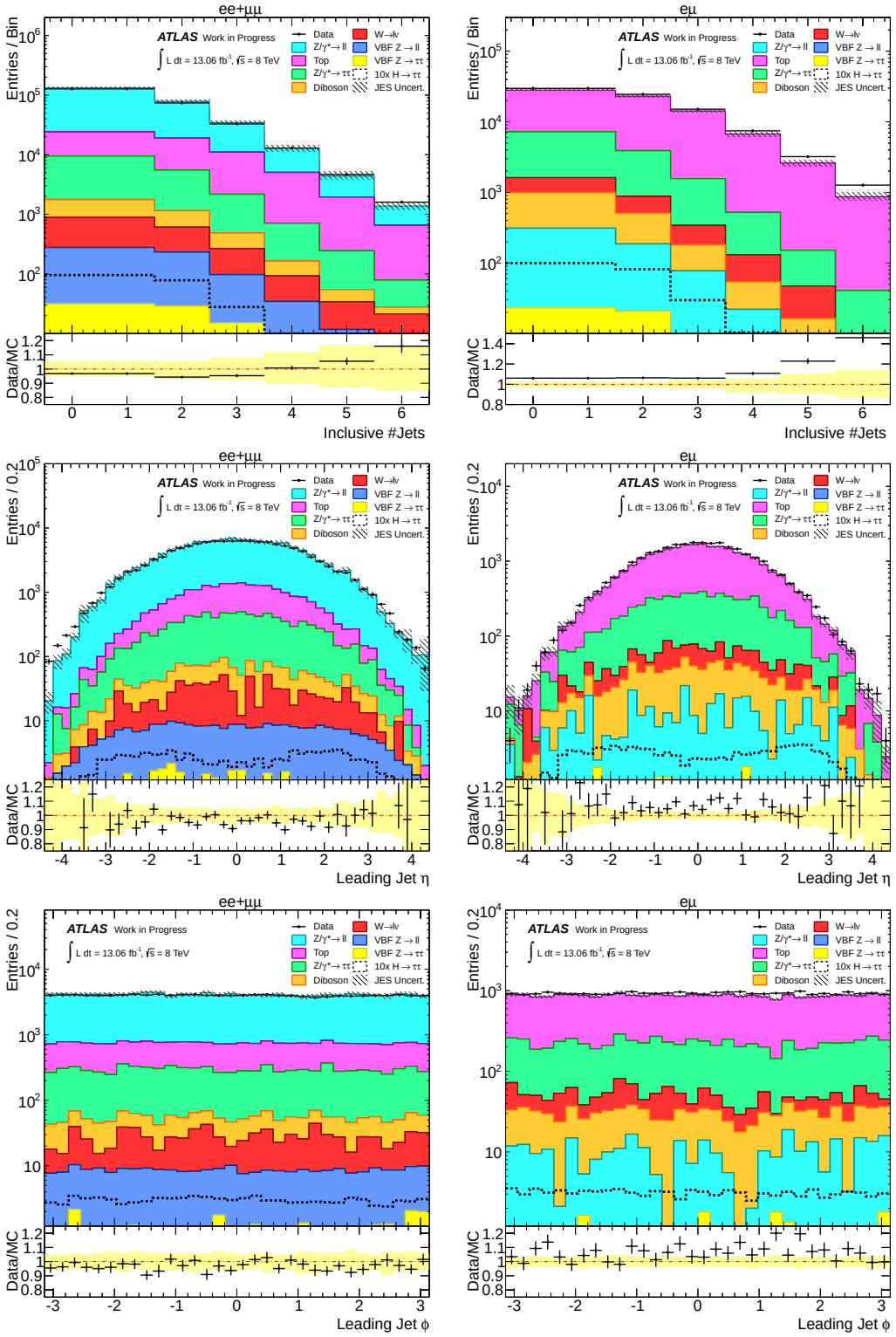

Figure BI.5.: Inclusive Jet multiplicity (top), η (middle) and ϕ (bottom) spectra for leading jets with $p_t > 40$ GeV after the di-lepton p_t requirement.

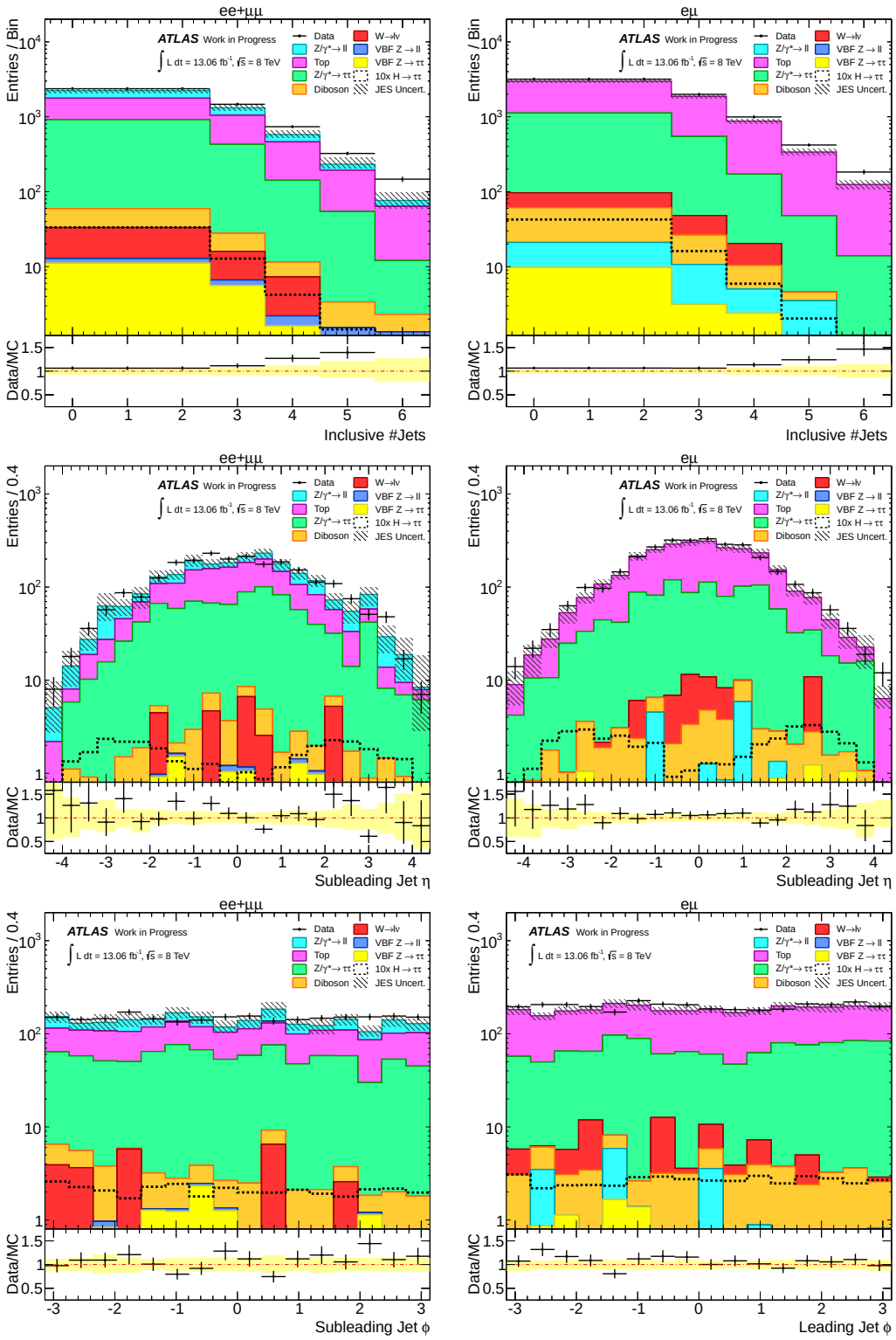

Figure BI.6.: Inclusive Jet multiplicity (top), η (middle) and ϕ (bottom) spectra for subleading jets with $p_t > 25$ GeV after the $\Delta\phi_{\ell\ell}$ cut.

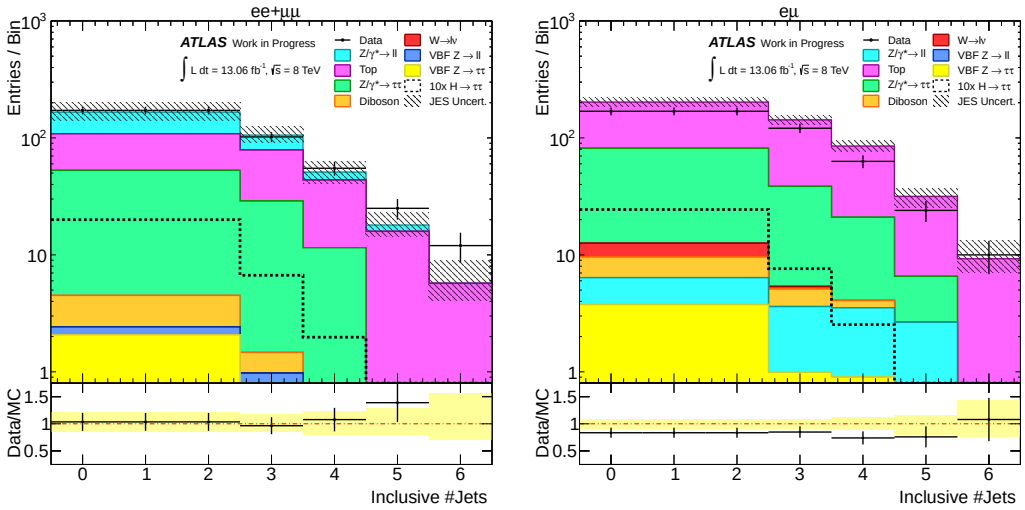

Figure BI.7.: Inclusive jet multiplicity after m_{jj} requirement.

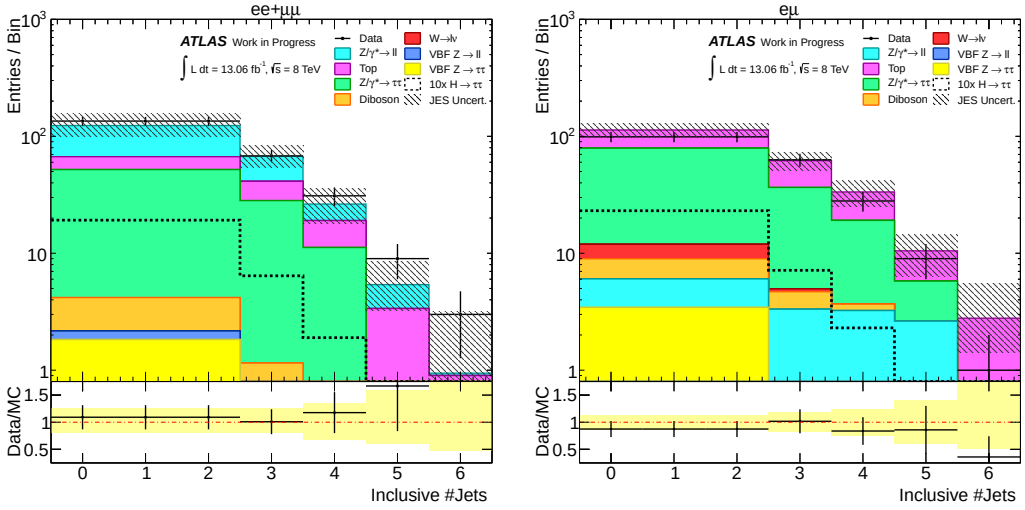

Figure BI.8.: Inclusive jet multiplicity after b-tag veto.

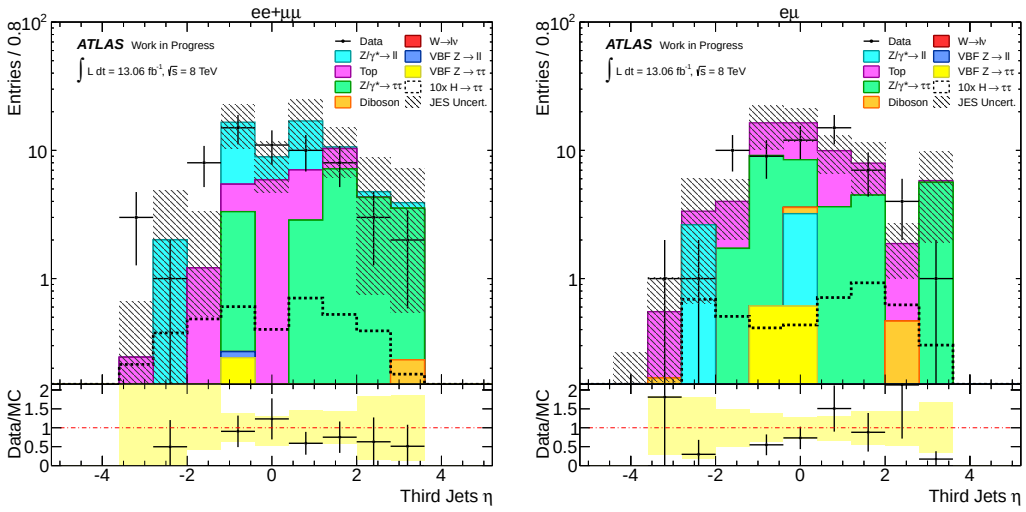

Figure BI.9.: η distribution for central third jets with $p_t(j3) > 25$ GeV after b-tag veto.

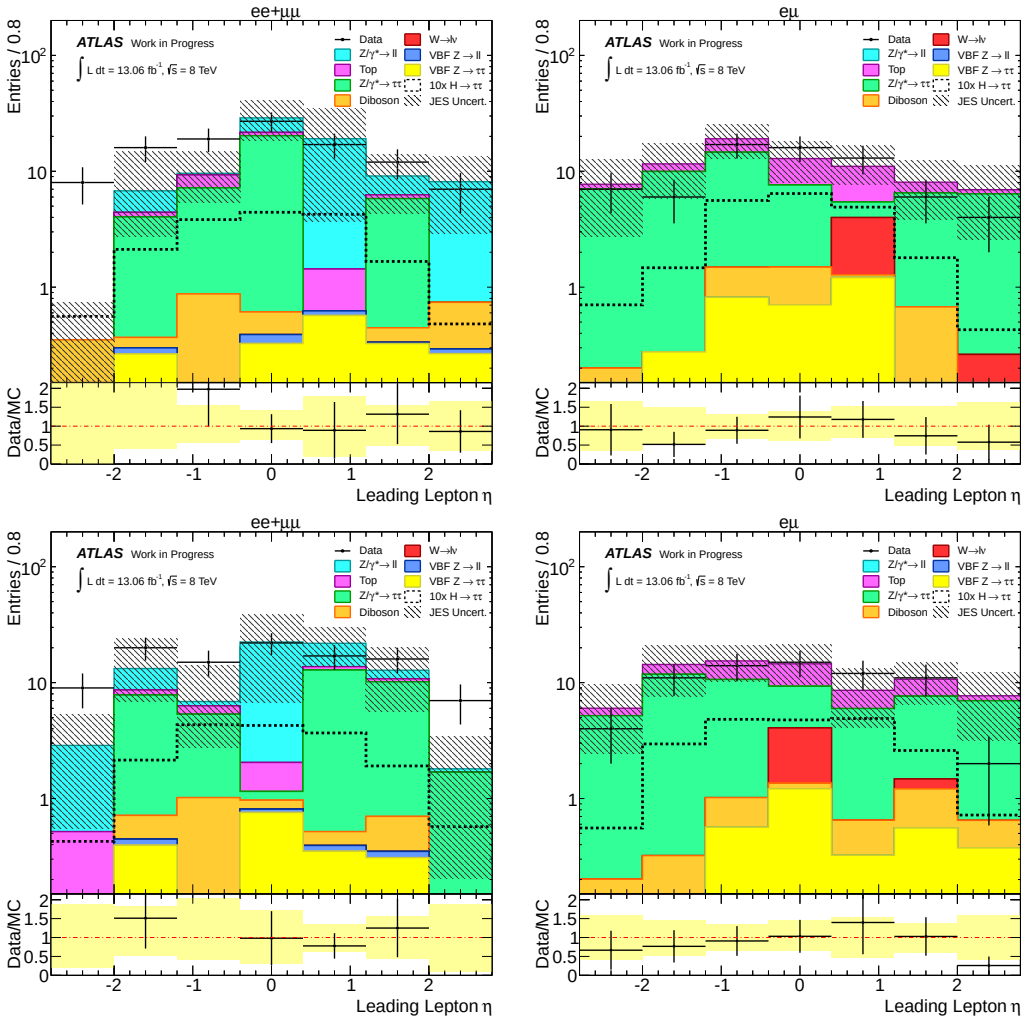

Figure BI.10.: η spectra for the leading leptons the central jet veto.

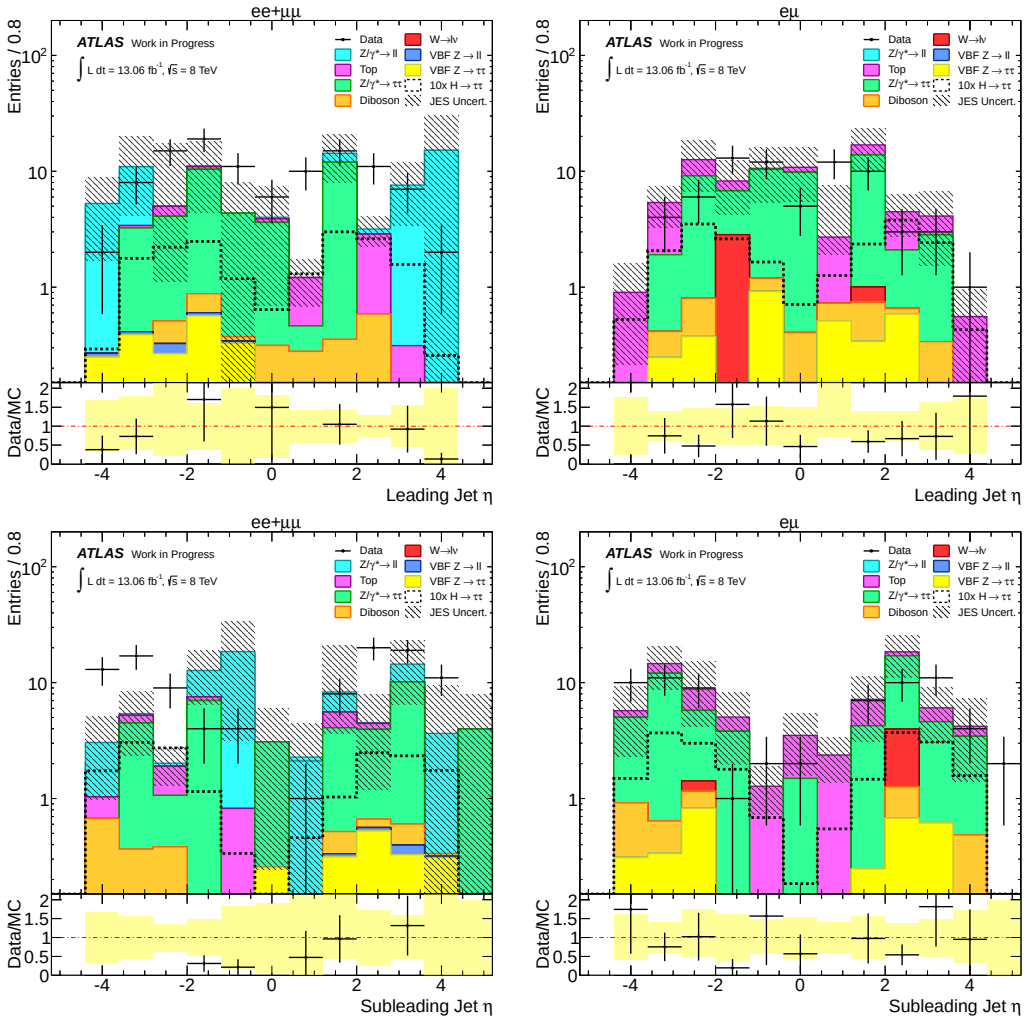

Figure BI.11.: η spectra for the leading jets after the central jet veto.

II. Event Yield Tables

In this section, the event yields for selected cut-stages of the VBF $H(\tau^+\tau^-) \to \ell^+\ell^- 4\nu$ selection are presented. The MC samples used for modelling the physics processes are discussed in Sec. (5.3).

The tables are organised as follows: The upper table shows the event yields for the combined $e^+e^- + \mu^+\mu^-$ channel and the lower table the yields for the $e\mu$ channel. The tables contain the number of events and their systematic and statistical uncertainty. The contributions from the background are summed and their uncertainties combined. Furthermore, the event yields for the selected data is presented, but, as not applicable, without systematics.

Combined $e^+e^- + \mu^+\mu^-$ channel			
Process	#Events	Syst. error	Stat. Error
$Z/\gamma^* \to e^+e^-/\mu^+\mu^- + jets$	1023578	$^{+0}_{-0}$	± 6559
Top	15877	$^{+0}_{-0}$	± 70
$Z/\gamma^* \to \tau^+\tau^- + jets$	54911	$^{+0}_{-0}$	± 411
Di-boson	3717	$^{+0}_{-0}$	± 24
$W \to \ell\nu$	3332	$^{+0}_{-0}$	± 264
VBF $Z/\gamma^* \to e^+e^-/\mu^+\mu^-$	461	$^{+0}_{-0}$	± 3
VBF $Z/\gamma^* \to \tau^+\tau^-$	188	$^{+0}_{-0}$	± 87
VBF $H(\tau^+\tau^-) \to \ell^+\ell^-$	11.55	$^{+0.01}_{-0.01}$	± 0.17
Background Sum	1102063	$^{+0}_{-0}$	± 6578
Data	1101559	–	± 1050

$e^\pm\mu^\mp$ channel			
Process	#Events	Syst. error	Stat. Error
$Z/\gamma^* \to e^+e^-/\mu^+\mu^- + jets$	1689	$^{+0}_{-0}$	± 73
Top	23640	$^{+0}_{-0}$	± 85
$Z/\gamma^* \to \tau^+\tau^- + jets$	55519	$^{+0}_{-0}$	± 415
Di-boson	4373	$^{+0}_{-0}$	± 27
$W \to \ell\nu$	3712	$^{+0}_{-0}$	± 237
VBF $Z/\gamma^* \to e^+e^-/\mu^+\mu^-$	0.9	$^{+0}_{-0}$	± 0.1
VBF $Z/\gamma^* \to \tau^+\tau^-$	246	$^{+0}_{-0}$	± 111
VBF $H(\tau^+\tau^-) \to \ell^+\ell^-$	13.66	$^{+0.01}_{-0.01}$	± 0.19
Background Sum	89180	$^{+0}_{-0}$	± 504
Data	116594	–	± 341

Table BII.1.: Event yields after the mass window requirement.

Combined $e^+e^- + \mu^+\mu^-$ channel			
Process	#Events	Syst. error	Stat. Error
$Z/\gamma^* \to e^+e^-/\mu^+\mu^- + jets$	697	$^{+35}_{-52}$	± 52
Top	934	$^{+25}_{-22}$	± 17
$Z/\gamma^* \to \tau^+\tau^- + jets$	1608	$^{+83}_{-58}$	± 75
Di-boson	46	$^{+2}_{-1}$	± 3
$W \to \ell\nu$	40	$^{+6}_{-0}$	± 12
VBF $Z/\gamma^* \to e^+e^-/\mu^+\mu^-$	2.4	$^{+0.2}_{-0.2}$	± 0.2
VBF $Z/\gamma^* \to \tau^+\tau^-$	8	$^{+0}_{-0}$	± 7
VBF $H(\tau^+\tau^-) \to \ell^+\ell^-$	4.13	$^{+0.08}_{-0.10}$	± 0.10
Background Sum	3335	$^{+94}_{-81}$	± 94
Data	3693	–	± 61

$e^\pm\mu^\mp$ channel			
Process	#Events	Syst. error	Stat. Error
$Z/\gamma^* \to e^+e^-/\mu^+\mu^- + jets$	35	$^{+0}_{-0}$	± 11
Top	2089	$^{+6}_{-9}$	± 25
$Z/\gamma^* \to \tau^+\tau^- + jets$	2310	$^{+24}_{-43}$	± 89
Di-boson	85	$^{+1}_{-2}$	± 4
$W \to \ell\nu$	47	$^{+0}_{-0}$	± 13
VBF $Z/\gamma^* \to e^+e^-/\mu^+\mu^-$	0.09	$^{+0}_{-0}$	0.04
VBF $Z/\gamma^* \to \tau^+\tau^-$	4	$^{+0}_{-0}$	± 4
VBF $H(\tau^+\tau^-) \to \ell^+\ell^-$	5.56	$^{+0.03}_{-0.02}$	± 0.12
Background Sum	4570	$^{+25}_{-44}$	± 94
Data	4736	–	± 69

Table BII.2.: Event yields after the $\Delta\phi_{\ell\ell}$ requirement.

Combined $e^+e^- + \mu^+\mu^-$ channel			
Process	#Events	Syst. error	Stat. Error
$Z/\gamma^* \to e^+e^-/\mu^+\mu^- + jets$	58	$^{+4}_{-3}$	± 19
Top	56	$^{+3}_{-4}$	± 4
$Z/\gamma^* \to \tau^+\tau^- + jets$	48	$^{+20}_{-0}$	± 13
Di-boson	2.1	$^{+0.3}_{-0.0}$	± 0.6
$W \to \ell\nu$	0	$^{+0}_{-0}$	–
VBF $Z/\gamma^* \to e^+e^-/\mu^+\mu^-$	0.34	$^{+0.08}_{-0.07}$	± 0.06
VBF $Z/\gamma^* \to \tau^+\tau^-$	0.2	$^{+0}_{-0}$	± 0.2
VBF $H(\tau^+\tau^-) \to \ell^+\ell^-$	2.00	$^{+0.09}_{-0.09}$	± 0.07
Background Sum	164	$^{+20}_{-5}$	± 23
Data	172	–	± 13

$e^\pm\mu^\mp$ channel			
Process	#Events	Syst. error	Stat. Error
$Z/\gamma^* \to e^+e^-/\mu^+\mu^- + jets$	3	$^{+0}_{-0}$	± 3
Top	121	$^{+2}_{-3}$	± 6
$Z/\gamma^* \to \tau^+\tau^- + jets$	69	$^{+2}_{-0}$	± 15
Di-boson	3.2	$^{+0.4}_{-0.8}$	± 0.7
$W \to \ell\nu$	3	$^{+0}_{-0}$	± 3
VBF $Z/\gamma^* \to e^+e^-/\mu^+\mu^-$	0.04	$^{+0}_{-0}$	0.03
VBF $Z/\gamma^* \to \tau^+\tau^-$	0	$^{+0}_{-0}$	± 0
VBF $H(\tau^+\tau^-) \to \ell^+\ell^-$	2.44	$^{+0.08}_{-0.10}$	± 0.08
Background Sum	199	$^{+3}_{-3}$	± 16
Data	169	–	± 13

Table BII.3.: Event yields after the m_{jj} requirement.

Combined $e^+e^- + \mu^+\mu^-$ channel			
Process	#Events	Syst. error	Stat. Error
$Z/\gamma^* \to e^+e^-/\mu^+\mu^- + jets$	56.70	$^{+3.28}_{-2.90}$	± 18.89
Top	15.01	$^{+0.27}_{-0.85}$	± 2.42
$Z/\gamma^* \to \tau^+\tau^- + jets$	47.77	$^{+19.17}_{-0}$	± 12.63
Di-boson	2.01	$^{+0.32}_{-0.03}$	± 0.60
$W \to \ell\nu$	0	$^{+0}_{-0}$	–
VBF $Z/\gamma^* \to e^+e^-/\mu^+\mu^-$	0.34	$^{+0.08}_{-0.07}$	± 0.06
VBF $Z/\gamma^* \to \tau^+\tau^-$	0.18	$^{+0}_{-0}$	± 0.18
VBF $H(\tau^+\tau^-) \to \ell^+\ell^-$	1.92	$^{+0.09}_{-0.08}$	± 0.07
Background Sum	122.01	$^{+19.46}_{-3.02}$	± 22.86
Data	135.00	–	± 11.62

$e^\pm\mu^\mp$ channel			
Process	#Events	Syst. error	Stat. Error
$Z/\gamma^* \to e^+e^-/\mu^+\mu^- + jets$	3	$^{+0}_{-0}$	± 3
Top	34.11	$^{+0.59}_{-1.08}$	± 3.66
$Z/\gamma^* \to \tau^+\tau^- + jets$	67.24	$^{+1.67}_{-0.02}$	± 14.44
Di-boson	2.93	$^{+0.42}_{-0.7}$	± 0.7
$W \to \ell\nu$	2.97	$^{+0}_{-0}$	± 2.72
VBF $Z/\gamma^* \to e^+e^-/\mu^+\mu^-$	0.02	$^{+0}_{-0}$	0.02
VBF $Z/\gamma^* \to \tau^+\tau^-$	0	$^{+0}_{-0}$	± 0
VBF $H(\tau^+\tau^-) \to \ell^+\ell^-$	2.31	$^{+0.07}_{-0.09}$	± 0.08
Background Sum	109.87	$^{+1.82}_{-1.29}$	± 15.38
Data	99.	–	± 9.95

Table BII.4.: Event yields after the b-tag veto.

Combined $e^+e^- + \mu^+\mu^-$ channel			
Process	#Events	Syst. error	Stat. Error
$Z/\gamma^* \to e^+e^-/\mu^+\mu^- + jets$	37.64	$^{+0.31}_{-2.83}$	$\pm$17.13
Top	3.77	$^{+0.21}_{-0.23}$	$\pm$1.11
$Z/\gamma^* \to \tau^+\tau^- + jets$	26.73	$^{+14.64}_{-0.09}$	$\pm$10.24
Di-boson	1.75	$^{+0.32}_{-0.03}$	$\pm$0.58
$W \to \ell\nu$	0	$^{+0}_{-0}$	–
VBF $Z/\gamma^* \to e^+e^-/\mu^+\mu^-$	0.26	$^{+0.03}_{-0.04}$	$\pm$0.05
VBF $Z/\gamma^* \to \tau^+\tau^-$	0.00	$^{+0}_{-0}$	–
VBF $H(\tau^+\tau^-) \to \ell^+\ell^-$	1.65	$^{+0.06}_{-0.06}$	$\pm$0.06
Background Sum	70.14	$^{+14.65}_{-3.13}$	$\pm$20.00
Data	71.00	–	$\pm$8.43

$e^\pm\mu^\mp$ channel			
Process	#Events	Syst. error	Stat. Error
$Z/\gamma^* \to e^+e^-/\mu^+\mu^- + jets$	0	$^{+0}_{-0}$	–
Top	13.27	$^{+0.18}_{-0.34}$	$\pm$2.26
$Z/\gamma^* \to \tau^+\tau^- + jets$	25.20	$^{+0.00}_{-4.98}$	$\pm$8.98
Di-boson	1.77	$^{+0.42}_{-0.50}$	$\pm$0.55
$W \to \ell\nu$	2.71	$^{+0}_{-0}$	$\pm$2.71
VBF $Z/\gamma^* \to e^+e^-/\mu^+\mu^-$	0.02	$^{+0}_{-0}$	0.02
VBF $Z/\gamma^* \to \tau^+\tau^-$	0	$^{+0}_{-0}$	–
VBF $H(\tau^+\tau^-) \to \ell^+\ell^-$	2.041	$^{+0.05}_{-0.07}$	$\pm$0.07
Background Sum	42.98	$^{+0.46}_{-5.01}$	$\pm$9.66
Data	47.00	–	$\pm$6.86

Table BII.5.: Final event yields.

III. CJV Variables

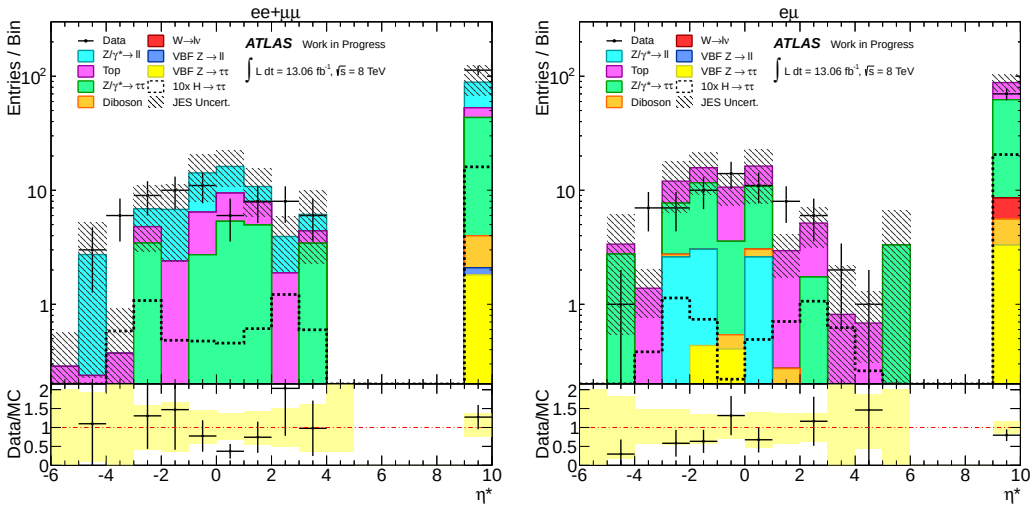

Figure BIII.12.: η^* for additional jets with $p_t > 25$GeV after the b-tag veto.

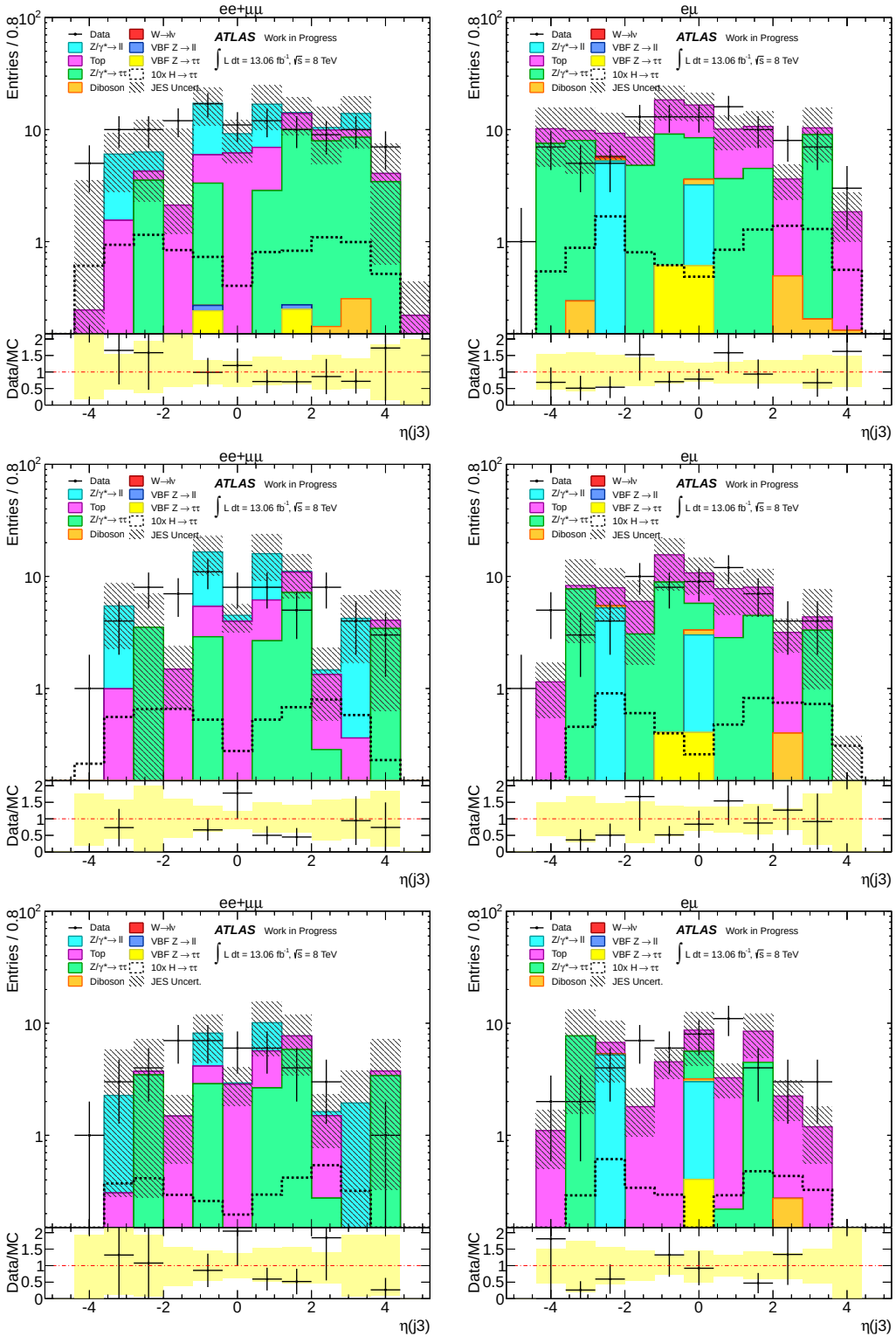

Figure BIII.13.: η_{j3} for additional jets with $p_t > 20$GeV (top),$p_t > 25$GeV (middle) and $p_t > 30$ GeV (bottom) after the b-tag veto.

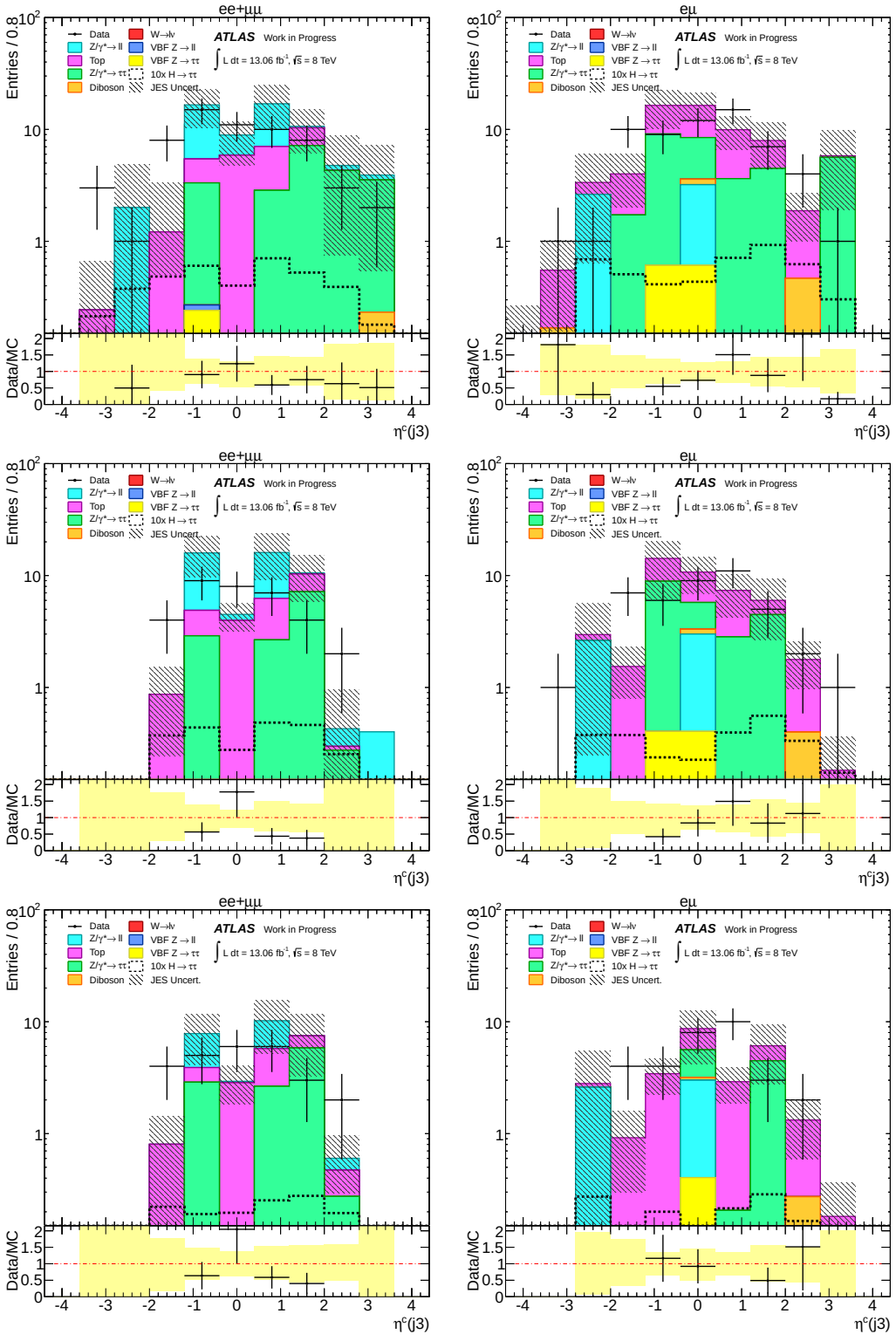

Figure BIII.14.: $\eta_{j3}^{\text{Central}}$ for additional jets with $p_t > 20$GeV (top),$p_t > 25$GeV (middle) and $p_t > 30$ GeV (bottom) after the b-tag veto.

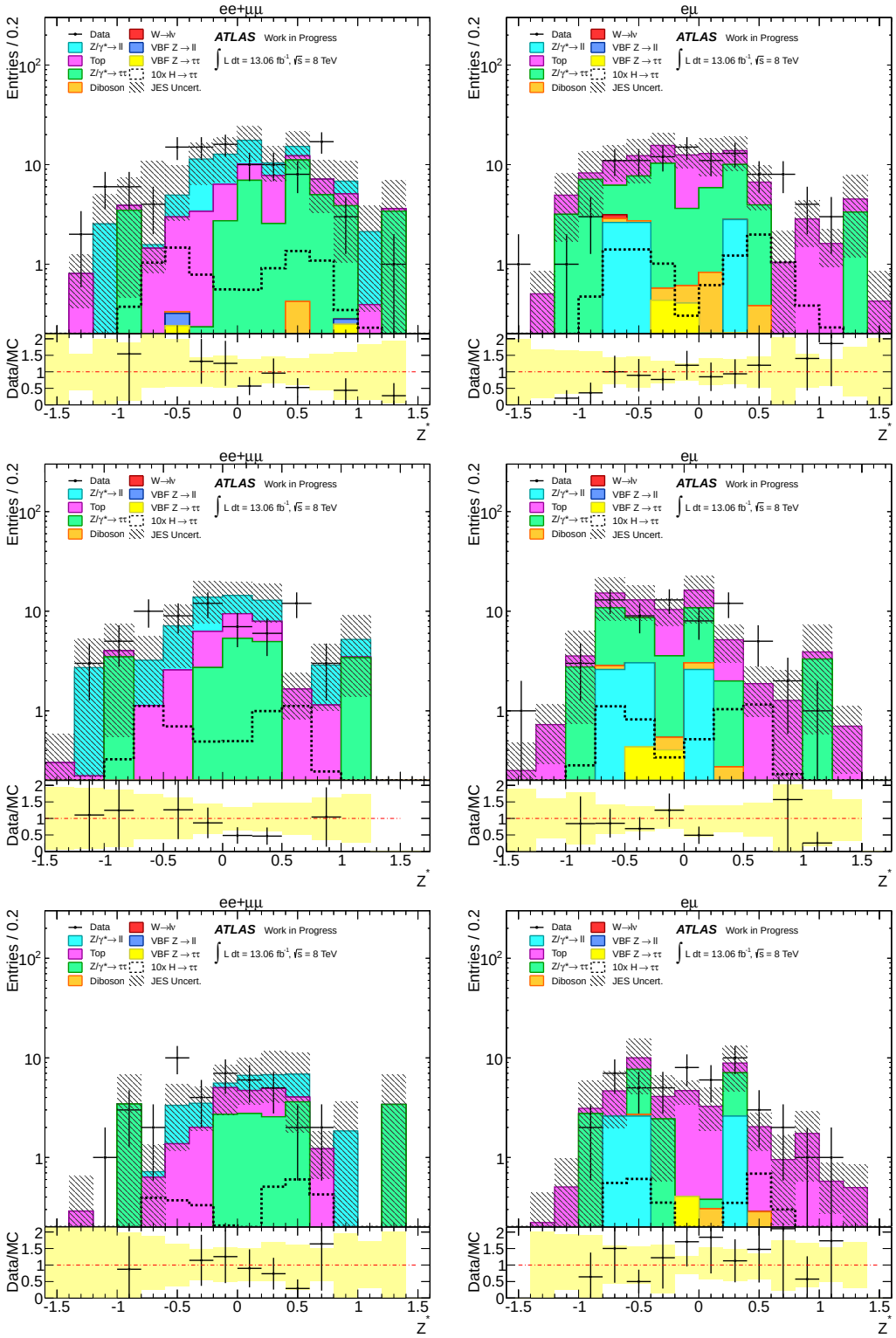

Figure BIII.15.: Z^* for additional jets with $p_t > 20$GeV (top),$p_t > 25$GeV (middle) and $p_t > 30$ GeV (bottom) after the b-tag veto.

List of Figures

List of Tables

Bibliography

[1] D. Griffiths, *Introduction to elementary particles*, Wiley-VCH, Weinheim. (2008)

[2] S. Chatrchyan, et al. (CMS Collaboration), *Observation of a new boson at a mass of 125 GeV with the CMS experiment at the LHC*, Phys. Lett. **B716**, 30 (2012), 1207.7235

[3] G. Aad, et al. (ATLAS Collaboration), *Observation of a new particle in the search for the Standard Model Higgs boson with the ATLAS detector at the LHC*, Phys. Lett. **B716**, 1 (2012), 1207.7214

[4] F. Halzen, A. D. Martin, *Quarks and Leptons: An introductory course in modern particle physics*, Wiley, New York. (1984)

[5] E. Noether, *Invariant Variation Problems*, Gott.Nachr. **1918**, 235 (1918), physics/0503066

[6] M. Robinson, *Symmetry and the Standard Model: Mathematics and Particle Physicss*, Springer. (2011)

[7] User:MissMJ, *Standard Model of Particle Physics* (27 June 2006, Published with CC3.0 License), URL http://en.wikipedia.org/wiki/File:Standard_Model_of_Elementa%ry_Particles.svg

[8] J. Beringer, et al. (Particle Data Group), *Review of Particle Physics (RPP)*, Phys. Rev. **D86**, 010001 (2012)

[9] S. Glashow, *Partial Symmetries of Weak Interactions*, Nucl.Phys. **22**, 579 (1961)

[10] S. Weinberg, *A Model of Leptons*, Phys. Rev.Lett. **19**, 1264 (1967)

[11] A. Salam, *Weak and Electromagnetic Interactions*, Conf.Proc. **C680519**, 367 (1968)

[12] J. Goldstone, A. Salam, S. Weinberg, *Broken Symmetries*, Phys. Rev. **127**, 965 (1962)

[13] M. Kobayashi, T. Maskawa, *CP Violation in the Renormalizable Theory of Weak Interaction*, Prog.Theor.Phys. **49**, 652 (1973)

[14] M. Banner, et al. (UA2 Collaboration), *Observation of Single Isolated Electrons of High Transverse Momentum in Events with Missing Transverse Energy at the CERN anti-p p Collider*, Phys. Lett. **B122**, 476 (1983)

[15] G. Arnison, et al. (UA1 Collaboration), *Experimental Observation of Isolated Large Transverse Energy Electrons with Associated Missing Energy at* $\sqrt{s} = 540$ *GeV*, Phys. Lett. **B122**, 103 (1983)

[16] P. Bagnaia, et al. (UA2 Collaboration), *Evidence for* $Z^0 \to e + e-$ *at the CERN anti-p p Collider*, Phys. Lett. **B129**, 130 (1983)

[17] N. Cabibbo, *Unitary Symmetry and Leptonic Decays*, Phys. Rev.Lett. **10**, 531 (1963)

[18] F. Gabbiani, E. Gabrielli, A. Masiero, L. Silvestrini, *A Complete analysis of FCNC and CP constraints in general SUSY extensions of the standard model*, Nucl.Phys. **B477**, 321 (1996), `hep-ph/9604387`

[19] P. W. Higgs, *Broken Symmetries and the Masses of Gauge Bosons*, Phys. Rev.Lett. **13**, 508 (1964)

[20] A. Djouadi, *The Anatomy of electro-weak symmetry breaking. I: The Higgs boson in the standard model*, Phys.Rept. **457**, 1 (2008), `hep-ph/0503172`

[21] L. Alvarez-Gaume, J. Ellis, *Eyes on a prize particle*, Nat. Phys. Journ. **7**, 1745 (2011/01)

[22] C. Bennett, D. Larson, J. Weiland, N. Jarosik, G. Hinshaw, et al., *Nine-Year Wilkinson Microwave Anisotropy Probe (WMAP) Observations: Final Maps and Results* (2012), `1212.5225`

[23] S. P. Martin, *A Supersymmetry primer* (1997), `hep-ph/9709356`

[24] W. Buchmuller, P. Di Bari, M. Plumacher, *Cosmic microwave background, matter - antimatter asymmetry and neutrino masses*, Nucl.Phys. **B643**, 367 (2002), `hep-ph/0205349`

[25] M. Spira, A. Djouadi, D. Graudenz, P. Zerwas, *Higgs boson production at the LHC*, Nucl.Phys. **B453**, 17 (1995), hep-ph/9504378

[26] G. Aad, et al. (ATLAS Collaboration), *ATLAS: Detector and physics performance technical design report. Volume 1* **(ATLAS-TDR-14)** (1999)

[27] G. Aad, et al. (ATLAS Collaboration), *ATLAS: Detector and physics performance technical design report. Volume 2* **(ATLAS-TDR-15)** (1999)

[28] J. Alcaraz (ALEPH and CDF and D0 and DELPHI and L3 and OPAL and SLD Collaboration), *Precision Electroweak Measurements and Constraints on the Standard Model* (2009), 0911.2604

[29] R. Barate, et al. (LEP Working Group for Higgs boson searches, ALEPH Collaboration, DELPHI Collaboration, L3 Collaboration, OPAL Collaboration), *Search for the standard model Higgs boson at LEP*, Phys. Lett. **B565**, 61 (2003), hep-ex/0306033

[30] TEVNPH (Tevatron New Phenomina and Higgs Working Group), CDF Collaboration, D0 Collaboration, *Combined CDF and D0 Search for Standard Model Higgs Boson Production with up to 10.0 fb^{-1} of Data* (2012), 1203.3774

[31] CDF and D0 Collaborations and the Tevatron New Physics and Higgs Working Group, *Updated Combination of CDF and D0 Searches for Standard Model Higgs Boson Production with up to 10.0 fb^{-1} of Data* (2012), 1207.0449

[32] G. Aad, et al. (ATLAS Collaboration), *An update of combined measurements of the new Higgs-like boson with high mass resolution channels* **(ATLAS-CONF-2012-170)** (2012)

[33] G. Aad, et al. (ATLAS Collaboration), *Coupling properties of the new Higgs-like boson observed with the ATLAS detector at the LHC* **(ATLAS-CONF-2012-127)** (2012)

[34] G. Aarons, et al. (ILC), *International Linear Collider Reference Design Report Volume 2: PHYSICS AT THE ILC* (2007), 0709.1893

[35] A. Chodos, R. Jaffe, K. Johnson, C. B. Thorn, V. Weisskopf, *A New Extended Model of Hadrons*, Phys. Rev. **D9**, 3471 (1974)

[36] C. Adloff, et al. (H1 Collaboration), *Deep inelastic inclusive e p scattering at low x and a determination of alpha(s)*, Eur.Phys.J. **C21**, 33 (2001), `hep-ex/0012053`

[37] S. Aid, et al. (H1 Collaboration), *A Measurement and QCD analysis of the proton structure function $f_2(x, q^2)$ at HERA*, Nucl.Phys. **B470**, 3 (1996), `hep-ex/9603004`

[38] Y. L. Dokshitzer, *Calculation of the Structure Functions for Deep Inelastic Scattering and e+ e- Annihilation by Perturbation Theory in Quantum Chromodynamics.*, Sov.Phys.JETP **46**, 641 (1977)

[39] A. Martin, W. Stirling, R. Thorne, G. Watt, *Parton distributions for the LHC*, Eur.Phys.J. **C63**, 189 (2009), `0901.0002`

[40] J. Pumplin, D. Stump, J. Huston, H. Lai, P. M. Nadolsky, et al., *New generation of parton distributions with uncertainties from global QCD analysis*, JHEP **0207**, 012 (2002), `hep-ph/0201195`

[41] H. Lai, et al. (CTEQ Collaboration), *Global QCD analysis of parton structure of the nucleon: CTEQ5 parton distributions*, Eur.Phys.J. **C12**, 375 (2000), `hep-ph/9903282`

[42] M. Gluck, E. Reya, A. Vogt, *Dynamical parton distributions of the proton and small x physics*, Z.Phys. **C67**, 433 (1995)

[43] H. Lai, J. Botts, J. Huston, J. Morfin, J. Owens, et al., *Global QCD analysis and the CTEQ parton distributions*, Phys. Rev. **D51**, 4763 (1995), `hep-ph/9410404`

[44] B. Andersson, G. Gustafson, G. Ingelman, T. Sjostrand, *Parton Fragmentation and String Dynamics*, Phys.Rept. **97**, 31 (1983)

[45] T. Sjostrand, *High-energy physics event generation with PYTHIA 5.7 and JETSET 7.4*, Comput.Phys.Commun. **82**, 74 (1994)

[46] T. Sjostrand, S. Mrenna, P. Z. Skands, *PYTHIA 6.4 Physics and Manual*, JHEP **0605**, 026 (2006), `hep-ph/0603175`

[47] G. Aad, et al. (ATLAS Collaboration), *The ATLAS Simulation Infrastructure*, Eur.Phys.J. **C70**, 823 (2010), `1005.4568`

[48] ATLAS LuminosityPublicResults, *ATLAS and LHC Luminosity 2012* (05.01.2013), URL `https://twiki.cern.ch/twiki/bin/view/AtlasPublic/LuminosityPublicResults`

[49] P. Z. Skands, *Tuning Monte Carlo Generators: The Perugia Tunes*, Phys.Rev. **D82**, 074018 (2010), `1005.3457`

[50] CERN, *LHC accelerator complex* (05.01.2013), URL `http://project-integration-accelerateurs.web.cern.ch/project-Integration-Accelerateurs/Integration/Images/`

[51] O. Bruning, H. Burkhardt, S. Myers, *The large hadron collider*, Prog.Part.Nucl.Phys. **67**, 705 (2012)

[52] O. S. Bruning, P. Collier, P. Lebrun, S. Myers, R. Ostojic, et al., *LHC Design Report. 1. The LHC Main Ring* (2004), `CERN-2004-003-V-1`

[53] G. Aad, et al. (ATLAS Collaboration), *The ATLAS Experiment at the CERN Large Hadron Collider*, JINST **3**, S08003 (2008)

[54] G. Bayatian, et al. (CMS Collaboration), *CMS physics: Technical design report* **(CERN-LHCC-2006-001)** (2006)

[55] C. Lourenco (ALICE Collaboration), *Heavy ion collisions at the LHC: The Alice experiment* pages 491–496 (1996), `hep-ph/9612221`

[56] LHCb Collaboration (LHCb Collaboration), *LHCb technical design report: Reoptimized detector design and performance* **(CERN-LHCC-2003-030)** (2003)

[57] M. Garcia-Sciveres (ATLAS Collaboration), *ATLAS Experiment Pixel Detector Upgrades* (2011), `1109.4662`

[58] G. Aad, et al. (ATLAS Collaboration), *ATLAS inner detector: Technical design report. Vol. 1* **(ATLAS-TDR-4)** (1997)

[59] G. Aad, et al. (ATLAS Collaboration), *ATLAS tile calorimeter: Technical design report* **(CERN-LHCC-96-42)** (1996)

[60] D. Berge, A. Hocker, T. Kono, H. Stelzer, T. Wengler, et al., *The configuration system of the ATLAS Trigger*, IEEE Trans.Nucl.Sci. **55**, 392 (2008)

[61] E. Barberio, et al. (ATLAS collaboration), *Re-optimized search for the Standard Model Higgs boson in the decay mode $H \to \tau_{lep}\tau_{lep}$ in pp collisions at $\sqrt{s} = 7$ TeV with ATLAS*, Technical report, CERN, Geneva (2012)

[62] G. Aad, et al. (ATLAS Collaboration), *Expected Performance of the ATLAS Experiment - Detector, Trigger and Physics* (2009), 0901.0512

[63] G. Aad, et al. (ATLAS Collaboration), *Reconstruction of collinear final-state-radiation photons in Z decays to muons in sqrts=7 TeV proton-proton collisions.*, Technical report, CERN, Geneva (2012)

[64] G. Aad, et al. (Atlas Collaboration), *Measurement of the $W \to \ell\nu$ and $Z/\gamma^* \to \ell\ell$ production cross sections in proton-proton collisions at $\sqrt{s} = 7$ TeV with the ATLAS detector*, JHEP **1012**, 060 (2010), 1010.2130

[65] G. Aad, et al. (ATLAS Collaboration), *Jet energy measurement with the ATLAS detector in proton-proton collisions at $\sqrt{s} = 7$ TeV* (2011), 1112.6426

[66] M. Cacciari, G. P. Salam, G. Soyez, *The Anti-k(t) jet clustering algorithm*, JHEP **0804**, 063 (2008), 0802.1189

[67] M. Cacciari, G. P. Salam, G. Soyez, *FastJet User Manual*, Eur.Phys.J. **C72**, 1896 (2012), 1111.6097

[68] W. Lampl, S. Laplace, D. Lelas, P. Loch, H. Ma, et al., *Calorimeter clustering algorithms: Description and performance* (2008)

[69] G. Aad, et al. (ATLAS Collaboration), *Jet energy scale and its systematic uncertainty in proton-proton collisions at sqrt(s)=7 TeV in ATLAS 2010 data* (2011)

[70] C. Albajar, et al. (UA1 Collaboration), *Search for B0 anti-B0 Oscillations at the CERN Proton - anti-Proton Collider. 2.*, Phys.Lett. **B186**, 247 (1987)

[71] G. Aad, et al. (ATLAS Collaboration), *Measurement of the b-tag Efficiency in a Sample of Jets Containing Muons with 5 fb^{-1} of Data from the ATLAS Detector* (2012)

[72] G. Aad, et al. (ATLAS Collaboration), *Commissioning of the ATLAS high-performance b-tagging algorithms in the 7 TeV collision data* (2011)

[73] D. Alvarez, et al. (ATLAS Collaboration), *Search for the Standard Model Higgs boson in the decay mode $H \to \tau_{lep}\tau_{lep}$ in pp collisions at $\sqrt(s) = 8$ TeV with ATLAS* **(ATL-COM-PHYS-2012-1166)** (2012)

[74] S. Agostinelli, et al. (GEANT4), *GEANT4: A Simulation toolkit*, Nucl.Instrum.Meth. **A506**, 250 (2003)

[75] E. Richter-Was, D. Froidevaux, L. Poggioli, *ATLFAST 2.0 a fast simulation package for ATLAS* (1998)

[76] M. L. Mangano, M. Moretti, F. Piccinini, R. Pittau, A. D. Polosa, *ALPGEN, a generator for hard multiparton processes in hadronic collisions*, JHEP **0307**, 001 (2003), `hep-ph/0206293`

[77] F. Caravaglios, M. L. Mangano, M. Moretti, R. Pittau, *A New approach to multijet calculations in hadron collisions*, Nucl.Phys. **B539**, 215 (1999), `hep-ph/9807570`

[78] S. Hoeche, F. Krauss, N. Lavesson, L. Lonnblad, M. Mangano, et al., *Matching parton showers and matrix elements* (2006), `hep-ph/0602031`

[79] G. Aad, et al. (ATLAS Collaboration), *Measurement of the production cross section for Z/gamma* in association with jets in pp collisions at $\sqrt{s} = 7$ TeV with the ATLAS detector*, Phys.Rev. **D85**, 032009 (2012), `1111.2690`

[80] G. Corcella, I. Knowles, G. Marchesini, S. Moretti, K. Odagiri, et al., *HERWIG 6: An Event generator for hadron emission reactions with interfering gluons (including supersymmetric processes)*, JHEP **0101**, 010 (2001), `hep-ph/0011363`

[81] J. Butterworth, J. R. Forshaw, M. Seymour, *Multiparton interactions in photoproduction at HERA*, Z.Phys. **C72**, 637 (1996), `hep-ph/9601371`

[82] G. Aad, et al. (ATLAS Collaboration), *First tuning of HERWIG/JIMMY to ATLAS data* **(ATL-PHYS-PUB-2010-014)** (2010)

[83] T. Gleisberg, S. Hoeche, F. Krauss, M. Schonherr, S. Schumann, et al., *Event generation with SHERPA 1.1*, JHEP **0902**, 007 (2009), `0811.4622`

[84] S. Frixione, B. R. Webber, *Matching NLO QCD computations and parton shower simulations*, JHEP **0206**, 029 (2002), `hep-ph/0204244`

[85] S. Frixione, P. Nason, C. Oleari, *Matching NLO QCD computations with Parton Shower simulations: the POWHEG method*, JHEP **0711**, 070 (2007), 0709.2092

[86] S. Jadach, J. H. Kuhn, Z. Was, *TAUOLA: A Library of Monte Carlo programs to simulate decays of polarized tau leptons*, Comput.Phys.Commun. **64**, 275 (1990)

[87] S. Jadach, Z. Was, R. Decker, J. H. Kuhn, *The tau decay library TAUOLA: Version 2.4*, Comput.Phys.Commun. **76**, 361 (1993)

[88] E. Barberio, Z. Was, *PHOTOS: A Universal Monte Carlo for QED radiative corrections. Version 2.0*, Comput.Phys.Commun. **79**, 291 (1994)

[89] A. Buckley, H. Hoeth, H. Lacker, H. Schulz, J. E. von Seggern, *Systematic event generator tuning for the LHC*, Eur.Phys.J. **C65**, 331 (2010), 0907.2973

[90] M. Guzzi, P. Nadolsky, E. Berger, H.-L. Lai, F. Olness, et al., *CT10 parton distributions and other developments in the global QCD analysis* (2011), 1101.0561

[91] S. Dittmaier, et al. (LHC Higgs Cross Section Working Group), *Handbook of LHC Higgs Cross Sections: 1. Inclusive Observables* (2011), 1101.0593

[92] P. Bolzoni, F. Maltoni, S.-O. Moch, M. Zaro, *Vector boson fusion at NNLO in QCD: SM Higgs and beyond*, Phys.Rev. **D85**, 035002 (2012), 1109.3717

[93] A. Djouadi, J. Kalinowski, M. Spira, *HDECAY: A Program for Higgs boson decays in the standard model and its supersymmetric extension*, Comput.Phys.Commun. **108**, 56 (1998), hep-ph/9704448

[94] R. V. Harlander, W. B. Kilgore, *Next-to-next-to-leading order Higgs production at hadron colliders*, Phys.Rev.Lett. **88**, 201801 (2002), hep-ph/0201206

[95] M. Spira, *HIGLU: A program for the calculation of the total Higgs production cross-section at hadron colliders via gluon fusion including QCD corrections* (1995), hep-ph/9510347

[96] S. Dittmaier, S. Dittmaier, C. Mariotti, G. Passarino, R. Tanaka, et al., *Handbook of LHC Higgs Cross Sections: 2. Differential Distributions* (2012), 1201.3084

[97] R. Gavin, Y. Li, F. Petriello, S. Quackenbush, *FEWZ 2.0: A code for hadronic Z production at next-to-next-to-leading order*, Comput.Phys.Commun. **182**, 2388 (2011), 1011.3540

[98] G. Aad, et al. (ATLAS Collaboration), *ATLAS tunes of PYTHIA 6 and Pythia 8 for MC11* **(ATL-PHYS-PUB-2011-009)** (2011)

[99] ATLAS, *Heavy Flavor Overlap Removal* (1995), hep-ph/9510347, URL https://twiki.cern.ch/twiki/bin/viewauth/AtlasProtected.HforTool

[100] P. Nason, *A New method for combining NLO QCD with shower Monte Carlo algorithms*, JHEP **0411**, 040 (2004), hep-ph/0409146

[101] M. Beneke, P. Falgari, S. Klein, J. Piclum, C. Schwinn, et al., *The total top-pair production cross section at NNLL* (2012), 1208.5578

[102] B. P. Kersevan, E. Richter-Was, *The Monte Carlo event generator AcerMC version 2.0 with interfaces to PYTHIA 6.2 and HERWIG 6.5* (2004), hep-ph/0405247

[103] N. Kidonakis, *Single top and top pair production* (2012), 1212.2844

[104] B. Mellado, W. Quayle, S. L. Wu, *Prospects for the observation of a Higgs boson with $H \to \tau^+\tau^- \to \ell^+\ell^- + \not{E}_T$ associated with one jet at the LHC*, Phys.Lett. **B611**, 60 (2005), hep-ph/0406095

[105] M. Ciccolini, A. Denner, S. Dittmaier, *Electroweak and QCD corrections to Higgs production via vector-boson fusion at the LHC*, Phys.Rev. **D77**, 013002 (2008), 0710.4749

[106] G. Gustafson, U. Pettersson, P. Zerwas, *Jet Final States in W W Pair Production and Color Screening in the QCD Vacuum*, Phys.Lett. **B209**, 90 (1988)

[107] T. Sjostrand, V. A. Khoze, *On Color rearrangement in hadronic W+ W- events*, Z.Phys. **C62**, 281 (1994), hep-ph/9310242

[108] R. Brun, F. Rademakers, *ROOT: An object oriented data analysis framework*, Nucl.Instrum.Meth. **A389**, 81 (1997)

[109] I. Antcheva, M. Ballintijn, B. Bellenot, M. Biskup, R. Brun, et al., *ROOT: A C++ framework for petabyte data storage, statistical analysis and visualization*, Comput.Phys.Commun. **180**, 2499 (2009)

[110] G. Aad, et al. (ATLAS Collaboration), *Electron and photon reconstruction and identification in ATLAS: expected performance at high energy and results at 900 GeV* **(ATLAS-CONF-2010-005)** (2010)

[111] Atlas JetEtMiss WG, *How to clean jets in 2012 data* (01.10.2012), URL `https://twiki.cern.ch/twiki/bin/viewauth/AtlasProtected/HowToCleanJets2012`

[112] J. Alwall, S. Hoche, F. Krauss, N. Lavesson, L. Lonnblad, et al., *Comparative study of various algorithms for the merging of parton showers and matrix elements in hadronic collisions*, Eur.Phys.J. **C53**, 473 (2008), `0706.2569`

[113] G. Aad, et al. (ATLAS Collaboration), *Measurement of the top quark pair production cross-section based on a statistical combination of measurements of dilepton and single-lepton final states at $\sqrt{s} = 7$ TeV with the ATLAS detector* **(ATLAS-CONF-2011-108)** (2011)

[114] J. M. Campbell, R. Ellis, *MCFM for the Tevatron and the LHC*, Nucl.Phys.Proc.Suppl. **205-206**, 10 (2010), `1007.3492`

[115] G. Aad, et al. (ATLAS Collaboration), *Luminosity Determination in pp Collisions at sqrt(s) = 7 TeV using the ATLAS Detector in 2011* **(ATLAS-CONF-2011-116)** (2011)

[116] G. Aad, et al. (ATLAS Collaboration), *Improved luminosity determination in pp collisions at sqrt(s) = 7 TeV using the ATLAS detector at the LHC* (2013), `1302.4393`

[117] D. L. Rainwater, D. Zeppenfeld, K. Hagiwara, *Searching for $H \to \tau^+\tau^-$ in weak boson fusion at the CERN LHC*, Phys.Rev. **D59**, 014037 (1998), `hep-ph/9808468`

[118] R. K. Ellis, I. Hinchliffe, M. Soldate, J. van der Bij, *Higgs Decay to tau+ tau-: A Possible Signature of Intermediate Mass Higgs Bosons at the SSC*, Nucl.Phys. **B297**, 221 (1988)

[119] T. Plehn, D. L. Rainwater, D. Zeppenfeld, *A Method for identifying $H \to \tau^+\tau^- \to e^\pm\mu^\mp p_T$ at the CERN LHC*, Phys.Rev. **D61**, 093005 (2000), `hep-ph/9911385`

[120] M. Albrow, A. Rostovtsev, *Searching for the Higgs at hadron colliders using the missing mass method* (2000), `hep-ph/0009336`

[121] A. Elagin, P. Murat, A. Pranko, A. Safonov, *A New Mass Reconstruction Technique for Resonances Decaying to di-tau*, Nucl.Instrum.Meth. **A654**, 481 (2011), `1012.4686`

Danksagung

First of all, I would like to thank my first referee Prof. Dr. Arnulf Quadt for providing the opportunity to write this master thesis at the II. Institute of Physics in Göttingen. As you also know *wie der Hase so läuft*, your reliability and support during my studies in Göttingen were encouraging and ensured a smooth course for my thesis. Furthermore, I owe you special thanks for the great time I had in Amsterdam - the intense studies at NIKHEF and the even more intense times at the *Tweede Kamer*.

I also would like to thank my second referee *Priv. Doz. Dr. Dipl. Phys. Shizzle K Boomtastic* Kevin Kröninger for bringing some joy in an occasional rather dull daily office routine.

I am deeply grateful to Ulla Blumenschein for supervising me during the last year. Your friendly nature, relentless effort and tremendous knowledge were very motivating and made this thesis possible. Thank you as well for the opportunity to establish my position in the world of particle physics research.

Oleg, although you joined later, your motivational skills helped me getting through the last months. I hope we will intensify our collaborative (beer-)researches in the future. And thank you both, Ulla and Oleg, very much, for correcting my thesis in such great detail.

Many thanks as well to you, Katharina, for sharing your technical knowledge, helping me to debug my code and the joyful meetings.

I would also like to thank the ATLAS $H \to \tau^+_{\text{lep}}\tau^-_{\text{lep}}$ working group, in particular Xin Chen and Christian Schillo, for helping me to solve problems by seemingly never-ending cutflow comparisons and for providing useful information.

Mein tiefster Dank gilt meiner Familie. Ohne euren Rückhalt, eure mentale Bestärkung und nicht zuletzt finanzielle Unterstüzung wäre mir mein Studium nicht möglich gewesen. Danke für die endlosen Minigolfrunden, Petabytes and Katzenbilder und das Aufbauen in schwierigen Stunden.
Auch meinem Ihme-Rolovschen Ruheresort möchte ich für die vielen kleinen und großen Nettigkeiten danken. <3

Erklärung nach §18(8) der Prüfungsordnung für den Bachelor-Studiengang Physik und den Master-Studiengang Physik an der Universität Göttingen:

Hiermit erkläre ich, dass ich diese Abschlussarbeit selbständig verfasst habe, keine anderen als die angegebenen Quellen und Hilfsmittel benutzt habe und alle Stellen, die wörtlich oder sinngemäß aus veröffentlichten Schriften entnommen wurden, als solche kenntlich gemacht habe.
Darüberhinaus erkläre ich, dass diese Abschlussarbeit nicht, auch nicht auszugsweise, im Rahmen einer nichtbestandenen Prüfung an dieser oder einer anderen Hochschule eingereicht wurde.

Göttingen, den May 9, 2014

(Eric Drechsler)